Analyzing the Role of CyFIP2 in the Mouse Brain

Dissertation

zur

Erlangung des Doktorgrades (Dr. rer. nat.)

der

Mathematisch-Naturwissenschaftlichen Fakultät

der

Rheinischen Friedrich-Wilhelms Universität Bonn

Vorgelegt von

Ilkin Deniz Özer

aus

Trabzon, Türkei

Bonn, 2020

Angefertigt mit Genehmigung der Mathematischen-Naturwissenschaftlichen-Fakultät
der Rheinischen Friedrich-Wilhelms-Universität Bonn.

1. Gutachter: Prof. Dr. rer. nat. Walter Witke
2. Gutachter: Prof. Dr. rer. nat. Frank Bradke

Tag der Promotion: 05.06.2020
Erscheinungsjahr: 2020

To my parents,
for making everything possible.

Summary

An important regulator of neuron outgrowth, growth cone motility and dendritic spine formation is the actin nucleator ARP2/3, a protein complex that functions in forming branched actin networks. ARP2/3 complex activity is regulated by the class I nucleation promoting factor WAVE regulatory complex (WRC). In the brain, a crucial component of the pentameric WRC is the Cytoplasmic Fragile-X Mental Retardation Protein (FMRP) Interacting Protein 2 (CyFIP2) that is highly expressed in neurons. Knockout of the *Cyfip2* gene in mice leads to perinatal lethality. When *Cyfip2* is conditionally knocked out exclusively in the central nervous system (CNS), the mice fully recapitulate the complete knockout phenotype, thus suggesting a specific role for CyFIP2 in the CNS. Here we present our studies on a viable *Cyfip2* conditional knockout mouse model, in which the deletion of the gene occurs at around postnatal day 18 (P18) mainly in hippocampal and cortical glutamatergic neurons.

Upon complete loss of CyFIP2, we observed an increase of the small, dynamic actin filaments with no detectable changes in the stable actin pool. The analysis of excitatory synaptic transmission using patch-clamp recordings as well as Schaffer collateral stimulation recordings showed decreased excitatory synaptic transmission and defects in pre-synaptic vesicle exocytosis in the hippocampus. Using electron microscopy, we also showed reduced pre-synaptic bouton area accompanied by decreased neurotransmitter vesicle density in both Schaffer collaterals and mossy fibers, while post-synaptic densities did not appear significantly altered.

In aged mice lacking CyFIP2, we observed increased dendritic spine number possibly in an attempt to compensate for the defects observed in the pre-synapse. These spines were mostly immature, phenocopying the Fragile-X syndrome mouse model. Lastly, a combination of behavioral tests showed a mild anxiety-like phenotype in *Cyfip2* forebrain knockout mice with no defects in working and short-term memory according to Y-maze and novel object recognition experiments, respectively.

Our electrophysiological, morphological and biochemical results together suggest a role of CyFIP2 in the structural maintenance of pre-synaptic terminals and dendritic spine maturation in the adult mouse brain that does not appear to be relevant for neurodegenerative processes, but rather for intellectual disability.

Table of Contents

List of Figures

List of Tables

Abbreviations

°	Arc degrees
°C	Degree Celsius
+/+, wt	Wild type
Aβ	Amyloid beta
ABI	Abelson-interacting protein
ABP	Actin binding protein
ACSF	Artificial cerebrospinal fluid
AD	Alzheimer's disease
ADF	Actin-depolymerizing factor
ADP	Adenosine diphosphate
AMPA	alpha-amino-3-hydroxy-5-methyl-4-isoxazolepropionic acid
AP	Action potential
APP	Amyloid precursor protein
ARP2/3	Actin-related protein 2/3
ARPC	Actin-related protein complex protein
ASD	Autism spectrum disorder
ATP	Adenosine triphosphate
BACE1	Beta-secretase 1
bp	Base pair(s)
BSA	Bovine serum albumin
CAMK2A	Calcium/calmodulin-dependent protein kinase II alpha
C_c	Critical concentration
CNS	Central nervous system
CyFIP	Cytoplasmic FMRP-interacting protein
de novo	Anew
DNA	Deoxyribonucleic acid
dNTP	Deoxyribonucleoside triphosphate
e.g.	Exempli gratia (for example)
ECL	Enhanced chemical luminescence
EDTA	Ethylenediaminetetraacetic acid
EGTA	Ethyleneglycoltetraacetic acid

eIF4E	Eukaryotic initiation factor 4E
EPSP	Excitatory post-synaptic potential
et al.	Et alii (and others)
F-actin	Filamentous actin
FH	Formin homology
flx	Floxed allele (exon[s] flanked by loxP sites)
FMR1	Fragile X mental retardation 1
FMRP	Fragile X mental retardation protein
FXS	Fragile X syndrome
G-actin	Globular actin
GABA	gamma-aminobutyric acid
GΩ	Gigaohm
HEPES	4-(2-hydroxyethyl)-1-piperazineethanesulfonic acid
HRP	Horseradish peroxidase
HSPC300	Hematopoietic stem/progenitor cell protein 300
IEI	Inter-event interval
IRES	Internal ribosome entry site
kDa	Kilodalton
LTD	Long-term depression
LTP	Long-term potentiation
mA	Milliampere
mEPSC	Miniature excitatory post-synaptic current
mg	Milligram
mGluR	Metabotropic glutamate receptor
min	Minute
ml	Milliliter
mM	Millimolar
mPSC	Miniature post-synaptic current
mRNA	Messenger RNA
ms	Millisecond
mV	Millivolt
MΩ	Megaohm
NAP1	Nck-associated protein 1

NFT	Neurofibrillary tangle
nm	Nanometer
NMDA	N-methyl-D-aspartate
NMJ	Neuromuscular junction
NPF	Nucleation-promoting factor
nt	Nucleotide(s)
o/n	Overnight
P	Postnatal
pA	Picoampere
PAGE	Polyacrylamide gel electrophoresis
PCR	Polymerase chain reaction
PET	Positron-emission tomography
P_i	Inorganic phosphate
PPR	Paired-pulse ratio
PSD	Post-synaptic density
PTX	Picrotoxin
PVDF	Polyvinylidene difluoride
QX-314	N-(2,6-Dimethylphenylcarbamoylmethyl)triethylammonium bromide
RAC1	Ras-related C3 botulinum toxin substrate 1
RNA	Ribonucleic acid
RP	Reserve pool
RPM	Revolutions per minute
RRP	Readily releasable pool
RT	Room temperature
SDS	Sodium dodecyl sulfate
SNAP25	Synaptosome associated protein 25
SNARE	SNAP receptor
TCM	Trichlormethiazide
TTX	Tetrodotoxin
V	Volt
VCA	Verprolin-homology, central, acidic (domain)
w/v	Weight/volume

WASH	Wiskott-Aldrich syndrome protein and SCAR homologue
WASP	Wiskott-Aldrich syndrome protein
WAVE	WASP family verprolin-homologous protein
WH	WASP homology
WHAMM	WASP homolog associated with actin
WRC	WAVE regulatory complex
X-gal	5-bromo-4-chloro-3-indolyl-beta-D-galactopyranoside
µA	Microampere
µg	Microgram
µl	Microliter
µM	Micromolar

1. Introduction

1.1 The actin cytoskeleton

The cytoskeleton is a network of filaments that function as a structural support in eukaryotic cells and plays crucial roles in dynamic processes such as cell division, intracellular transport and migration. It is composed of three different structures: microtubules – with 23 nm in diameter; intermediate filaments – with a diameter of 10 nm; and the smallest ones, with 7 nm diameter, the actin filaments (Holmes *et al.*, 1990). This thesis work focuses on the actin filaments, which play essential roles during cell growth, differentiation, motility and division, as well as for membrane trafficking and intracellular transport (Dominguez and Holmes, 2011). The 42 kDa actin monomer is a highly conserved protein and the most abundant one in eukaryotic cells (Kron *et al.*, 1992).

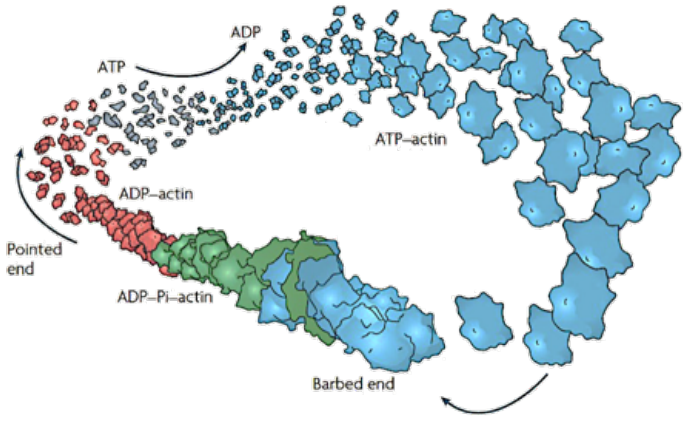

Figure 1. The actin treadmilling cycle.
ATP-bound G-actin monomers (blue) bind to the barbed (+) end of an actin filament with strong affinity. As the new monomers bind, the old ones are hydrolyzed slowly releasing Pi and forming ADP -actin (green), eventually dissociating from the pointed (-) end (red). The free G-actin monomers are then re-loaded with ATP, entering the cycle again by binding to the barbed (+) end of the filament. The different polymerization rates at the barbed (+) and pointed (-) ends result in the initial elongation of the actin filaments, and then lead to a treadmilling process in the steady state (figure adapted from Pak, Flynn, and Bamburg 2008).

Actin monomers, called globular actin (G-actin), polymerize into long double helical filaments of actin (F-actin), generating a robust structure that is still highly dynamic. Filaments are polymerized *de novo* from an actin nucleus, which consist of three G-actin or G-actin-like monomers. ATP-bound G-actin monomers are added at the barbed (+) end of a nucleus or a polymer (Figure 1). As the filament elongates, the ATP that is bound to the incorporated G-actin is hydrolyzed into ADP and inorganic

phosphate (P_i). This eventually leads to the dissociation of G-actin monomers from the pointed (-) end (Pak, Flynn and Bamburg, 2008). Actin filaments are structurally polar and the critical concentration (C_c) of actin monomers for their binding to the filament is different at the two ends. The C_c is lower (0.1 µM) at the barbed end of the filament, with a higher on and lower off rate (monomers bind faster than they dissociate). At the pointed end C_c is higher (1 µM), leading monomers to dissociate faster than they bind (Pantaloni, Carlier and Coue, 1984). When the actin concentration in the cell is in between these two C_c, a net actin addition will occur at the barbed end whereas a net dissociation will take place at the pointed end. This movement of the actin filament in the direction of the barbed end is called actin treadmilling (Lodish *et al.*, 2000; Dominguez and Holmes, 2011). The treadmilling of actin filaments is crucial for cell processes such as motility, filopodia and lamellipodia formation (Chhabra and Higgs, 2007).

1.1.1. Actin binding proteins

Regulation of cellular processes such as motility, intracellular transport and cell division requires precise and rapid control of the actin cytoskeleton dynamics in the cell. This is ensured by actin binding proteins (ABPs) (Figure 2), which can increase actin turnover by over 100-fold (Didry, Carlier and Pantaloni, 1998).

The spontaneous nucleation of actin monomers is an energetically unfavorable process that requires the formation of an actin nucleus by a G-actin trimer. To speed up this process, actin nucleators (*e.g.* ARP2/3 complex, formins, spire, cordon-bleu) bind to G-actin or G-actin-like monomers and bring them together. They enable the polymerization of the filament by mimicking or stabilizing the nucleation complex (Winder, 2005). Profilin binds to free ADP-G-actin monomers in the cytoplasm exchanging the ADP with ATP to provide polymerization competent G-actin monomers to the nucleation or elongation factors on the (+) end of the growing filament (Witke, 2004). Conversely, recycling of G-actin monomers is achieved by actin depolymerization factors such as ADF and cofilin (Bamburg, 1999; Bernstein and Bamburg, 2010). Regulation of filament length is achieved by the filament-severing and capping protein gelsolin, which functions by cutting the filament into two pieces

and blocking their ends (Pollard, 2016). Another factor involved in this process are the end-capping proteins CapZ/CapG that bind to the barbed end of the filament and prevent addition of monomers (dos Remedios *et al.*, 2003). The cross-linking of long filaments into ordered structures as bundles and networks that make up filopodia and lamellipodia is achieved by ABPs such as spectrin, fimbrin and fascin, as well as the actin nucleator ARP2/3 complex (Winder, 2005; Weston, Coutts and La Thangue, 2012).

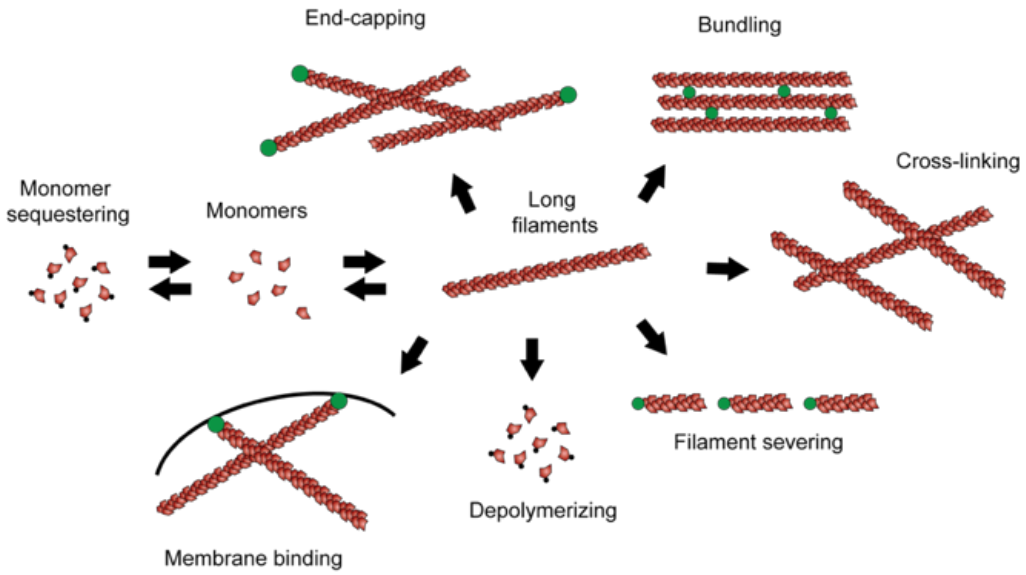

Figure 2. Functions of actin binding proteins.
Actin binding proteins have various functions in the cell ranging from monomer binding (*e.g.* profilin), end-capping (*e.g.* CapG, CapZ), filament bundling and cross-linking (*e.g.* fascin, filamin, ARP2/3), and membrane binding (*e.g.* α-actinin) to filament severing (*e.g.* gelsolin) and depolymerizing (*e.g.* ADF/cofilin). These proteins ensure the overall spatial and temporal regulation of actin dynamics in different cellular functions.

1.1.2. Actin nucleation factors

The rate-limiting step of actin polymerization is the formation of a nucleation complex consisting of three G-actin monomers. This is overcome with the help of actin nucleation factors that mimic the trimeric nucleation core or stabilize an existing nucleation core. There are three classes of actin nucleation factors: formins, WH2-domain-containing nucleators (*e.g.* Spire) and the ARP2/3 complex (Figure 3).

Formins are a family of proteins that contain formin homology (FH) domains. The FH1 domains function in recruiting profilin bound G-actin monomers to form the nucleus

while FH2 dimers keep formins bound to the barbed end of an actin filament and allow the FH1 domains to function also for the elongation of the filament (Romero *et al.*, 2004). Conversely, spire binds to four G-actin monomers through its WH2 domains and forms a tetramer, which then homodimerizes with another tetramer to form the octamer nucleation core. It then remains associated to the pointed end of the actin filament (Weston, Coutts and La Thangue, 2012).

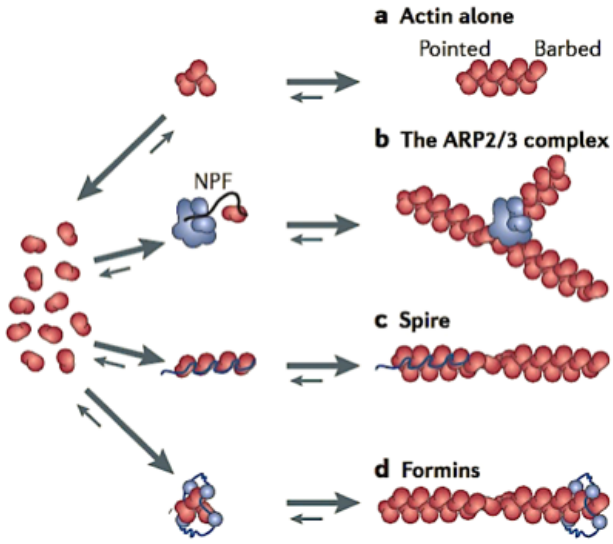

Figure 3. Actin nucleation mechanisms in the cell.
(a) Polymerization of actin begins with the formation of an energetically unfavorable actin nucleation core that consists of a minimum of three G-actin monomers. Actin nucleation factors help forming the actin nucleation core in mainly three different ways: (b) the ARP2/3 complex, activated by nucleation-promoting factors (NPFs), binds to the side of an existing actin filament and nucleates a new filament, leading to branching; (c) spire forms a tetramer of G-actin monomers which then binds to a second tetramer to form an actin octamer nucleus; (d) formins favor the formation of a G-actin trimer and also function as elongation factors by remaining bound to the barbed end of a filament (figure adapted from Goley and Welch, 2006).

The last class of actin nucleation factors is the ARP2/3 complex that was identified by its affinity to bind to profilin in *Acanthamoeba castellanii* (Machesky, 1994). The ARP2/3 complex consists of seven subunits: ARP2, ARP3, actin-related protein complex 1 (ARPC1), ARPC2, ARPC3, ARCP4 and ARPC5. Activation of the ARP2/3 complex by nucleation promoting factors (NPFs) allows it to bind to existing (mother) filaments and create an actin nucleus for a new (daughter) filament that branches with a 70° angle (Goley and Welch, 2006). By remaining bound to the pointed-end of the actin filament, ARP2/3 complex functions as an end-capping protein and allows filament elongation from the barbed end by other factors (San Miguel-Ruiz and Letourneau, 2014).

ARP2/3 complex activation requires the binding of NPFs, which are divided into two classes. Class I NPFs (*e.g.* WRC, WASP, WASH, WHAMM) bind to both the ARP2/3 complex and a G-actin monomer through their VCA domain (V; Verprolin-homology

[also called WH2] domain, C; central domain and A; acidic domain). This leads to the formation of the actin nucleus through close interaction of ARP2, ARP3 and the G-actin monomer (Mullins, Heuser and Pollard, 1998). Class II NPFs (*e.g.* cortactin) also bind to the ARP2/3 complex through their acidic domain, differing from class I NPFs for their binding to F-actin instead of a G-actin monomer (Rotty, Wu and Bear, 2013). Lastly, while class I NPFs dissociate after the nucleation of a new branch, class II NPFs remain bound to the ARP2/3 complex. This supports the hypothesis that class I NPFs are the major activators of branched actin nucleation, whereas class II NPFs act as stabilizers instead (Campellone and Welch, 2010).

1.1.3. The WAVE regulatory complex

A major activator of the ARP2/3 complex is the class I NPF WAVE (WASP family verprolin-homologous protein) regulatory complex (WRC) (Figure 4). The WRC is a ~400 kDa heteropentameric structure consisting of the proteins WAVE, ABI (Abelson-interacting protein), HSPC300 (Hematopoietic stem/progenitor cell protein 300), NAP1 (Nck-associated protein 1) and CyFIP (Cytoplasmic Fragile-X mental retardation-protein [FMRP] interacting protein) (Chen *et al.*, 2014). WAVE has three isoforms, of which the WAVE1 and WAVE3 are predominantly expressed in the brain, whereas WAVE2 is ubiquitously expressed (Takenawa and Miki, 2001; Takenawa and Suetsugu, 2007). ABI also has three isoforms, however, only the ubiquitously expressed ABI1 and the brain specific ABI2 have been shown to be involved in the WRC (Eden *et al.*, 2002; Innocenti *et al.*, 2004). CyFIP has two isoforms (Schenck *et al.*, 2003), the ubiquitously expressed CyFIP1 and CyFIP2, which is predominantly expressed in the brain.

The crystal structure of the WRC revealed that CyFIP and NAP, the two bigger proteins of the complex, serve as a scaffold for the other proteins to bind (Chen *et al.*, 2010). Different WRCs can be assembled by the combination of different isoforms of the WRC components. Recent studies in our lab have shown that three complexes coexist in the brain, one formed by the ubiquitously expressed CyFIP1 and WAVE2 isoforms, and the other two formed by WAVE1 and WAVE3 with CyFIP2 (Beuck, unpublished).

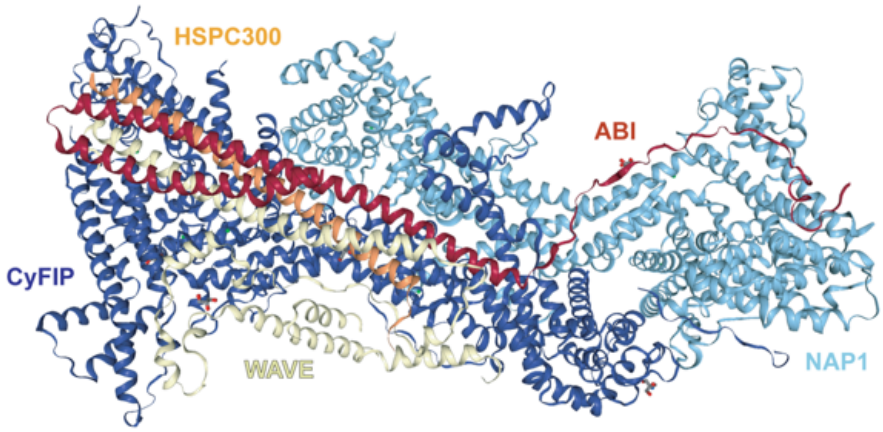

Figure 4. Crystal structure of the WAVE regulatory complex.
The heteropentameric WRC consists of the proteins WAVE (1-3), ABI (1-2), HSPC300, NAP1 and CyFIP (1-2), where the latter two serve as a scaffold base. The WRC binds to the ARP2/3 complex and to one G-actin monomer through the VCA domain, thus bringing the G-actin in close proximity with the ARP2 and ARP3 proteins to mimic a trimeric nucleus. The VCA is basally sequestered by CyFIP, allowing regulation of WRC activity by extracellular signaling (figure adapted from Chen et al. 2010).

The intrinsically inactive WRC can be activated by the small GTPase RAC1, which binds to CyFIP1 and leads to the exposure of the VCA domain of WAVE (that is basally sequestered by CyFIP) (Steffen *et al.*, 2004; Derivery *et al.*, 2009). The acidic domain of the VCA then binds to the ARP2/3 complex, bringing the ARP2 and ARP3 proteins in close proximity with a G-actin monomer. This trimer is a mimic of an actin nucleus that leads to the elongation of a daughter filament (Mullins, Heuser and Pollard, 1998).

1.1.4. The CyFIP1 isoform

The CyFIP protein family is highly conserved in evolution and both paralogues, CyFIP1 (its gene encoded on Chromosome 15 in human and Chromosome 7 in mouse) and CyFIP2 (its gene encoded on Chromosome 5 in human and Chromosome 11 in mouse), consist of 1253 amino acids with 88 % sequence identity and 95 % sequence similarity (Schenck *et al.*, 2001). CyFIP1 is a ~145 kDa protein which was discovered through its interaction with RAC1, initially giving it the name Specifically Rac-associated protein 1 (SRA1) (Kobayashi *et al.*, 1998). At the same time, due to its quantitative interaction with the ABP profilin it was named partner of profilin (POP) in our lab (Witke *et al.*, 1998). Shortly after this, an independent study reported increased CyFIP2 mRNA in cell lines expressing the apoptosis-inducing p53 mutant 121F,

therefore naming it PIR121 (p53-inducible RNA, 121F-specific) (Saller *et al.*, 1999). Lastly, using a yeast two-hybrid system, CyFIP1 and 2 were shown to interact with FMRP by Schenck et al. in 2001, giving CyFIP its current name. FMRP is an RNA binding protein that is involved in the regulation of mRNA translation, localization and stability (Verheij *et al.*, 1993). A silencing mutation of the *FMR1* gene, which codes for FMRP, leads to the most common form of mental retardation, Fragile-X syndrome (FXS) (Wohrle *et al.*, 1992; De Boulle *et al.*, 1993). More than 200 CCG trinucleotide repeats in the 5' untranslated region of the *FMR1* gene lead to the full silencing of the gene by an unstable hypermethylation (Hoeffer *et al.*, 2012). A link of CyFIP1 to autism spectrum disorder (ASD) and intellectual disability (ID) was demonstrated by studies that showed reduced CyFIP1 levels in lymphoblasts of FXS patients with ASD (Nowicki *et al.*, 2007). Additionally, genome-wide expression profiling of ASD patients with a duplication in 15q11-q13 region of the genome showed a significant upregulation of *Cyfip1* mRNA (Nishimura *et al.*, 2007). Recently, using RT-PCR, the levels of both CyFIP1 and CyFIP2 were shown to be elevated in the blood of ASD patients (Noroozi *et al.*, 2018).

In a 2014 study by Pathania et al., using a CyFIP1/2-GFP construct transfected in cultured neurons, both isoforms appeared to localize in dendritic spines. The same study showed that the overexpression of both isoforms enhanced dendritic complexity, whereas *Cyfip1*$^{+/-}$ cultured hippocampal neurons showed decreased dendritic complexity and spine maturation (Pathania *et al.*, 2014). Recently, the same research group showed that both CyFIP isoforms are present in inhibitory synapses, observed by co-localization of CyFIP1/2-GFP signal and the inhibitory post-synaptic marker gephyrin in cultured hippocampal neurons (Davenport *et al.*, 2019). The knockdown of *Cyfip1* in cultured cells by RNAi was shown to lead to defects in lamellipodia formation and a significant reduction of WAVE2 (Steffen *et al.*, 2004). The consequences of *Cyfip1* complete knockout in the mouse were dramatic, resulting in embryonic lethality around embryonic day 6.5 (E6.5) due to defects in gastrulation (Pathania *et al.*, 2014; Stöcker, 2015). Complementary to its role in the WRC and thus actin dynamics, CyFIP1 was found to independently interact with the translation machinery. A 2008 study by Napoli et al. showed that CyFIP1 binds to the eukaryotic initiation factor 4E (eIF4E) and in cooperation with FMRP it is involved in the

repression of mRNA translation in neurons. Further studies demonstrated that CyFIP1 shifts between eIF4E and the WRC through a conformational change facilitated by the activation of RAC1 GTPase by the brain-derived neurotrophic factor (BDNF) (De Rubeis *et al.*, 2013).

1.1.5. The CyFIP2 isoform

CyFIP2, albeit its sequence similarity to CyFIP1, displays non-redundant functions during development and in the adult organism (Cioni *et al.*, 2018). In contrast to its ubiquitously expressed paralogue, CyFIP2 is expressed only in the brain, kidney, spleen and thymus (Beuck, unpublished). The expression of CyFIP2 starts at ~E11.5, reaching its peak between P14-P21 and stabilizing in the adult mouse (Hauck, unpublished; Bonaccorso *et al.*, 2015). The full knockout of *Cyfip2* leads to perinatal lethality with no defects in brain size and morphology (Kumar *et al.*, 2013; Han *et al.*, 2015; Zhang *et al.*, 2019). In a recent study, an RNA sequencing performed on cortical tissues of *Cyfip2*$^{-/-}$ at E18.5 showed upregulated ECM receptor interactors and focal adhesion markers (Zhang *et al.*, 2019).

A role of CyFIP2 has been shown in growth cone regulation and axonal outgrowth. In Drosophila NMJs, a role of *dCyFIP* was demonstrated in synaptic bouton maintenance (Schenck *et al.*, 2003). The zebrafish orthologue of CyFIP2, nev, was shown to be involved in axonal outgrowth and guidance (Pittman, Gaynes and Chien, 2010). Moreover, a recent study presented a role of CyFIP2 in axonal sorting in the optic tract of zebrafish, showing the relocation of CyFIP2 into the peripheral domain of growth cones to regulate filopodial dynamics via the WRC (Cioni *et al.*, 2018).

Similar to its paralogue, CyFIP2 was shown to be linked to certain neuropsychiatric disorders. The C57BL/6N substrain of mice carries a missense mutation at S968F in the CyFIP2 protein, which was shown to reduce the locomotor response to cocaine (Kumar *et al.*, 2013). The same mutation was later shown to lead to a greater susceptibly to binge-eating in the C57BL/6N mice compared to the C57BL/6J substrain (Kirkpatrick *et al.*, 2017). On the other hand, *Cyfip2*$^{+/-}$ mice showed normal synaptic transmission in the hippocampus, conserved input-output responses, as well

as conserved long-term potentiation and depression. Also, total spine density and mature/immature spine ratios were conserved in the hippocampus of *Cyfip2*$^{+/-}$ mice (Han *et al.*, 2015). In contrast, DHPG induced expression of CyFIP2 and dendritic spine remodeling was impaired in cultured *Cyfip2*$^{+/-}$ cortical neurons, suggesting a role of CyFIP2 in dendritic spine remodeling upon its translational upregulation by mGluR activation (Han *et al.*, 2015). In line with this study, Lee at al. determined two phosphorylation sites of CyFIP2 (S582 and T1067), specifically in the brain. The phospho-blocking mutant T1067A showed significantly decreased density of stubby spines, while the overexpression of the wild-type (wt) protein increased neurite length in cultured hippocampal neurons, supporting the role of CyFIP2 in dendritic spine remodeling (Lee *et al.*, 2017).

1.1.5.1. CyFIP2 is expressed predominantly in brain

In previous studies the mRNA levels of *Cyfip2* were shown to be ~10-fold higher in the brain than *Cyfip1* (Massimi, 2008). This finding was later supported by the predominant expression levels of CyFIP2 in the brain compared to CyFIP1 (Hauck, unpublished).

A transgenic *Cyfip2-lacZ* reporter mouse line expressing β-galactosidase under the endogenous *Cyfip2* promoter was used to determine the *Cyfip2* expression pattern in the mouse. In agreement with the expression pattern observed by western blotting, CyFIP2 expression was detected in spleen, thymus, kidney, and prominently in the central nervous system (CNS). In the brain, CyFIP2 is expressed strongly in all cortical layers, hippocampus and, to a lesser degree, in the thalamus and striatum (Hauck, unpublished).

1.1.5.2. Alzheimer's-like phenotype of *Cyfip2*$^{+/-}$ mice

In 2016, a study by Tiwari *et al.* claimed a role for CyFIP2 in Alzheimer's disease. In the study the researchers showed that hippocampal lysates prepared from post-mortem brains of severe Alzheimer's patients have 50 % reduction of CyFIP2. The 50 % CyFIP2 decrease was also observed in the Alzheimer's mouse model Tg2576,

which overexpresses a mutant form of amyloid precursor protein (APP, isoform 695) with the Swedish double mutation (KM670/671NL). Based on these findings, the researchers studied the levels of certain Alzheimer's disease markers in the brains of *Cyfip2*$^{+/-}$ mice, detecting a 2.5-fold increase of CAMK2A (Calcium/Calmodulin-dependent protein kinase 2 alpha) and a 1.7-fold increase of APP levels without changes in the mRNA levels, consistent with a role of CyFIP2 in FMRP-dependent translational regulation (similar to CyFIP1). The authors also reported higher amyloid beta 42 ($A\beta_{42}$) levels and consequently a slight increase of the APP cleaving enzyme β-secretase 1 (BACE1), which was never observed in a FXS mouse model or patients. In line with the CAMK2A results, the *Cyfip2*$^{+/-}$ mice showed increased TAU phosphorylation on S214, one of the main CAMK2A phosphorylation sites that affects binding of TAU to microtubules, whereas the total TAU levels remained comparable to the controls. Lastly, *Cyfip2*$^{+/-}$ mice showed decreased mature spines and increased immature spines on apical CA1 dendrites and impaired long-term maintenance of spatial memory in a Morris water maze (MWM) task (Tiwari *et al.*, 2016).

1.2. The nervous system

The brain consists of two main types of cells, neurons and glia. Both neurons and glia are diversified in various subtypes, which differ in their specific gene expression and functions. Neurons can be distinguished into two broad classes, excitatory and inhibitory neurons. As the names suggest, the neurotransmitters released from these neurons depolarize or hyperpolarize the post-synaptic neuron, leading to its excitation or inhibition, respectively (Kandel *et al.*, 2012). Excitatory neurons are further divided into glutamatergic, cholinergic, serotonergic, noradrenergic, and dopaminergic neurons. Glutamatergic synapses constitute ~90 % of all release in the brain (Attwell and Laughlin, 2001). Compared to excitatory neurons, inhibitory neurons represent a much smaller fraction of the neurons. Nevertheless, there are over 25 different subtypes of GABAergic neurons with different morphological and electrophysiological properties (Parra, Gulyás and Miles, 1998; Pelkey *et al.*, 2017; Booker and Vida, 2018).

The second type of cells in the brain, glial cells, are distinguished in three different subtypes. Astrocytes are the most abundant type of glia and tile the entire CNS (Sofroniew and Vinters, 2010). A single mouse astrocyte is estimated to contact over 100,000 synapses by wrapping tightly around them (Bushong *et al.*, 2002). These star-shaped cells provide nutrients to neurons and help maintain the blood-brain barrier. They also maintain homoeostasis by secreting soluble factors that bind to the pre- and post-synaptic sites of both excitatory and inhibitory synapses. Recent studies revealed that peri-synaptic astrocyte processes contribute to remove the neurotransmitters released into the inter-synaptic space in order to prevent their accumulation (Allen and Eroglu, 2017; Murphy-Royal *et al.*, 2017). Additionally, astrocytes play important roles in maintenance of tissue integrity following injury. Upon inflammation, activated astrocytes release anti-inflammatory cytokines and chemokines (Jang *et al.*, 2013).

The second type of glia, oligodendrocytes, are the myelinating cells of the CNS. They ensheath many axons (with diameters above 0.2 μm) in multiple layers of myelin in order to decrease the capacitance of the neuronal membrane for long stretches and only allow propagation of action potentials at nodes of Ranvier, thus increasing the speed of synaptic transmission (Simons and Trajkovic, 2006; Bradl and Lassmann, 2010; Michalski and Kothary, 2015).

Lastly, microglia mediate immune responses in the central nervous system by acting as macrophages. Upon detecting foreign materials or pathogens, they phagocytose the material or the invading bacteria/virus and present antigens to T-cells which cross the blood-brain barrier (Aloisi, 2001; Perry and Teeling, 2013). Chronic inflammation, such as neurological degenerative disorders lead to activation of microglia (Thameem Dheen, Kaur and Ling, 2007). In addition to its role as an active defense system, microglia also regularly move through specific domains, surveying for damaged tissue, plaques, NFTs or apoptotic cells.

1.2.1. The synapse

Communication between neurons is achieved by signals that travel through contacts named synapses. Synapses are structures that consists of three main parts: the pre-

synaptic terminal, the synaptic cleft and the post-synaptic target, and that allow the transmission of action potentials from one neuron (pre-synaptic) to the next (post-synaptic), leading to its excitation or inhibition. There are two types of synapses: electrical and chemical. Electrical synapses are formed by a physical connection of the pre- and post-synaptic membranes (4 nm in between) through gap junctions that results in a continuous cytoplasm between the two neurons. Due to the physical connection of the pre- and post-synapse, ionic transmission between the neurons is almost instantaneous (Kandel *et al.*, 2012). In the mouse (the animal model used in this thesis), electrical synapses mainly connect glial cells. Conversely to the physically adhering electrical synapses, chemical synapses have a larger distance (20-40 nm) and an inter-synaptic space between the pre- and the post-synapse. As the name suggests, chemical synapses rely on the release of specific chemicals, called neurotransmitters, from the pre-synaptic site. This type of synaptic transmission is slower relative to the electrical synapse, producing a delay of 0.3-5 ms. While synaptic transmission in a chemical synapse is unidirectional, in the electrical synapses it is usually bidirectional (Andersen *et al.*, 2007; Kandel *et al.*, 2012; Pereda, 2014).

1.2.2. Synaptic transmission

Neurotransmission is a process where electrical signals or chemical molecules (neurotransmitters) are transferred across neurons. In the electrical synapse, an ionic current simply passes through the gap junctions that physically connect two cells, leading to changes in the membrane potential of the post-synaptic one. In the chemical synapse (Figure 5), synaptic vesicles located in pre-synaptic boutons are loaded with neurotransmitters by active transport. These vesicles are available for exocytosis upon the arrival of an action potential, which produces the rapid depolarization of the neuronal membrane. As a consequence, voltage-gated Ca^{2+} channels in the pre-synaptic site open. The opening of these channels leads to a significant increase of Ca^{2+} in the pre-synaptic site, which triggers the fusion of vesicles in the readily releasable pool to the pre-synaptic membrane. Exocytosis of the vesicles occurs only in restricted places, called active zones, on the pre-synaptic terminal. Fusion of vesicles to the pre-synaptic membrane releases the neurotransmitters into the synaptic cleft, where they diffuse into the extracellular space.

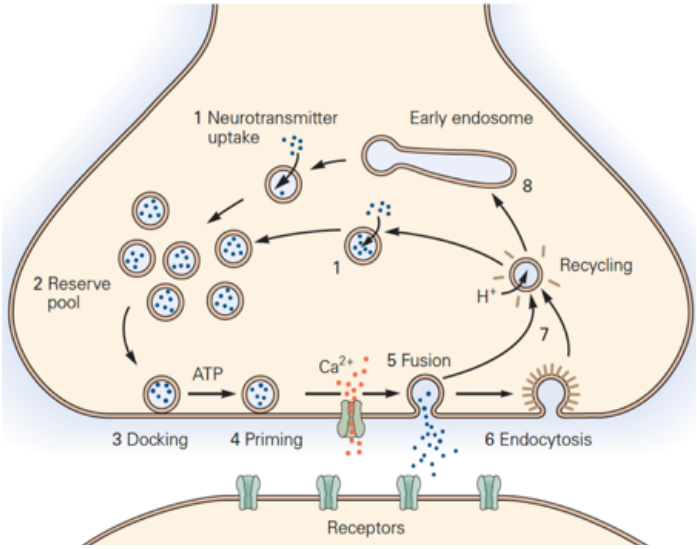

Figure 5. The synaptic vesicle cycle. In the pre-synaptic site, synaptic vesicles are (1) filled with neurotransmitters through active transport and (2) stored in the reserve pool (RP), ready to be translocated to the readily releasable pool (RRP) during synaptic activity. The vesicles from the RRP are (3) docked to the pre-synaptic membrane and (4) primed for release. Upon the arrival of an action potential, voltage-gated Ca^{2+} channels open, allowing Ca^{2+} entry into the pre-synaptic terminal. This leads to (5) the fusion of the synaptic vesicles to the synaptic membrane. After the neurotransmitters are released, the vesicle membranes are retrieved by (6) endocytosis and recycled (7) directly or (8) through endosomes. The recycled vesicles are again filled with neurotransmitters and the synaptic cycle is repeated (figure modified from Kandel et al. 2012).

The released neurotransmitters then bind to their respective receptors located on the post-synaptic site. This binding can either lead to a change in the membrane potential/conductance of the post-synaptic neuron by ion influx through specific channel receptors (short-term effect) or it can activate signaling cascades (long-term effect) that either leads to an excitation or an inhibition (Andersen *et al.*, 2007; Kandel *et al.*, 2012).

The exocytosis of the pre-synaptic vesicles is tightly regulated by pre-synaptic protein complexes. The SNARE (Synaptosome associated protein receptor) complex proteins on the vesicle and the plasma membrane of the pre-synaptic terminal mediate the temporally and spatially regulated exocytosis of the synaptic vesicles (Figure 6). The SNARE complex is composed of two components, the v-SNARE (SNARE proteins on the vesicles) and t-SNARE (SNARE proteins located on the target site, the plasma membrane). The v-SNARE in neurons mainly consists of synaptobrevin (or VAMP2 [Vesicle-associated membrane protein 2]), a protein that is crucial in calcium dependent vesicle fusion, whereas the t-SNARE is composed of SNAP25 (Synaptosome associated protein 25) and syntaxin. These proteins interact with each other through highly-conserved SNARE motifs to tether the synaptic vesicle to the membrane. A tight, stable bundle made of four helices forms, bringing together the synaptic vesicle and plasma membrane, thus keeping the vesicle ready for fusion and the release of neurotransmitters.

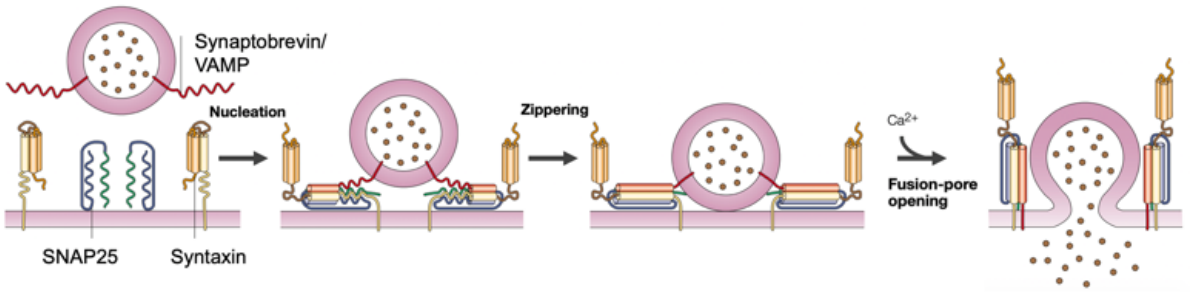

Figure 6. SNARE complex in synaptic vesicle exocytosis.
The vesicle associated v-SNARE complex protein VAMP and plasma membrane t-SNARE proteins syntaxin and SNAP25 form a tight, stable bundle that consists of four helices (two from SNAP25 and one each from syntaxin and VAMP). The helices of the bundle coil tightly in a process called zippering, which brings the vesicle into close contact with the plasma membrane. Upon Ca^{2+} entry into the pre-synaptic site a block is removed leading to the opening of a fusion pore, releasing neurotransmitters into the synaptic cleft (figure modified from Rizo and Südhof, 2002).

The released neurotransmitters bind to specific metabotropic and ionotropic (channel) receptors on the post-synaptic membrane. Neurons express mainly two types of ion channels: voltage-gated, which open in response to changes in membrane potential, and ligand-gated, that open upon binding of specific ligand molecules. Opening of these channels allows the influx of cations (Na^+, K^+, Ca^{2+}) or anions (Cl^-), leading to excitation or inhibition, respectively. Unlike the ionotropic receptors, metabotropic receptors do not have a channel that opens. Upon binding of a neurotransmitter, these receptors activate the G-proteins they are linked to. This activation in turn leads to activation of secondary messengers in the neuron. The excitatory neurotransmitter glutamate can bind to the ionotropic AMPA (α-amino-3-hydroxy-5-methyl-4-isoxazolepropionic acid), NMDA (N-methyl-D-aspartate), and kainate receptors, as well as to metabotropic (mGluR) receptors, inducing events leading to the depolarization of the post-synaptic neuron. The inhibitory neurotransmitter GABA (gamma-aminobutyric acid) is synthesized from glutamate by the glutamate decarboxylase enzyme. It can also bind to ionotropic and metabotropic receptors on the post-synaptic membrane to inhibit the activity of neurons (Kandel *et al.*, 2012).

A single post-synaptic neuron receives inputs from hundreds to thousands of different neurons. These inputs are summed up both spatially and temporally, allowing a very precise regulation of neuronal activity. If the excitatory inputs received by a post-synaptic neuron outnumber the inhibitory ones, the outcome might lead to an action potential. If the two are equal, they will cancel each other out. However if the number and strength of inhibitory inputs are higher than the excitatory ones, the neuron will be

inhibited, thus will not transfer the signal to other neurons (Andersen *et al.*, 2007; Kandel *et al.*, 2012).

1.2.3. Actin in the synapse

Synaptic development and transmission are robust processes that require tightly regulated cytoskeletal dynamics. Actin is the most abundant cytoskeletal protein in the synapse, playing crucial roles in its formation and maintenance, as well as dynamically regulating both the pre- and post-synapse during synaptic transmission. In the pre-synaptic site, actin helps to control synaptic vesicle exocytosis, while it is involved in many roles in the post-synapse, including the regulation of dendritic spine maturation (Figure 7).

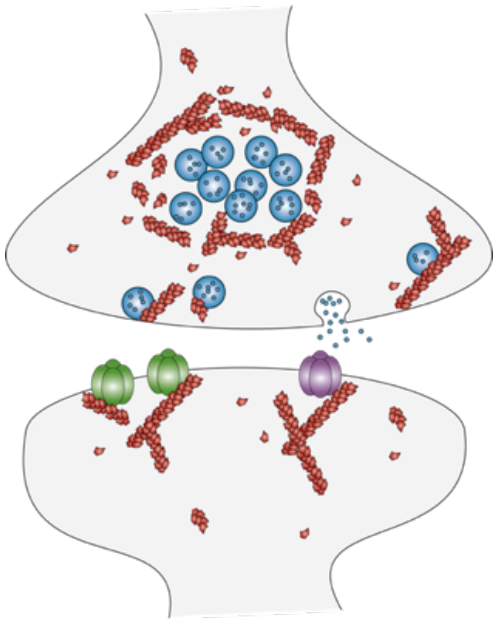

Figure 7. The actin cytoskeleton in the pre- and post-synapse.
In the pre-synaptic site, the actin network (red) confines the reserve pool of neurotransmitter loaded synaptic vesicles (blue). In addition, vesicles are translocated to the sites of release along actin fibers connecting the reserve pool to the readily releasable pool at the active zone. Actin dynamics are also required for vesicle reuptake. On the post-synaptic site, actin filaments form a network that anchors the post-synaptic density as well as targets the receptors (green and purple) to the post-synaptic membrane and confines their movement. Further to serving as a scaffold, actin cytoskeletal dynamics play crucial roles in synaptic plasticity. Upon stable stimulation from the pre-synaptic site, actin filaments rapidly polymerize in the post-synaptic density to sustain structural changes essential for long-term potentiation (LTP).

1.2.3.1. Actin in synaptogenesis

The formation of synapses is the basis for the development of neuronal circuits. During its development, a neuron forms many small protrusions, called neurites, which then differentiate into axon and dendrites. Neurites contain actin filaments and microtubules that help regulate their growth, shape and movement. At the beginning of neuronal development, all neurites have the potential to become an axon. At a certain point one of these neurites starts growing faster than the others, becoming the axon (Andersen

and Bi, 2000). Axon fate determination is an irreversible event that is strongly regulated by the local cytoskeleton dynamics. Studies showed that the neurite with the most dynamic growth cone (the distal end of a neurite rich in actin filaments) is most likely to become the axon (Ledesma and Dotti, 2003). When the actin polymerization inhibitor Cytochalasin D was added to cultured hippocampal neurons, multiple axons formed due to the microtubules extending to the lamellipodia at the ends of neurites (Bradke and Dotti, 1999). It was later shown that the determination of an axon relies on the stabilization of these microtubules (Witte, Neukirchen and Bradke, 2008).

A growth cone is a motile structure at the distal tip of an elongating neurite, prevalently consisting of a dense mesh of actin filaments that bundle or network into filopodia-like micro spikes and lamellipodia necessary to guide the neurite according to external cues. During the development of the brain, the receptors on the growth cone membrane of an axon recognize attractive and repulsive guidance cues (netrin, ephrins, semaphorins as well as adhesion molecules) that help the axon to reach its target sites (Graus-Porta *et al.*, 2001). There, a part of the growth cone is transformed into a pre-synaptic terminal.

1.2.3.2. Actin in pre-synaptic boutons

As mentioned earlier in chapter 1.2.2, pre-synaptic boutons (or terminals) are small distal bulging compartments of axons filled with synaptic vesicles. In the pre-synaptic site, three different pools of synaptic vesicles exist: reserve pool (RP), readily releasable pool (RRP) and recycling pool (Denker and Rizzoli, 2010). The RP consists of synaptic vesicles located at the center of the bouton, surrounded by an actin network (Dillon and Goda, 2005). Vesicles of the RRP, primed for exocytosis upon Ca^{2+} entry, reside in the active zone and are linked to the actin cytoskeleton through short filaments of synapsin 1 (Hirokawa, 1989). In the pre-synaptic site, actin is thought to function as a physical barrier that restricts the vesicle fusion with the membrane, as well as a facilitator for the docking of RRP vesicles for neurotransmitter release (Pilo Boyl *et al.*, 2007). Studies using the actin polymerization inhibitor latrunculin A have demonstrated an increase of neurotransmitter release upon its application to cultured neurons, indicating that actin indeed participates in a regulatory mechanism that

restrains fusion of synaptic vesicles at the active zone (Morales, Colicos and Goda, 2000). In addition to its roles in the RP and RRP, the actin cytoskeleton plays important roles in the recycling pool. When the F-actin stabilizing peptide jasplakinolide was added on acute rat brain slices, the distribution of recycling vesicles in the synapse was disturbed, thus indicating a function for the actin cytoskeleton in facilitating the repositioning of recycling vesicles towards the active zone after endocytosis (Marra *et al.*, 2012).

1.2.3.3. Actin in dendritic spines

Dendritic spines are the post-synaptic membrane protrusions of dendrites, which generally receive inputs from a single excitatory pre-synaptic terminal (Nimchinsky, Sabatini and Svoboda, 2002). A dendritic spine contains many receptors on its membrane, usually concentrated opposite to the pre-synaptic active zone. This region, termed post-synaptic density (PSD), is enriched in cytoskeletal proteins as well as receptors, channels and signaling molecules. Dendritic spines have different morphological characteristics depending on their maturity level. An immature spine appears as a long, thin, filopodia-like structure, sometimes with a small bulb on the distal end. On the other hand, a mature spine can be described as mushroom-shaped or stubby, having a large bulb on a shorter or very short and thick neck, respectively (Peters and Kaiserman-Abramof, 1970; Miermans *et al.*, 2017).

The actin cytoskeleton is fundamental for the dynamic changes occurring in dendritic spine morphology during synaptic plasticity, which are considered as the structural basis of learning and memory (Figure 8). Upon receiving a high frequency pre-synaptic input, cellular and morphological changes are observed in the post-synapse (Bliss and Lømo, 1973). This process, called long-term potentiation (LTP), leads to increased synaptic strength by induction of signaling pathways (such as CAMK2) that recruit scaffold proteins, which in turn recruit more receptors to the PSD (Herring and Nicoll, 2016). Upon LTP induction, actin polymerization increases in the spines and networks of branched actin filaments form a stable mature spine. Studies using actin polymerization inhibitors demonstrated that actin polymerization is fundamental for the maintenance of LTP (Krucker, Siggins and Halpain, 2000).

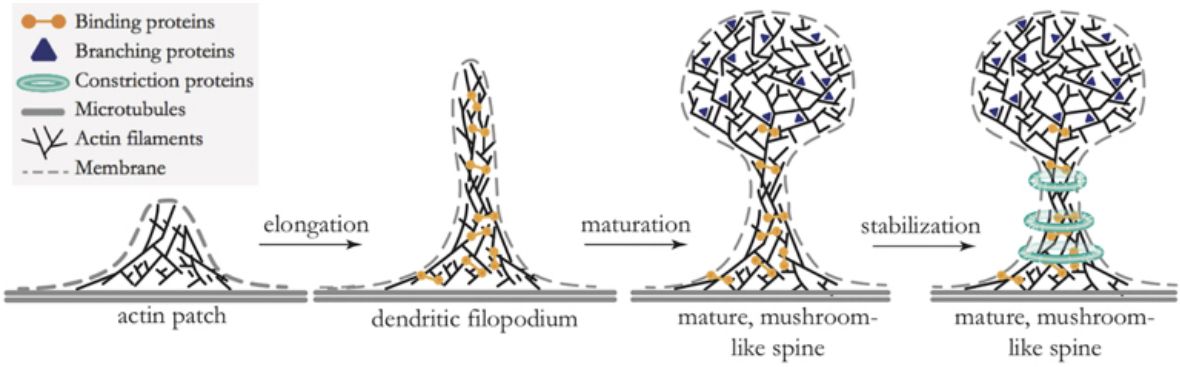

Figure 8. The actin cytoskeleton in spine maturation and stabilization.
Actin polymerization and branching is crucial in the maturation and maintenance of spines. During the formation of the thin (filopodia-like) spine, actin binding proteins (orange) such as α-actinin might be involved in the elongation of the filaments. Maturation requires branching of actin filaments into stable tree-like structures with the help of branching nucleators (dark blue), such as the ARP2/3 complex. Lastly, ring-like F-actin complexes form the neck of the spine leading to stabilization and maintenance of dendritic spines (figure modified from Miermans *et al.*, 2017).

The formation of a stable spine with a network of branched actin filaments requires the ARP2/3 complex. Knockdown of the ARP2/3 complex subunit ARPC2 using siRNAs in mouse hippocampal neurons resulted in the loss of spine heads (Hotulainen *et al.*, 2009). Additionally, studies on ARP2/3 conditional knockout mice showed that the complex is involved in the recruitment of glutamate binding AMPA receptors, demonstrating a role for ARP2/3 in the unsilencing of dendritic spines during synaptogenesis (Spence *et al.*, 2016). In *Drosophila*, the WRC was shown to link a diverse set of receptors and ion channels as well as neuroligins, protocadherins and netrin receptors to the actin cytoskeleton (Chen *et al.*, 2014).

1.3. Dementia

Dementia is a term that defines symptoms of cognitive decline and confusion severe enough to affect a person's daily life. Common symptoms include memory defects, concentration problems, difficulty in language and communication and reasoning (Livingston *et al.*, 2017). The main cause of dementia is synaptic or neuronal loss, leading to defects in synaptic transmission. This loss can be restricted to a neuron type (*e.g.* loss of dopaminergic neurons in Parkinson's disease) or to a certain region of the brain (*e.g.* neuronal loss in the hippocampus in early Alzheimer's disease).

1.3.1. Alzheimer's disease

Alzheimer's disease (AD) is the most common form of dementia, accounting for ~70 % of all cases. It is a progressive disease that worsens over time, mostly observed in humans above 65 years of age (Crous-Bou *et al.*, 2017; Lane, Hardy and Schott, 2018). In 1907, the German psychiatrist Alois Alzheimer used a silver staining method on the post-mortem brain tissue of a 55-year old patient to describe abnormal structures such as inter-neuronal clumps (so called amyloid plaques) and tangled bundles of fibers (neurofibrillary [TAU] tangles). The patient had severe memory defects with paranoia, sleep disorders and progressive confusion (Hippius and Neundörfer, 2003).

Histologically, Alzheimer's disease is characterized by the deposition of extracellular amyloid-β (Aβ) plaques and intracellular neurofibrillary tangles (NFT). As the disease progresses, major synaptic and neuronal loss occurs in the entorhinal cortex, hippocampus, amygdala and neocortex (Ingelsson *et al.*, 2004). NFTs are aggregates of hyperphosphorylated TAU proteins. In a healthy neuron, TAU proteins help axonal transport of vesicles and organelles, as well as providing structural support. Upon hyperphosphorylation they detach from microtubules, forming aggregates inside the neuron and leading to defects in axonal transport (Torres *et al.*, 2012). The second hallmark of AD are the Aβ plaques, which form as a result of the aberrant cleavage of the amyloid precursor protein (APP). APP processing is further explained in the next chapter (1.3.1.1).

Thus far, the cause of AD has not been clearly identified. However, there are two main hypotheses. The first one is the amyloid cascade hypothesis that suggests Aβ plaque accumulation as the causative factor for AD, which is followed by NFT formation, neuronal and synaptic loss (Hardy and Higgins, 1992). While almost all AD patients have been shown to display Aβ pathology, positron-emission tomography (PET) studies have shown a group of individuals with considerable amounts of amyloid aggregates in their brains without showing any cognitive defects (Aizenstein *et al.*, 2008). Thus, the existence of Aβ plaques alone might not be the cause of AD. The second hypothesis for the cause of AD is the TAU hypothesis, which suggests that the

hyperphosphorylated TAU aggregates are the cause of the disease. Studies have reported occurrence of TAU lesions before Aβ plaques in AD patients, leading to cognitive decline (Braak and Del Tredici, 2015; Bejanin *et al.*, 2017).

1.3.1.1. APP processing

APP is a highly conserved transmembrane protein expressed in many tissues. In the brain, APP is expressed predominantly in synapses. In the adult human brain, the role of APP is still poorly understood. However, a broad range of studies have shown many important functions for the cleavage products of APP in CNS pathology during aging.

Under normal (healthy) conditions, the processing of APP occurs via a non-amyloidogenic pathway (Figure 9). APP is initially cleaved by an extracellular α-secretase (a disintegrin and metalloproteinase domain-containing protein [ADAM]), ADAM10 or ADAM17, which releases the soluble APPsα (α-secretase-generated APP ectodomain fragment) to the extracellular space. Subsequently, the transmembrane region of APP is cleaved by the γ-secretase liberating the small p3 peptide and the APP intracellular domain (AICD). The γ-secretase is a transmembrane protease complex composed of four different proteins: Presenilin 1 or 2 (PSEN1 or PSEN2), nicastrin, anterior pharynx-defective 1 (APH-1) and presenilin-enhancer 2 (PEN-2) (Edbauer *et al.*, 2003).

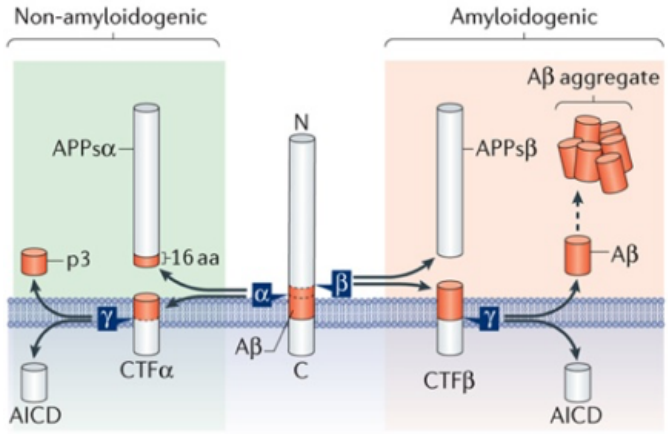

Figure 9. Processing of the amyloid precursor protein.
The transmembrane amyloid precursor protein is processed in two different pathways. In the non-amyloidogenic pathway, the amyloid-β region (shown in red) is cut by the enzyme α-secretase. This leads to the release of the soluble APPsα fragment into the extracellular space. The cleavage of the transmembrane domain then generates the soluble p3 peptide, which is also released into the extracellular space. Instead, in the amyloidogenic pathway, through β- secretase and γ-secretase cleavage, an APPsβ (β-secretase-generated APP ectodomain fragment) fragment and the toxic Aβ peptides are released. The insoluble Aβ fragments aggregate in the extracellular space, forming plaques. In both pathways, the C-terminal fragment (CTF) of APP generates the APP intracellular domain (AICD) upon γ-secretase cleavage (figure modified from Müller, Deller, and Korte 2017).

In contrast, in the amyloidogenic pathway, APP is cleaved extracellularly by the β-secretase (beta-site amyloid precursor protein cleaving enzyme 1 [BACE1]) that cuts 16 amino acids further towards the N-terminus. When the γ-secretase cuts the transmembrane region of the cleaved APP, it releases a 39-43 amino acid Aβ peptide. The insoluble $A\beta_{42}$ peptides aggregate in the extracellular space as oligomers, forming Aβ plaques (O'Brien and Wong, 2011; Müller, Deller and Korte, 2017).

1.3.1.2. Mouse models for Alzheimer's disease

In humans, APP is located on Chromosome 21. Over 65 mutations of the gene have been identified at different sites (*e.g.* close to the β-cleavage site, in the Aβ region or in the γ-cleavage site), leading to different AD development (Elder, Gama Sosa and De Gasperi, 2010). The most common mutations of APP occur through alternative splicing of exons 7 and 8, leading to different lengths of APP (APP_{695}, APP_{751} and APP_{770}). The longer forms of the gene cause more severe AD phenotype (Esquerda-Canals *et al.*, 2017). A common mutation at the β-cleavage site is the Swedish double mutation (APP_{Swe} – K670N/M671L) that favors BACE1 cleavage, which increases Aβ production. In the Aβ region, Flemish (A692G), Dutch (E693Q) and Italian (E693K) mutations are identified, which lead to increased Aβ accumulation in the neurons as well as blood vessel walls. Mutations at the γ-cleavage site (London [V717I], Indiana [V717F], Florida [I716V] and German [V715A]) do not lead to changes in total Aβ level, however the ratio of toxic $A\beta_{42}$ peptides is increased compared to the soluble $A\beta_{40}$ peptide (Esquerda-Canals *et al.*, 2017). In addition to the *APP* gene, more than 230 mutations in the *PSEN1* locus are described. Finally, M146V/L, L286V and ΔE9 mutations alter *BACE1* activity, hence triggering $A\beta_{42}$ production (Shen and Kelleher, 2007).

The study of AD in mice requires the generation of transgenic models since rodents do not spontaneously develop AD (Kasza *et al.*, 2017; Mullane and Williams, 2019). In order to induce Aβ accumulation and memory defects in mice, mutated human APP and/or PSEN1 genes are expressed in transgenic mice. The PDAPP mouse line is the first transgenic AD mouse line generated, which overexpresses all three isoforms of APP under the *Pdgf* promoter. Starting at ~4 months of age, the mice show spatial

memory deficits in MWM and Aβ accumulation at ~6-9 months of age (Games *et al.*, 1995). The Tg2576 and APP23 models both overexpress the APP_{Swe} under *Prp* and *Thy-1* promoters, respectively. Since the APP23 mice express APP_{751}, they show amyloid plaques and spatial memory defects earlier than the Tg2576 mice that express APP_{695}. While the APP23 mice show neuronal loss in the CA1 region of the hippocampus, Tg2576 mice do not show any neuronal loss (Sturchler-Pierrat *et al.*, 1997; Esquerda-Canals *et al.*, 2017).

Mouse models with PSEN1 mutations alone show increased $Aβ_{42}$ production without accumulation of amyloid plaques (Raux *et al.*, 2000; Amtul *et al.*, 2002; Dermaut *et al.*, 2004). For this reason, bigenic lines with mutations in both APP and PSEN1 genes were developed. These mouse lines have an earlier onset of the disease, with faster rates of pathogenesis compared to single APP or PSEN1 transgenic lines. The most widely used line is the PSAPP, which is a crossing of APP_{Swe} and $PSEN1_{M146L}$ transgenic lines. In these mice, Aβ deposits develop in the cerebral cortex and hippocampus at ~6 months of age. The PSAPP mice already show spatial working memory deficits at ~3 months of age in a Y-maze test (Holcomb *et al.*, 1998).

1.3.2. Behavioral paradigms

The study of AD models in mice requires the assessment of memory deficits by using different behavioral paradigms. Due to its vulnerability to damage at the earlier stages of AD as well as its crucial role in learning and storage of memory, the hippocampus is considered an important region of the brain to study AD pathophysiology. In this chapter four general tests that aim to study hippocampal-dependent memory deficits in AD mice will be explained: Y-maze (or T-maze), radial arm maze (RAM), novel object recognition (NOR) test and MWM.

The Y-maze is a test used to assess spatial working memory in mice by using their preference to choose new environments for exploration (Hughes, 2004). In this test, the mouse is placed in a maze composed of three arms (X, Y and Z) oriented at an angle of 120° (or in a T shape for the T-maze). As mice have a preference for novel environments, the mouse is expected to enter the arms in an alternating sequence

(*e.g.* X-Y-Z). A failure (*e.g.* X-Y-X) is scored as a defect in working memory of the mouse to remember the last arm it has visited. The RAM has a similar working principle as the Y-maze, but it usually involves a food reward at the end of one of the eight arms. The latency of a mouse to find the arm with the reward is used as indicative of reference memory, whereas working memory is assessed by the alternation of the arms during the exploration phase to find the food reward (as the mouse should visit in sequence each arm a single time) (Olton and Samuelson, 1976).

In a NOR test, the short-term memory of mice is assessed by taking advantage of the preference of mice to explore novel objects. During the habituation phase, the mouse is placed in an empty arena to freely explore the environment. The following day, two identical objects are placed in the arena for the mouse to explore. After a certain time (one hour or one day later, for the assessment of short or long-term memory, respectively), one of the objects is replaced by a different one. The time that the mouse spends on the novel object is used as an indicator of memory (Bevins and Besheer, 2006; Leger *et al.*, 2013).

The MWM is a test developed by Richard Morris in 1981 using rats, which serves as a fundamental technique in the study of spatial memory in rodents. The test does not depend on any visual, auditory or olfactory cues but rather on the escape behavior of the animal (Morris, 1981). The MWM uses a circular arena filled with water, including an escape platform. To test spatial working memory, the animal is placed in the maze during a series of sample trials where it is trained to reach the location of a visible platform to escape the water. In the following test trial, the swimming path and the animal's latency to reach the platform is used as an indicator of spatial working memory. In another version of MWM, learning trials are performed in which the swimming pattern of the animal is recorded. After the platform is removed, the time that the animal spends in the vicinity of the platform area is used as an indication of spatial memory (D'Hooge and De Deyn, 2001; Vorhees and Williams, 2006).

1.4. The *Cyfip2*$^{flx/flx}$*;Camk2a-Cre* mouse model

As mentioned earlier (in chapter 1.1.5), the complete knockout of the *Cyfip2* gene leads to perinatal lethality of mice, which makes it impossible to study the role of CyFIP2 in the adult mouse brain. This problem can be overcome by the generation of a conditional knockout mouse model, which was achieved by the deletion of *Cyfip2* in the hippocampus and cortex using the Cre/loxP system (Figure 10).

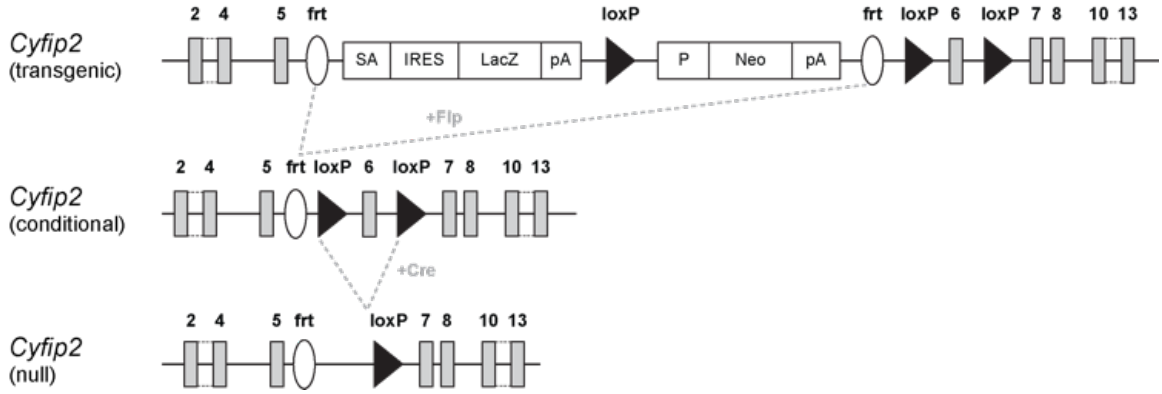

Figure 10. Generation of the *Cyfip2*$^{flx/flx}$*;Camk2a-Cre* mouse.
(Top) Transgenic *Cyfip2* locus, containing a splice acceptor site (SA) and an internal ribosomal entry site (IRES) followed by the *LacZ* gene and its polyA (pA) signal; a β-actin promoter (P), neomycin resistance gene (Neo) with its pA signal were used for ES cell selection (EUCOMM). Two frt sites flanked the insertion, which was deleted via Flp-recombination, generating the conditional or flox allele (middle). The flox allele containes two loxP sites flanking exon 6, which was cut out when the flox mice were crossed with mice expressing the Cre recombinase under the *Camk2a* promoter. This resulted in a conditional knockout offspring (bottom), where the *Cyfip2* gene was deleted (by excision of exon 6 and disruption of the translation frame) only in the cells that expressed *Camk2a-Cre*.

Cyfip2 conditional knockout mice were generated by crossing *Cyfip2*$^{flx/flx}$ mice, which contain the loxP sites flanking the exon 6 of the *Cyfip2* gene, with *Camk2a-Cre* mice that express the Cre recombinase under the minimal promoter of the *Camk2a* (Minichiello *et al.*, 1999). CAMK2 is a serine/threonine kinase that plays important roles in synaptic plasticity and memory consolidation (specifically the induction and maintenance of long-term potentiation) (Burgin *et al.*, 1990; Benson *et al.*, 1992). The CAMK2A isoform is highly expressed in the *Cornu Ammonis* (CA) pyramidal neurons and dentate gyrus (DG) granular neurons of the hippocampus, in principal neurons of the cortex and in medium spiny neurons of the striatum (Liu and Murray, 2012). Thus, the crossing of the *Cyfip2*$^{flx/flx}$ and *Camk2a-Cre* mice lead to deletion of the *Cyfip2*

gene in mainly glutamatergic neurons of the cortex and hippocampus, starting at postnatal day (P) 18.5 (Minichiello *et al.*, 1999).

1.5. Aim of the thesis

Studies on the role of CyFIP have been mainly focused on the ubiquitously expressed CyFIP1 paralogue. Due to the perinatal lethality of *Cyfip2*$^{-/-}$ mice, the function of the brain prominent paralogue has only been studied using heterozygous animals. Although its importance in embryonic development is evident from the perinatal lethality phenotype, the role of CyFIP2 in the brain and in neuronal physiology has so far been investigated to a limited detail in adult mice.

In this thesis, we aimed to explore three main aspects of the function of CyFIP2 in the adult mouse brain using the *Cyfip2* conditional knockout mouse line. Firstly, we identified the expression pattern of CyFIP2 in different neuronal and non-neuronal subtypes by immunofluorescence. Secondly, we explored the role of CyFIP2 in synaptic transmission by electrophysiological recordings, as well as its role in synaptic morphology by electron microscopy. Lastly, we investigated potential Alzheimer's- and FXS-like phenotypes upon CyFIP2 loss with biochemical, anatomical, and behavioral approaches in aged mice.

2. Results

2.1. CyFIP2 expression in the mouse brain

Studies on CyFIP2 have hitherto failed to focus on the expression profile of CyFIP2 in adult mouse tissues, due to a lack of specific tools. For this reason, our research group has produced a CyFIP2 specific monoclonal antibody (named 1C4) that can detect CyFIP2 in western blotting and immunoprecipitation (Hauck, unpublished) and that has been optimized for immunofluorescence staining in this work. Using specific markers for neuronal and glial subtypes, the expression profile of CyFIP2 was determined by co-immunofluorescence staining on paraffin-embedded coronal slices of *Cyfip2*$^{flx/flx}$ mouse brains (see chapter 4.3.4).

2.1.1. Glutamatergic neurons express CyFIP2

Glutamatergic neurons constitute the majority (~80-85 %) of the neurons in the cortex and hippocampus, providing the main excitatory input to most neurons in these and surrounding regions. These glutamate releasing neurons are in fact termed principal neurons and in the cortical and hippocampal regions are subdivided in pyramidal and granular neurons. Pyramidal neurons are characterized by their large triangular cell bodies and long, thick apical dendrites. Granular neurons are on the contrary characterized by small round cell bodies and typically form more compact layers.

Studies using the *Cyfip2-lacZ* reporter mouse model showed the expression of CyFIP2 in all cortical layers and in the hippocampus cell body layer. This expression pattern paralleled the layering of glutamatergic neurons populations, suggesting that they may express CyFIP2. In order to verify this hypothesis, co-stainings were performed using the anti-CyFIP2 antibody and the glutamatergic neuron marker neurogranin (NRGN). NRGN is a calmodulin-binding protein that is specifically expressed in principal neurons of cortex and hippocampus (Singec *et al.*, 2004). NRGN stains the cell bodies and dendrites of glutamatergic neurons.

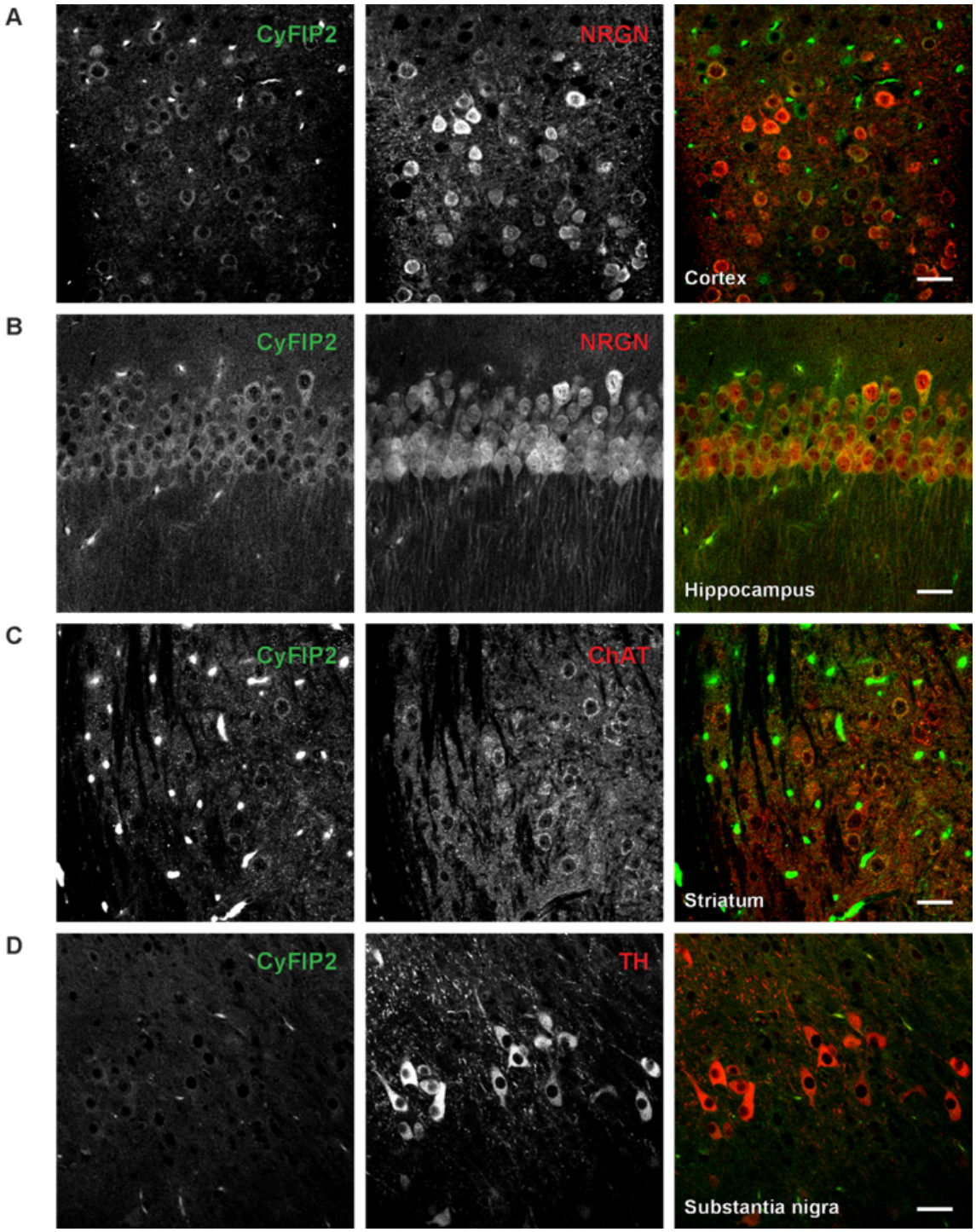

Figure 11. CyFIP2 is expressed in glutamatergic and cholinergic neurons.
Co-stainings performed with an antibody against CyFIP2 (green) and the glutamatergic neuron marker NRGN (red) show co-localization of signals in (A) the cortex and (B) CA1 region of the hippocampus of *Cyfip2*$^{flx/flx}$ mice at age P80. (C) CyFIP2 (green) is expressed in cholinergic neurons identified by ChAT (red) expression. (D) Dopaminergic neurons (red) stained with an anti-TH antibody do not show detectable CyFIP2 (green) expression. Scale bar: 20 µm.

Immunofluorescence stainings showed co-localization of the signals from CyFIP2 and NRGN in cortical (Figure 11A) and hippocampal CA1 (Figure 11B) pyramidal neurons,

proving that glutamatergic neurons express CyFIP2. All NRGN-positive cells were co-stained with an anti-CyFIP2 antibody, showing that CyFIP2 expression is ubiquitous in the glutamatergic neuron population. In addition to the glutamatergic neurons, we analyzed CyFIP2 expression in other excitatory neurons. In co-stainings, CyFIP2 expression was seen in striatal cholinergic neurons (Figure 11C), labeled with an antibody detecting the enzyme choline acetyltransferase (ChAT) that synthesizes the neurotransmitter acetylcholine. However, TH (tyrosine hydroxylase) positive dopaminergic neurons of the substantia nigra pars compacta (Figure 11D) and VTA (not shown) were devoid of detectable CyFIP2 expression.

These data overall showed expression of CyFIP2 in glutamatergic and cholinergic neurons, while CyFIP2 was lacking from the dopaminergic neurons in the brain.

2.1.2. Glial cells are devoid of CyFIP2

Glial cells, the most abundant cell population in the brain, surround neurons to provide support and insulation, as well as maintain homeostasis. There are three main types of glia: astrocytes, oligodendrocytes and microglia.

To investigate whether glial cells express CyFIP2, we performed co-stainings of CyFIP2 with the microglia marker ionized calcium-binding adaptor molecule 1 (IBA1), the mature astrocyte marker S100 calcium-binding protein β (S100β) and the oligodendrocyte marker myelin basic protein (MBP). When the signals of CyFIP2 and glial markers were compared, no co-localization was observed, suggesting that glial cells are devoid of CyFIP2 (Figure 12). These results were in agreement with previous studies that showed the absence of CyFIP2 in a mixed glial culture by western blotting (Tiwari and Suresh, 2016).

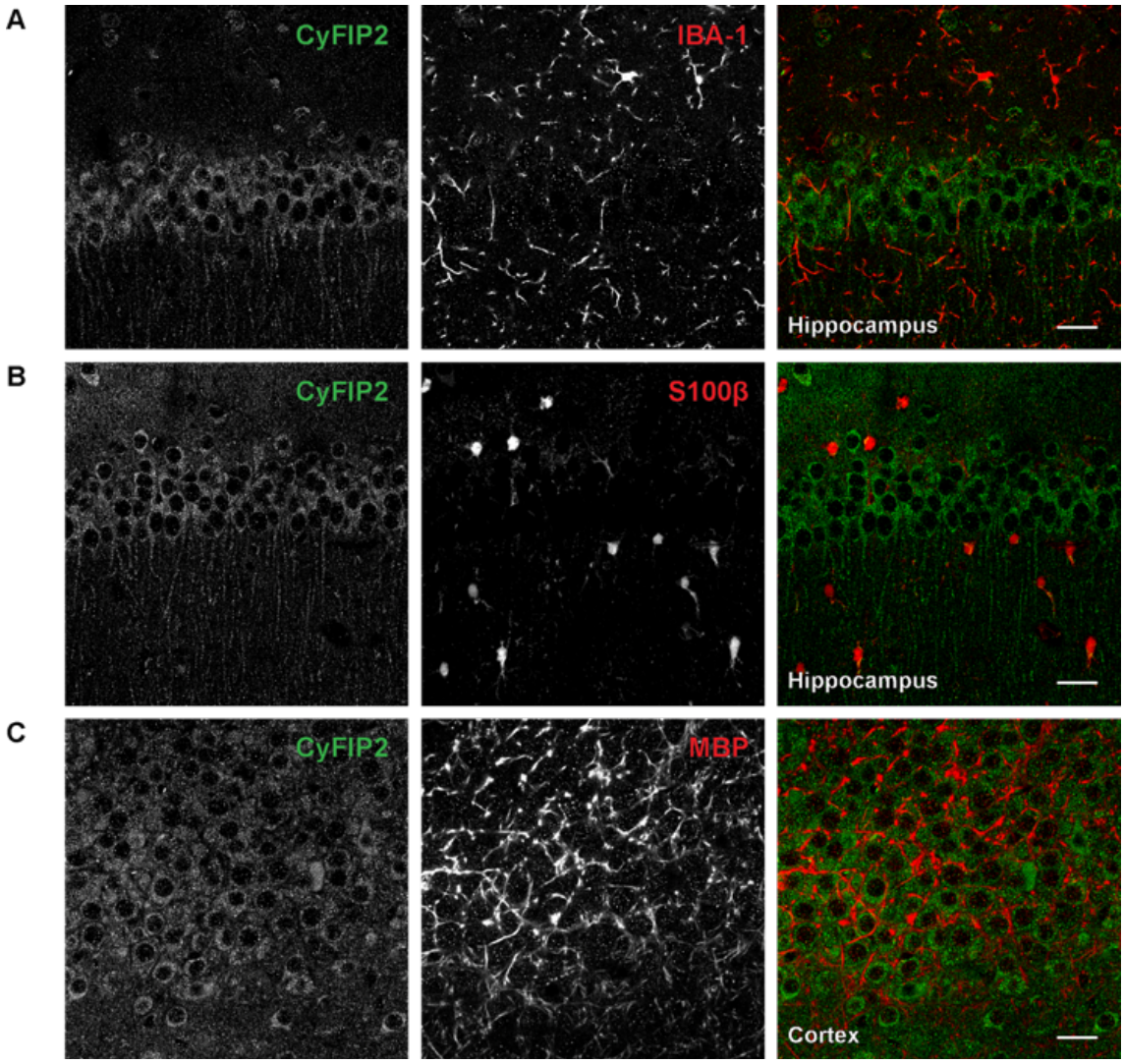

Figure 12. Glial cells do not express CyFIP2.
CyFIP2 (green) co-stainings with (A) microglia – IBA1, (B) astrocyte – S100β and (C) oligodendrocyte – MBP markers (red) show no co-localization of signals in the brains of *Cyfip2*$^{flx/flx}$ mice at age P80, indicating that glial cells do not express CyFIP2. Scale bar: 20 µm.

2.2. Analysis of *Cyfip2* conditional knockout mice

Compared to its paralogue CyFIP1, the role of CyFIP2 has not been extensively studied in adult mice due to the perinatal lethality of *Cyfip2*$^{-/-}$ mice (see chapter 1.1.5). In order to study the role of CyFIP2 in a developed organism, a conditional knockout mouse model was created (see chapter 1.4) using the Cre/loxP system. A Cre recombinase under the control of a minimal *Camk2a* promoter (Minichiello *et al.*, 1999) was used to delete CyFIP2 mainly in glutamatergic neurons of the cortex and hippocampus, starting at ~P18. The following chapters will provide a biochemical,

morphological, physiological and behavioral characterization of this *Cyfip2* conditional knockout mouse model.

2.2.1. CyFIP2 has a long half-life *in vivo*

To quantify CyFIP2 loss in the cortex and hippocampus of the conditional knockout mouse, total tissue lysates were prepared from *Cyfip2*$^{flx/flx}$*;Camk2a-Cre* mice at ages P21, P28, P40, P70, P130 and P330. Equal amounts of protein lysates were loaded on an SDS-PAGE and the level of CyFIP2 was analyzed by western blotting (Figure 13). Calibration was performed by Coomassie staining on the membranes (as explained in chapter 4.2.4.3.1).

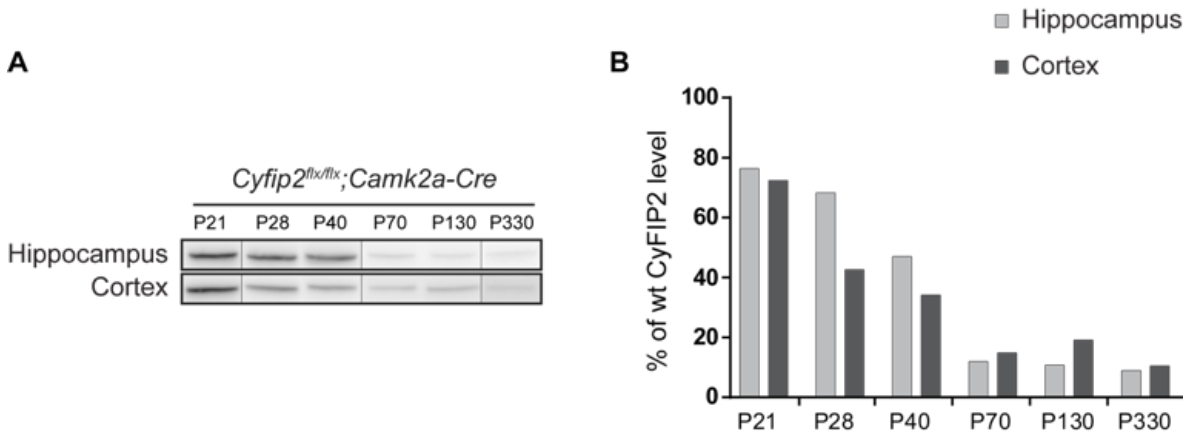

Figure 13. CyFIP2 has a long half-life.
(A) Western blots of membranes probed with anti-CyFIP2 antibody, showing the levels of CyFIP2 in hippocampus and cortex of *Cyfip2*$^{flx/flx}$*;Camk2a-Cre* mice at different postnatal ages (P21, P28, P40, P70, P130 and P330). (B) Quantification of CyFIP2 protein levels of *Cyfip2*$^{flx/flx}$*;Camk2a-Cre* mice compared to age-matched *Cyfip2*$^{flx/flx}$ controls show a complete deletion of the protein at P70 in glutamatergic neurons (the remaining 10 % is likely the CyFIP2 in other cell types). Coomassie stainings performed on the membrane were used as calibration control. n=2 animals per genotype.

In both cortex and hippocampus of *Cyfip2* conditional knockout mice, compared to controls (*Cyfip2*$^{flx/flx}$ mice), ~75 % of the protein was present at P21 (~3 days after the deletion). CyFIP2 level decreased to ~40 % at P40. Finally, at P70 CyFIP2 level decreased to ~10-15 % and remained stable throughout the rest of adulthood. This remaining ~10-15 % of CyFIP2, given its stability in time, is likely the expression of the protein in cell types other than glutamatergic neurons. Even compared to the generally long half-life of proteins in the brain, CyFIP2 appeared to have a slower turnover (~12

days). Due to this long half-life, all experiments described in the following chapters were performed in mice older than P70.

2.2.2. WRC components are co-regulated with CyFIP2

CyFIP is a crucial component of the WRC, serving as a scaffold (together with NAP1) for the binding of WAVE, ABI and HSPC300 (see chapter 1.1.3). CyFIP2 forms a distinct WRC together with NAP1, HSPC300, ABI1/2 and WAVE1/3 (Beuck, unpublished). In light of these studies and the role of CyFIP2 as a scaffold in the WRC, we analyzed the levels of WRC proteins in wt (+/+), *Cyfip2*$^{flx/flx}$ and *Cyfip2*$^{flx/flx}$*;Cam2a-Cre* mice (Figure 14).

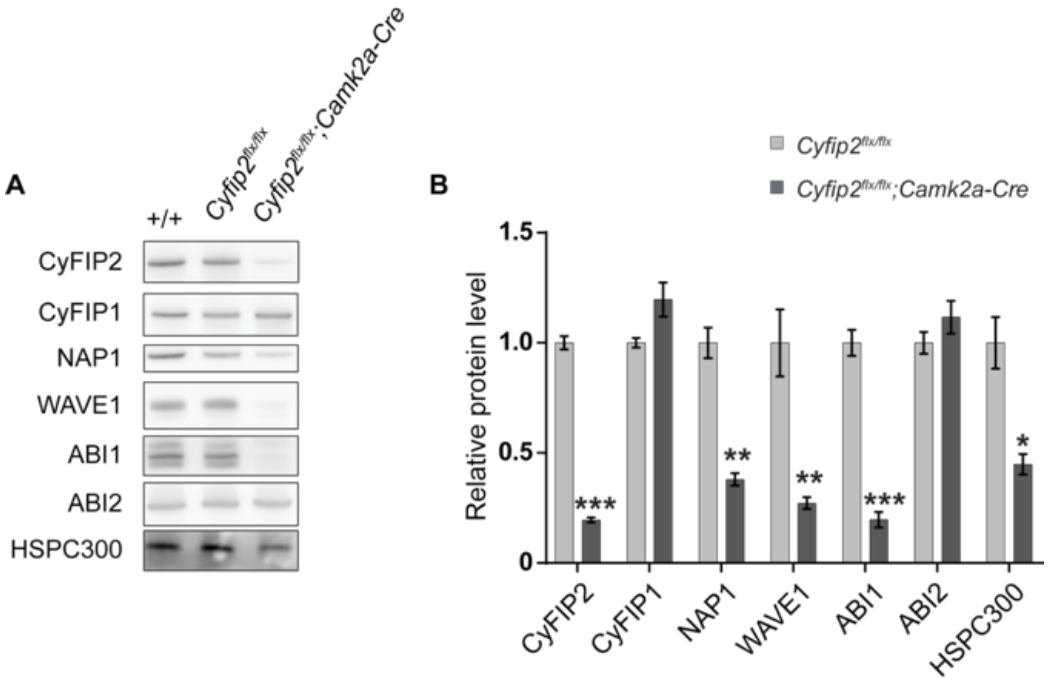

Figure 14. Expression levels of select WRC components are decreased in response to CyFIP2 loss.
(A) Representative western blot comparing the level of different WRC protein in the hippocampus of wt (+/+), *Cyfip2*$^{flx/flx}$ and *Cyfip2*$^{flx/flx}$*;Camk2a-Cre* mice at age P70. (B) Quantification of WRC proteins relative to *Cyfip2*$^{flx/flx}$ control mice shows decreased levels of CyFIP2 ($p=2x10^{-4}$), NAP1 (p=0.001), WAVE1 (p=0.009), ABI1 ($p=3x10^{-4}$) and HSPC300 (p=0.012). CyFIP1 levels showed a tendency for increase, although not significantly (p=0.071). ABI2 levels were conserved following CyFIP2 loss (p=0.261). Coomassie stainings performed on the membranes were used as calibration control. n=3 animals per genotype. Two-tailed t-test; *p<0.05, **p<0.01, ***p<0.001. Error bars represent s.e.m.

Hippocampal total lysates were prepared from mice at age P70 and proteins of the WRC were analyzed using western blotting. Compared to the wild-type mice,

Cyfip2$^{flx/flx}$ mice did not differ in the levels of the WRC proteins (Figure 14A), showing that the loxP sites did not significantly affect CyFIP2 expression. In the hippocampus of the conditional knockout mice, instead, CyFIP2 decreased to ~20 %. Upon CyFIP2 loss, CyFIP1 protein levels were not significantly altered, although tendentially increased. This result was in line with the studies on *Cyfip2*$^{+/-}$ mice, which also showed conserved CyFIP1 levels (Tiwari *et al.*, 2016). The expression levels of the WRC members that form a complex together with CyFIP2, namely NAP1, WAVE1, ABI1 and HSPC300 were all significantly decreased upon *Cyfip2* deletion. ABI2 levels showed no change in expression, although in a different approach it appeared to participate in a complex with CyFIP2 (Beuck, unpublished). WAVE2 and WAVE3 expression levels showed high variances between the animals (data not shown), indicating that they might be regulated by external factors. Overall, the loss of CyFIP2 led to a decrease in the expression of a specific WRC (the CyFIP2-NAP1-WAVE1-ABI1-HSPC300) whereas CyFIP1 levels remained relatively unchanged, indicating that it participates in a different coexisting complex.

2.2.3. CyFIP2 loss leads to an increase of small actin filaments

The loss of CyFIP2 and the subsequent decrease in the protein levels of its WRC partners, which together are a major activator of the branched actin nucleation factor ARP2/3 complex, may lead to changes in actin dynamics. Previous studies on hippocampal lysates of *Cyfip1*$^{+/-}$ mice showed higher F/G-actin ratio compared to wt littermates (Hsiao *et al.*, 2016). In order to detect changes in actin polymerization, different cellular fractions were prepared from the forebrains of *Cyfip2*$^{flx/flx}$ and *Cyfip2*$^{flx/flx}$*;Camk2a-Cre* mice (as explained in chapter 4.2.6). Equal volumes of samples from nucleic (200 x *g*), cytosolic (10,000 x *g*) and ultraspin (100,000 x *g*) fractions were run on an SDS-PAGE and actin levels in these fractions were analyzed by western blotting (Figure 15).

Figure 15A shows the western blot results of the experiment from four animals per genotype. In general, the cellular distribution of actin was comparable between the animals. Quantification of these blots (Figure 15B) revealed no changes in the F/G-

actin ratios in the nucleic and cytosolic fractions, which contain the bigger filaments of actin. However, in the ultraspin fraction, where the smallest and most dynamic actin filaments are precipitated, a significant increase of F-actin was observed in the *Cyfip2* conditional knockout mice. These results show that loss of CyFIP2 and the decrease of specific WRC protein levels do not lead to alterations in stable actin dynamics. Rather, the increase in smaller actin filaments might indicate a change in the actin turnover mechanisms.

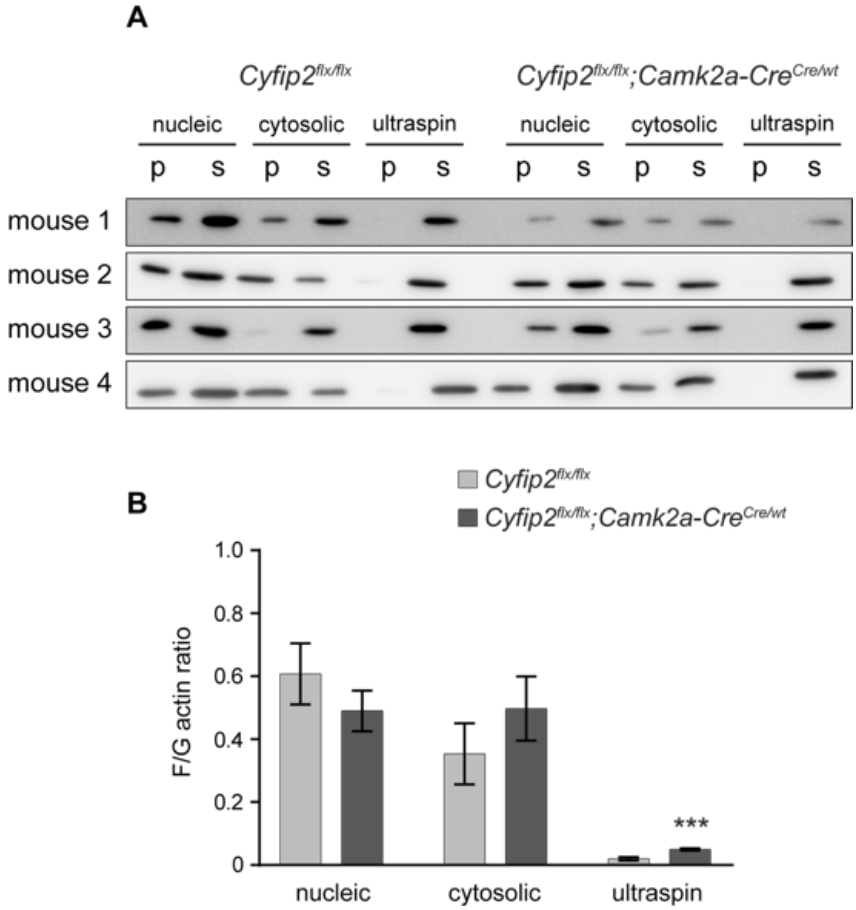

Figure 15. CyFIP2 loss leads to increase in smaller actin filaments with no significant difference in larger filaments.
(A) Western blots showing the level of the actin protein in nucleic, cytosolic and ultraspin fractions prepared from the brains of *Cyfip2*$^{flx/flx}$ and *Cyfip2*$^{flx/flx}$*;Camk2a-Cre* mice at age P130. (B) F/G-actin ratios were calculated by dividing the signal of the actin band in the pellet fraction by the respective supernatant fraction. F/G-actin ratios in nucleic (p=0.353) and cytosolic (p=0.354) fractions show no significant difference in actin levels between the genotypes. *Cyfip2* conditional knockout mice have increased dynamic actin filaments compared to controls (p=0.008). n=4 animals per genotype. Two-tailed t-test. ***p<0.001. Error bars represent s.e.m.

2.3. Synaptic analysis of *Cyfip2* conditional knockout mice

Due to the perinatal lethality of the *Cyfip2*$^{-/-}$ mice, a conditional knockout mouse was generated in our lab where *Cyfip2* was deleted in all CNS cells that express nestin (*Cyfip2*$^{flx/flx}$*;Nes-Cre*). This conditional knockout mouse phenocopied the full knockout with a perinatal lethality phenotype (Hauck, unpublished). Furthermore, the analysis of the *Cyfip2-lacZ* reporter mouse revealed the expression of CyFIP2 prominently in the brain (see chapter 1.1.5.1). Finally, in a previous chapter (2.1.1) we showed the specific expression of CyFIP in all principal neurons of the brain. These results together led to the hypothesis that CyFIP2 has an essential role in the CNS in excitatory synaptic transmission. In order to investigate the role of CyFIP2 in the synapse, we performed physiological, morphological and biochemical analyses in the hippocampus and cortex of *Cyfip2*$^{flx/flx}$*;Camk2a-Cre* mice.

2.3.1. CyFIP2 loss leads to defects in synaptic transmission

To study synaptic physiology, we used well-established electrophysiological techniques. We measured electrical properties of single CA1 pyramidal neurons by using the patch-clamp method, developed by Neher and Sakmann in 1976, where a tight seal is made between a recording microelectrode and the neuronal membrane. We recorded non-action potential (AP)-related excitatory spontaneous synaptic events (miniature excitatory post-synaptic currents, mEPSCs) with the use of specific blockers. To inhibit APs, Na^{2+} channel blocker tetrodotoxin (TTX) was added in the extracellular solution. In order to specifically record the inputs from *Cyfip2*$^{-/-}$ cells (which are all the glutamatergic pyramidal neurons in the hippocampal CA region in the conditional knockout mouse model used), inhibitory inputs were blocked using the $GABA_A$ receptor blocker picrotoxin (PTX) that was added into the extracellular solution. Finally, QX-314 was added in the intracellular solution filling the microelectrode, to block Na^{2+}/Ca^{2+} exchangers.

300 µm thick coronal brain slices were placed in a chamber containing the extracellular solution with the blockers described. A neuron in the pyramidal cell layer of the hippocampal CA1 region was chosen, according to its morphology, and patched with

a microelectrode. The non-AP related spontaneous responses of the neuron were recorded while the membrane was held at -70 mV (Figure 16). The amplitudes and frequencies of the mEPSCs were analyzed to measure post-synaptic strength and pre-synaptic vesicle release dynamics, respectively (Hsia, Malenka and Nicoll, 1998).

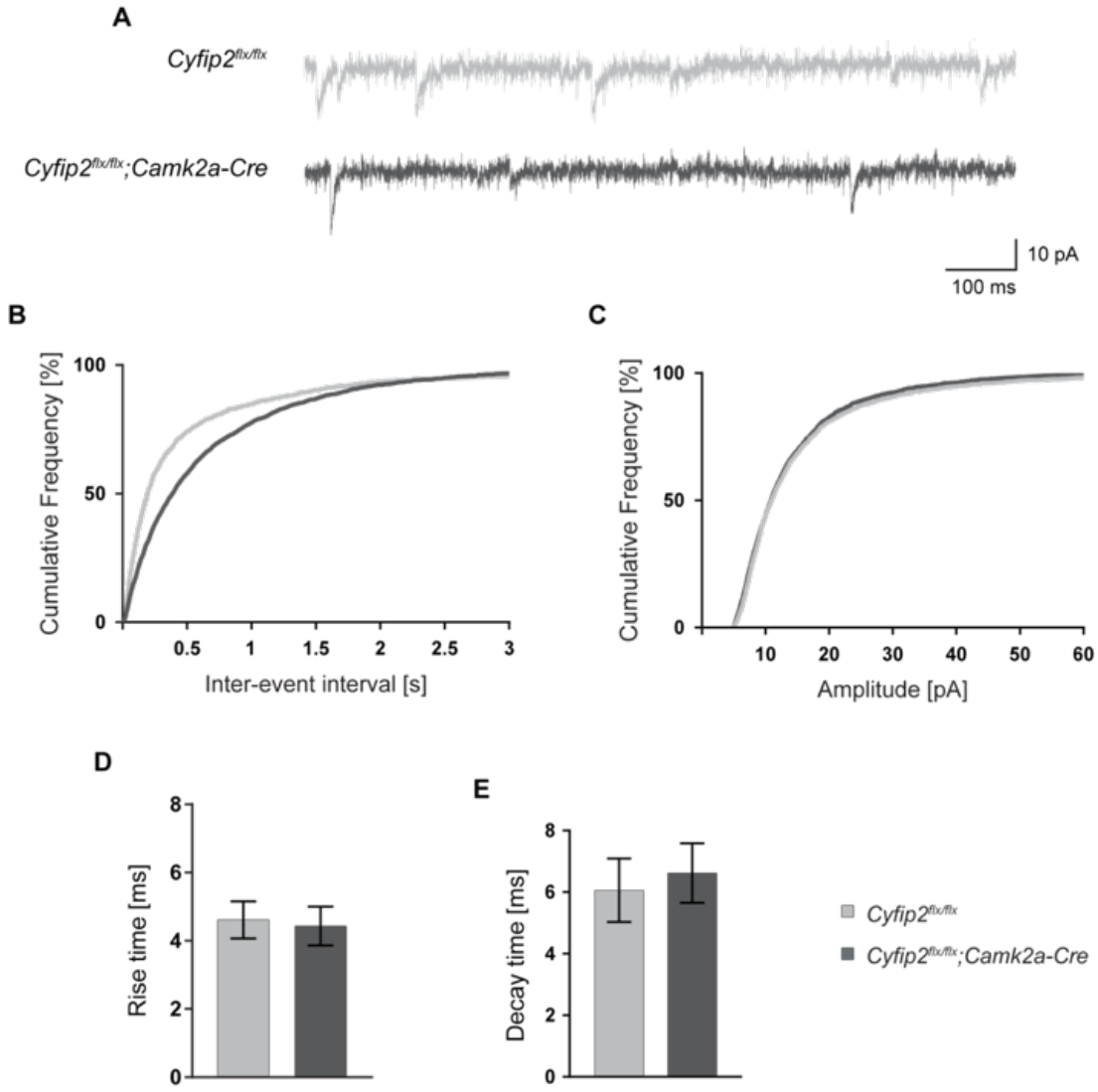

Figure 16. *Cyfip2* conditional knockout mice show reduced excitatory synaptic transmission. (A) Example traces of spontaneous mEPSCs recorded from patched control and knockout CA1 neurons in the presence of TTX and PTX at age P70. (B) CA1 *Cyfip2*$^{-/-}$ neurons show significantly increased inter-event interval (IEI), equivalent to reduced frequency, of spontaneous mEPSC events. The cumulative frequency representation is shown (Kolmogorov-Smirnov test, p=0.011). (C) The amplitudes of mEPSCs are unaltered between the two genotypes. The cumulative frequency representation is shown. (D,E) The kinetics of spontaneous excitatory events are not altered, with unchanged rise (p=0.823) and decay (p=0.702) times of the synaptic currents. Two-tailed t-test. Control cells n=7 cells/4 animals and *Cyfip2*$^{flx/flx}$*;Camk2a-Cre* cells n=9 cells/5 animals. Error bars represent s.e.m.

When the mEPSCs of *Cyfip2* conditional knockout mice were compared to the controls, no difference was observed in the amplitudes of the events (Figure 16C). This indicated that structure and receptor composition of post-synaptic terminals were conserved in the conditional knockout mice at P70. However, we observed that these events were significantly less frequent compared to controls with longer inter-event intervals (IEIs), suggesting reduced pre-synaptic vesicle exocytosis from *Cyfip2*$^{-/-}$ neurons (Figure 16B). To evaluate the kinetics of these events, rise (Figure 16D) and decay (Figure 16E) times of mEPSCs were analyzed. Both rise and decay times were unchanged, pointing to conserved membrane properties (input resistance, capacitance) and AMPA receptor distribution in the post-synapse. Overall, the mEPSC recordings pointed to defects in pre-synaptic vesicle release with no changes in post-synaptic composition in the hippocampus.

2.3.2. *Cyfip2* conditional knockout mice have decreased pre-synaptic vesicle exocytosis

Following the observation of decreased pre-synaptic function in mEPSC recordings in single neurons, we checked whether the non-AP related pre-synaptic defects also translated to a general synaptic transmission deficit in the hippocampus. For this reason, we performed field recordings where we recorded the cumulative output of CA1 pyramidal neurons in response to inputs from the CA3 neurons. To study excitatory synaptic transmission, PTX was added into the extracellular solution. A stimulation microelectrode was placed on the Schaffer collaterals (axons of CA3 pyramidal neurons), while a recording electrode was placed in the *stratum radiatum* of the CA1, where the dendrites of pyramidal neurons are located. Schaffer collaterals were stimulated for 0.2 ms with increasing intensities (10, 15, 20, 25 and 30 µA) and field excitatory post-synaptic potentials (fEPSPs) of CA1 pyramidal neurons were recorded (Figure 17B). Both controls and *Cyfip2* conditional knockout mice showed increasing response to the increasing stimulation intensity. However, compared to the controls, the output of CA1 pyramidal neurons in *Cyfip2* conditional knockout mice was significantly decreased, confirming the synaptic defects observed in mEPSC recordings.

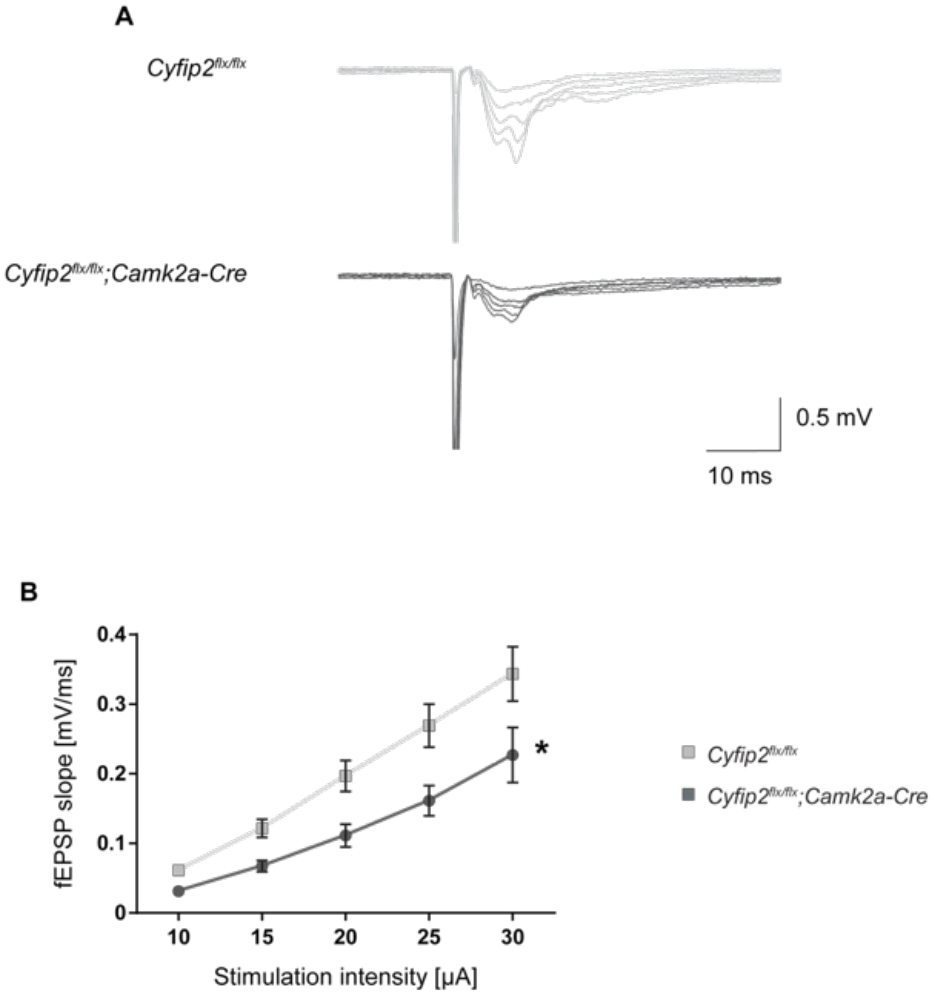

Figure 17. CyFIP2 loss leads to decreased excitatory synaptic transmission in the Schaffer collaterals.
(A) Overlay of example traces of CA1 neurons in response to increasing stimulation of Schaffer collaterals in the presence of PTX. (B) *Cyfip2$^{flx/flx}$;Camk2a-Cre* mice show decreased fEPSP responses to increasing stimulation of CA3 axons, compared to controls (Two-tailed t-test on the slope coefficients of single neurons, p=0.014). Controls n=11 slices/7 animals and *Cyfip2$^{flx/flx}$;Camk2a-Cre* n=11 slices/6 animals. *p<0.05. Error bars represent s.e.m.

In parallel, we performed paired-pulse experiments to confirm the defects in pre-synaptic vesicle release observed by measuring the mEPSCs. In a paired-pulse experiment, two stimuli are presented with a defined time interval and the responses of the neurons are recorded. A facilitation occurs when the response of the neurons to the second stimulus is higher than the response to the first stimulus. This is due to the residual calcium hypothesis, which states that the remaining Ca^{2+} in the pre-synaptic terminals that have not released on the first stimulation will increase the probability of reaching the release threshold following the new Ca^{2+} influx succeeding the second stimulation (Zucker and Regehr, 2002). Therefore, changes in the paired-pulse ratio (PPR) are an indicator of defects in pre-synaptic vesicle exocytosis.

Two adjacent stimuli with 50 ms inter-stimulus interval (ISI) were applied to the Schaffer collaterals, in the presence of PTX (Figure 18B). The PPR was determined as the ratio between the second fEPSP and the first one ($fEPSP_2/fEPSP_1$). *Cyfip2* conditional knockout mice showed an increased PPR compared to the controls, suggesting decreased probability of vesicle exocytosis. As all the patch-clamp and field recordings were performed by blocking inhibitory inputs, only the responses of glutamatergic (thus, *Cyfip2*$^{-/-}$ neurons) were recorded. Hence, decreased mEPSCs frequencies, and increased PPR point to defects in pre-synaptic vesicle exocytosis in neurons lacking CyFIP2, with no measurable post-synaptic changes at P70.

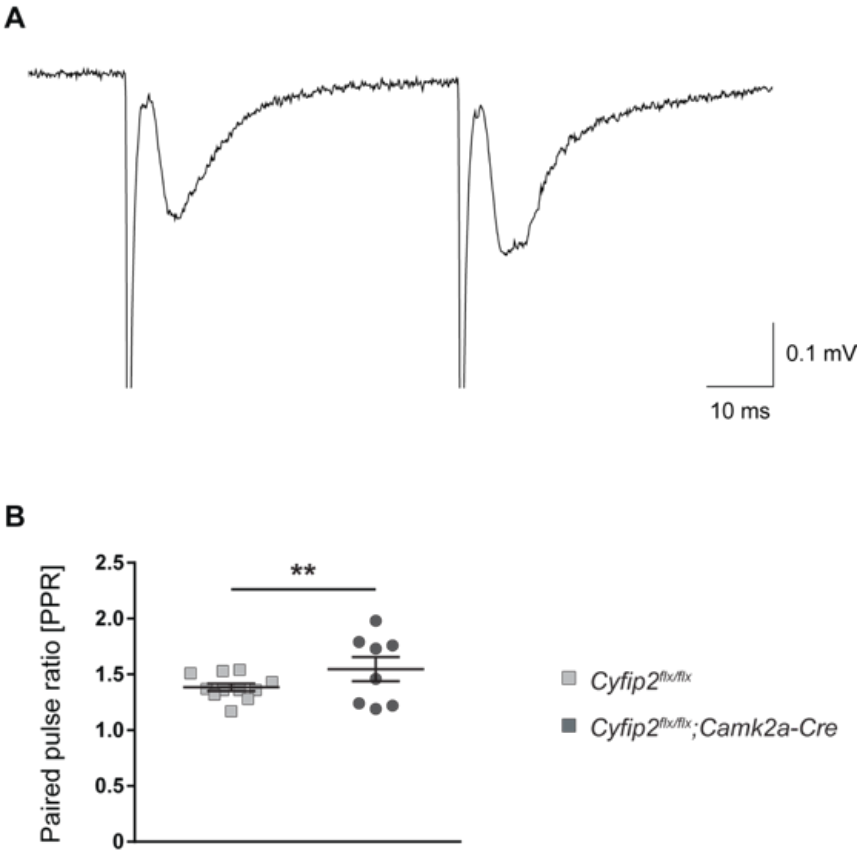

Figure 18. CyFIP2 loss leads to defects in pre-synaptic release.
(A) Example traces of CA1 neurons in response to paired-pulse stimulations of Schaffer collaterals with 50 ms interval, in the presence of PTX. (B) Increase of the paired-pulse ratio ($fEPSP_2/fEPSP_1$) measured by responses to two adjacent stimuli indicates decreased probability of pre-synaptic vesicle exocytosis from the CA3 axons to the CA1 dendrites of *Cyfip2* conditional knockout mice at P70 (Two-tailed t-test, p=0.021). Controls n=11 slices/5 animals and *Cyfip2*$^{flx/flx}$*;Camk2a-Cre* n=8 slices/3 animals. **p<0.01. Error bars represent s.e.m.

2.3.3. Loss of CyFIP2 leads to pre-synaptic terminal shrinkage in the hippocampus

The electrophysiological recordings in *Cyfip2* conditional knockout mice showed defects in pre-synaptic vesicle exocytosis in neurons lacking CyFIP2. However, electrophysiology alone is not sufficient to determine whether these defects are a result of mechanistic alterations in the vesicle cycle or of morphological changes of synapses, and what these changes may be. In order to examine the ultrastructural morphology of synapses in *Cyfip2*$^{flx/flx}$*;Camk2a-Cre* mice, we used electron microscopy (EM). Classical transmission EM is a technique that uses electrons as a very high energy radiation to increase the resolution of the image far beyond what can be obtained with the visible or UV range. Since the wavelength of an electron is 0.0009-0.027 nm, the resolution of the images taken with an EM is at least ~1000-fold higher than light microscope (Gordon, 2014). This allows the visualization of nanoscale structures, such as synaptic vesicles (~40 nm in diameter) and PSDs (25-50 nm in thickness).

CA1 and CA3 synapses (Figure 19A) of control and *Cyfip2* conditional knockout mice at P130 were imaged in coronal brain slices. In Schaffer collateral CA3-CA1 synapses, average pre-synaptic bouton area (Figure 19B,C) and vesicle density (Figure 19B,D) were significantly decreased compared to controls. This was even more pronounced in the mossy fibers DG-CA3 synapses, where the average bouton area was decreased by 80 % in *Cyfip2* conditional knockout mice (Figure 19F,G) and the average vesicle density of these synapses was half of the controls (Figure 19F,H).

Figure 19. Loss of CyFIP2 leads to pre-synaptic shrinkage in CA1 neurons.
(A) Schematic representation of the localization and structure of a mossy fiber bouton (MFB) filled with synaptic vesicles; gcl – granule cell layer, pcl – pyramidal cell layer; DG – dentate gyrus; sl – stratum lucidum; *Cornu ammonis* (CA) areas 1 and 3 are indicated; D – dendrite; s – spine; m – mitochondrion; asterisks indicate synaptic contacts. Ultrastructure of sample cross-sectioned (B) Schaffer collateral boutons and (F) MFBs in *Cyfip2*$^{flx/flx}$ and *Cyfip2*$^{flx/flx}$*;Camk2a-Cre* mice; asterisks indicate boutons with strongly reduced synaptic vesicle density; scale bar: 1 µm. *Cyfip2*$^{flx/flx}$*;Camk2a-Cre* mice show decreased Schaffer collateral (C) bouton area and (D) vesicle density, (E) with no changes in the post-synaptic density (PSD) length (p=0.636). MFB (G) area and (H) vesicle density are significantly reduced, whereas (I) PSD average length is increased by ~15 % in *Cyfip2* conditional knockout mice at age P130 (p=0.001). n=4 animals per genotype. Two-tailed t-test; ***p<0.001. Error bars represent s.e.m.

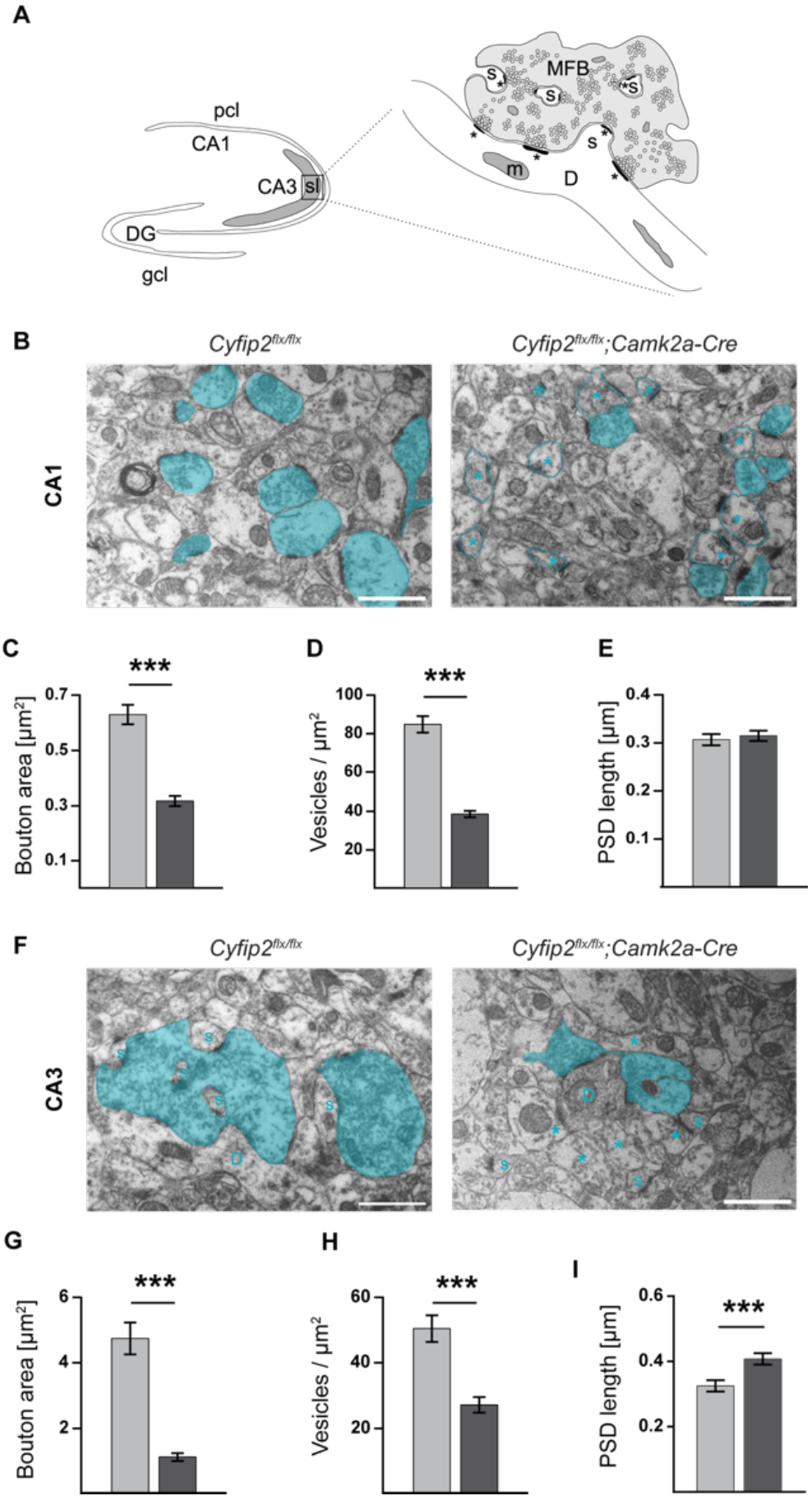
A
pcl
CA1
CA3
sl
DG
gcl
MFB
s
m
D
B
Cyfip2flx/flx
Cyfip2flx/flx;Camk2a-Cre
CA1
C
***
Bouton area [µm²]
0.7
0.5
0.3
0.1
D
***
Vesicles / µm²
100
80
60
40
20
E
PSD length [µm]
0.4
0.3
0.2
0.1
F
Cyfip2flx/flx
Cyfip2flx/flx;Camk2a-Cre
CA3
G
***
Bouton area [µm²]
6
4
2
H
***
Vesicles / µm²
60
40
20
I
***
PSD length [µm]
0.6
0.4
0.2

The PSD length of CA3-CA1 synapses was unaltered, while it was increased by ~15 % in the DG-CA3 synapses. Overall, these observations supported and explained the electrophysiological recordings, showing significant defects in pre-synaptic morphology of *Cyfip2* conditional knockout mice that would account for a reduction of the probability of vesicle exocytosis.

2.3.4. CyFIP2 loss leads to altered levels of certain pre-synaptic proteins upon aging

The decreased pre-synaptic terminal size and vesicle density of hippocampal neurons might be reflected in changes in the levels of pre-synaptic proteins involved in these structures or in their regulation.

In order to analyze changes in the levels of the proteins involved in pre-synaptic vesicle exocytosis, western blotting was performed on total hippocampal lysates from P130 mice, at the age of the EM analysis. The levels of SNARE complex proteins VAMP2, syntaxin 1 (STX1) and SNAP25 as well as of other regulators of exocytosis, such as synaptotagmin 1 (SYT1), synaptophysin (SYP), MUNC18, synapsins (SYN1, SYN2A) and dynamin 1 (DNM1), were analyzed.

In the *Cyfip2* conditional knockout mice, of all analyzed pre-synaptic proteins, only the levels of DNM1 were decreased, whereas MUNC18 levels were slightly increased (Figure 20A). However, when we analyzed the same proteins in the total hippocampal lysates from mice at P330 (Figure 20B), we observed a significant increase in the levels of VAMP2, SNAP25, MUNC18 and SYN1, with a decrease only in STX1 levels. Despite the significant morphological defects observed in EM at P130, the levels of pre-synaptic proteins involved in the vesicle cycle were in general conserved. However, during aging, the levels of several of these pre-synaptic proteins (such as VAMP2, SNAP25, MUNC18, SYN1) were increased, possibly due to a compensatory mechanism to balance the defects in pre-synaptic vesicle exocytosis.

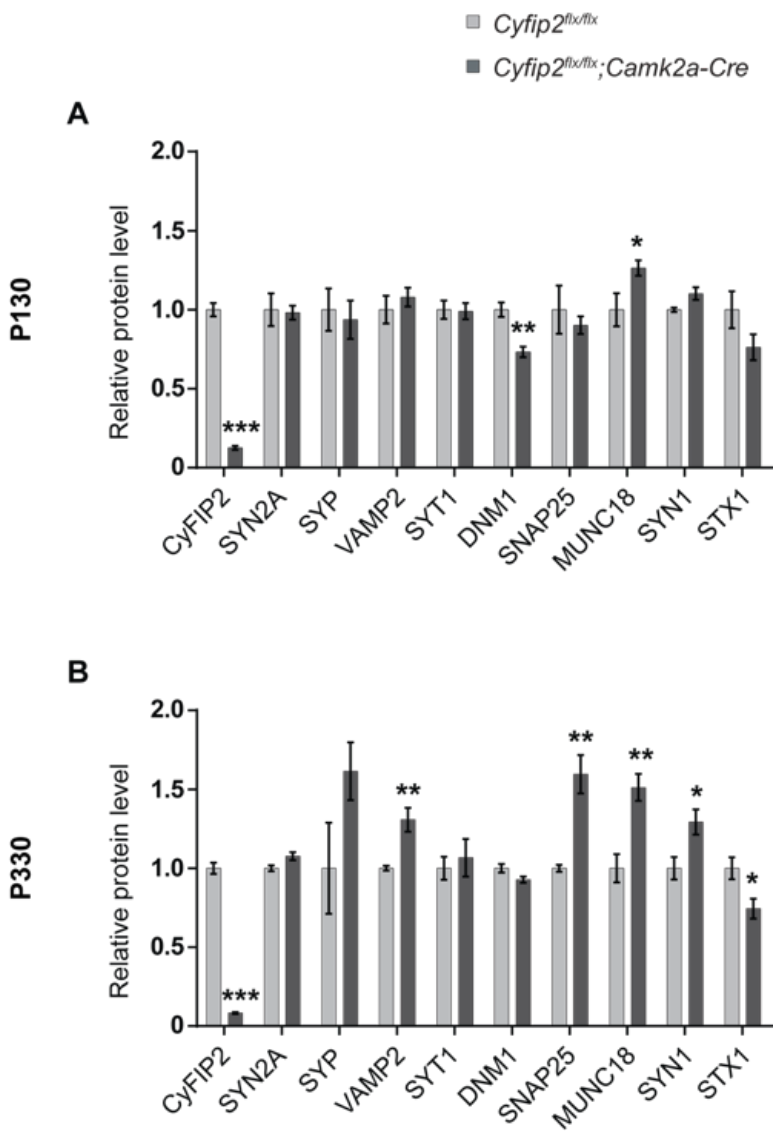

Figure 20. The loss of CyFIP2 leads to increase in certain pre-synaptic protein levels over time.
The effects of synaptic shrinkage on pre-synaptic protein levels (A) are not yet observable at age P130, where the protein levels were mostly unaltered except for a decrease in DNM1 (p=0.002) and an increase in MUNC18 (p=0.044). As the mouse aged, (B) at P330, the levels of certain pre-synaptic proteins such as VAMP2 (p=0.009), SNAP25 (p=0.004), MUNC18 (p=0.005), SYN1 (p=0.033) were increased, whereas STX1 (p=0.029) levels decreased significantly. Blots used for the quantification are shown in Supp. Figure 2. Coomassie stainings performed on the membranes were used as calibration control. n=4 animals for controls and n=5 animals for *Cyfip2*$^{flx/flx}$*;Camk2a-Cre* mice. Two-tailed t-test; *p<0.05, **p<0.01, ***p<0.001. Error bars represent s.e.m.

2.4. Evaluation of an Alzheimer's-like phenotype in *Cyfip2* conditional knockout mice

An anatomical hallmark of AD in patients is the loss of synapses. The synapses of cultured neurons or hippocampal slices of rats exposed to oligomeric Aβ shrink or collapse (Koffie, Hyman and Spires-Jones, 2011). Furthermore, AD mouse models

show synapse loss, which can be reversed with using anti-Aβ_{42} antibodies (Spires-Jones *et al.*, 2009). Pre-synaptic shrinkage and changes in the levels of pre-synaptic proteins during aging in *Cyfip2* conditional knockout mice, together with previous studies claiming an Alzheimer's-like phenotype in *Cyfip2*$^{+/-}$ mice (see chapter 1.1.5.2), pointed to the possibility that complete loss of CyFIP2 could produce an Alzheimer's-like phenotype in the mouse. In order to test this hypothesis, we checked levels of proteins involved in the development of AD as well as neuronal markers to investigate neuronal loss.

2.4.1. *Cyfip2* conditional knockout mice show some molecular signatures of Alzheimer's disease

As previously explained in chapter 1.3.1, the molecular hallmarks of AD are the (1) deposition of extracellular Aβ_{42} plaques upon processing of APP by the BACE1 enzyme and (2) the aggregation of hyperphosphorylated TAU proteins, forming intracellular fibrillary tangles in neurons. In the 2016 study by Tiwari *et al.*, levels of APP, CAMK2A, p-TAU-pS214 (TAU phosphorylated at Serine 214) and BACE1 were shown to be increased in hippocampal synaptosomal extracts of *Cyfip2*$^{+/-}$ mice. Following a similar approach, we measured the levels of the same markers in cortical and hippocampal synaptosomal lysates from control and *Cyfip2*$^{flx/flx}$*;Camk2a-Cre* mice at ~14 months of age (an age when in most mouse models AD phenotypes start to appear) using western blotting (Figure 21).

Cortical synaptosomes of *Cyfip2* conditional knockout mice showed conserved APP and BACE1 levels. In hippocampal synaptosomes, normalized protein levels of BACE1 were conserved, whereas APP levels were increased in *Cyfip2* conditional knockout mice. This result was partially in line with the study by Tiwari et al., also showing increased APP levels in hippocampal lysates.

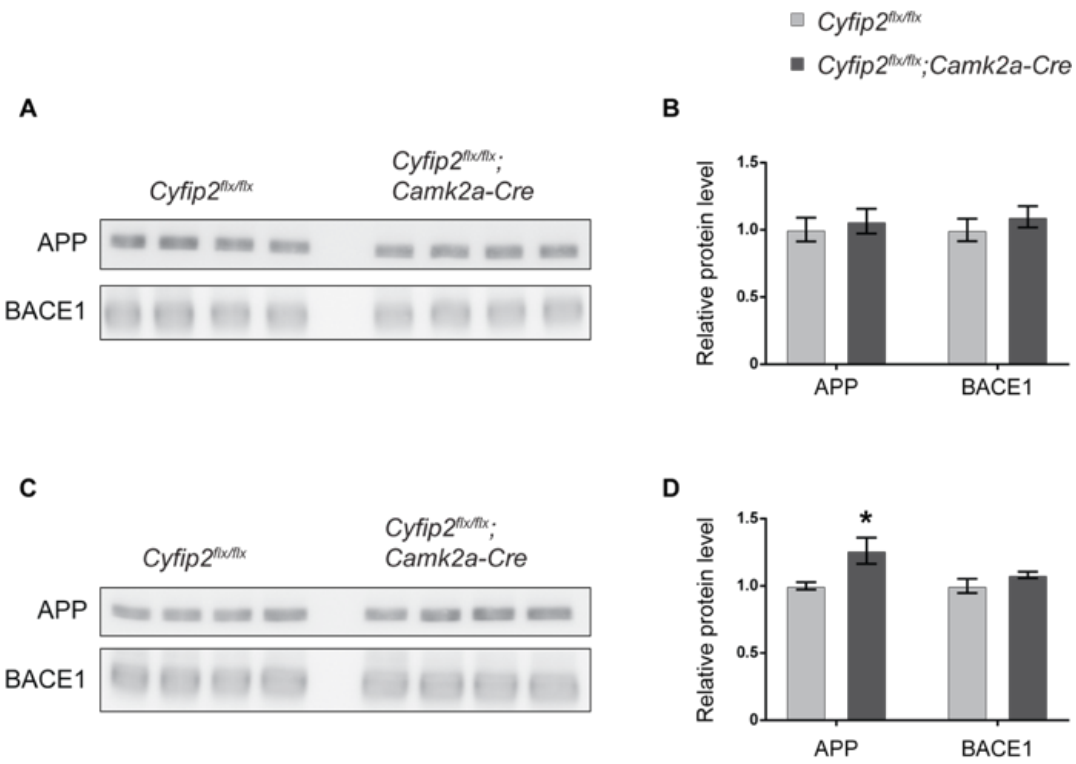

Figure 21. CyFIP2 loss leads to increased APP levels in hippocampal synapses.
Western blots showing the levels of different Alzheimer's markers in (A) cortical and (C) hippocampal synaptosomes of ~14-month-old control and *Cyfip2* conditional knockout mice. (B) Quantification of blots (shown in A) shows no difference in the expression of APP (p=0.628) and BACE1 (p=0.425) in the cortical synaptosomes. **(**D) Quantification of blots (shown in C) shows increased APP expression (p=0.038) and unaltered BACE1 expression (p=0.214) in the hippocampal synaptosomes of *Cyfip2$^{flx/flx}$;Camk2a-Cre* mice. Coomassie stainings performed on the membrane were used as calibration control. n=4 animals per genotypes. Two-tailed t-test; *p<0.05. Error bars represent s.e.m.

In addition to the loss of synapses, a characteristic of AD is the loss of neurons in the hippocampus. The debris produced by disintegrating synapses and neurons then typically lead to the activation of microglia and astrocytes, which secrete inflammatory cytokines such as IL-1, IL-6 and TNF-α that induce astrogliosis and microglia proliferation. These pro-inflammatory molecules may also lead to demyelination of axons and further neuron apoptosis (Fakhoury, 2017).

To analyze neuronal loss and changes in the levels of glial cells, western blotting was performed on total hippocampal lysates from control and *Cyfip2$^{flx/flx}$;Camk2a-Cre* mice at P330. Specific markers were used to quantify the cell types: NEUN for neurons, GFAP for astrocytes, IBA1 for microglia and MBP for oligodendrocytes (Figure 22).

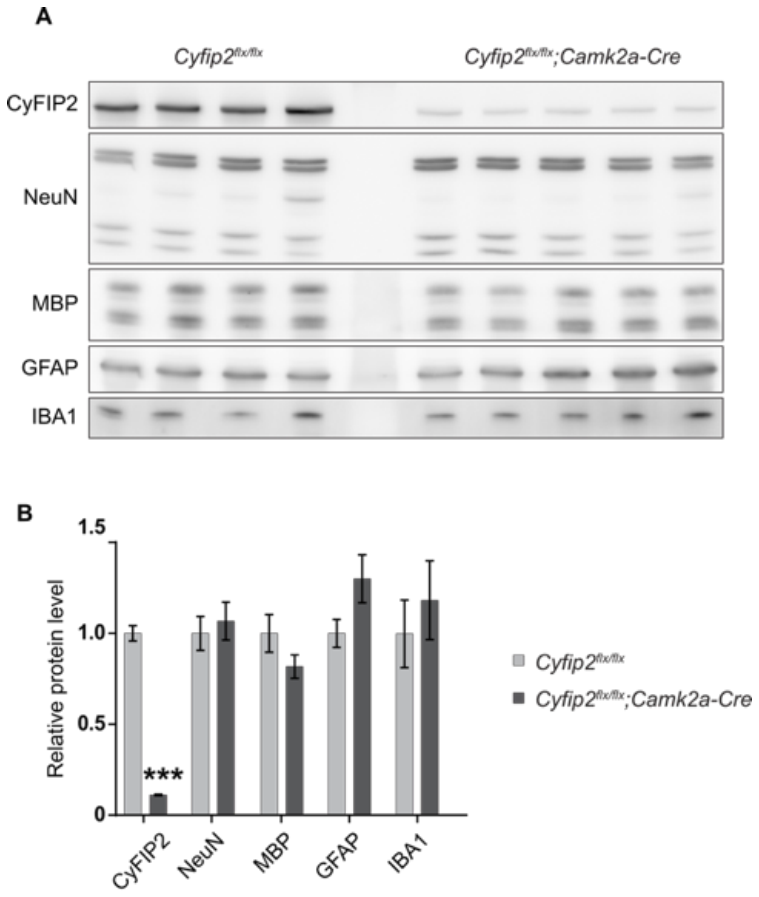

Figure 22. CyFIP2 loss in the hippocampus does not lead to astrogliosis nor neuronal death. (A) Western blots showing levels of neuronal (NEUN), oligodendrocyte (MBP), astrocyte (GFAP) and microglia (IBA1) markers in hippocampi of P330 mice. (B) *Cyfip2* conditional knockout mice do not show neuronal loss, observed by unchanged NEUN levels (p=0.648). Although not significant, a tendential decrease of myelinating oligodendrocytes (MBP, p=0.161) and a tendential increase of astrocytes (GFAP, p=0.109), but no change in microglia (IBA1, p=0.554) was observed upon CyFIP2 loss. Coomassie stainings performed on the membranes were used as calibration control. n=4 animals for controls and n=5 animals for *Cyfip2$^{flx/flx}$;Camk2a-Cre* mice. Two-tailed t-test; ***p<0.001. Error bars represent s.e.m.

The normalized levels of the marker neuronal nuclei (NEUN) were conserved in the *Cyfip2* conditional knockout mice, suggesting no neuronal loss in the hippocampus. In the hippocampus, the levels of the oligodendrocyte marker MBP were tendentially decreased while the astrocyte marker GFAP showed a tendential increase (without significance) upon loss of CyFIP2. This might be interpreted as a mild astrogliosis but inflammatory reaction appeared to be absent. In conclusion, according to the biochemical analysis, the loss of CyFIP2 does not seem to lead to an obvious Alzheimer's-like phenotype, with only a slight increase in APP levels in hippocampal synaptosomes, which are not exclusive to AD.

2.4.2. CyFIP2 is involved in mRNA translation regulation

Previous work on CyFIP1 showed an interaction of the protein with eIF4E, thus suggesting a role for CyFIP1 in mRNA translation. Since CyFIP2 had an identical eIF4E-binding motif, a similar role of CyFIP2 in mRNA translation regulation was proposed (see chapter 1.1.4). It is known that FMRP regulates the translation of APP by binding to the coding region of the *App* mRNA. Therefore, it is plausible to suggest that CyFIP2, a protein that is proposed to dually bind FMRP and eIF4E, might have a possible role in the regulation of *App* mRNA.

To confirm whether CyFIP2 interacts with eIF4E, we performed a pull-down using m^7GTP-Sepharose beads that mimic the 5' cap of an mRNA (see chapter 4.2.8) (Figure 23). As expected, eIF4E was successfully bound to the m^7GTP-Sepharose beads. In addition, both CyFIP1 and CyFIP2 were detected in the bound fraction, interacting with the cap binding complex. However, repeated washes of the beads led to the dissociation of both CyFIPs, suggesting a weak and transient interaction with the cap binding complex. Surprisingly, FMRP was missing from the bound fraction, possibly due to the experimental conditions and procedure. These results demonstrated, for the first time, an involvement of CyFIP2 in mRNA translation regulation.

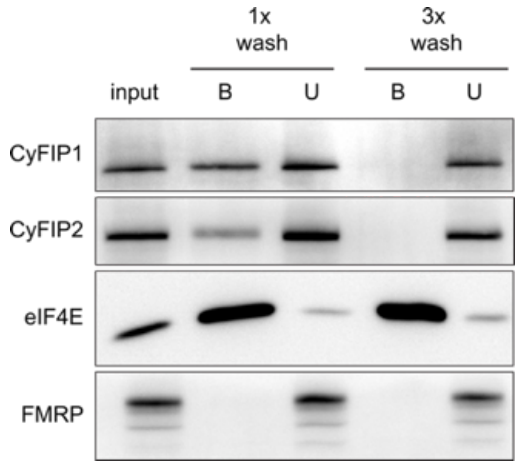

Figure 23. CyFIP2 is possibly involved in mRNA translation.
Western blot showing the results of a sample pull-down experiment performed on a wt mouse brain extract at age P70 using m^7GTP coated Sepharose beads; I – input, B – bound fraction, U – unbound fraction. eIF4E is enriched in the bound fraction, and both CyFIPs are present when the beads are washed one time. Increased number of washes lead to the dissociation of the CyFIPs, suggesting a transient binding between CyFIPs and the eIF4E.

2.5. Morphological analysis of *Cyfip2* conditional knockout mice reveals a phenotype similar to Fragile-X Syndrome

The pre-synaptic shrinkage in hippocampal neurons in *Cyfip2* conditional knockout mice and the increase of certain pre-synaptic proteins with aging led to the question of whether CyFIP2 loss also affects the post-synapse. In order to address this question, we performed Golgi staining, which is a random and sparse staining of neurons in the brain by the crystallization of silver chromate. This method allowed us to identify and analyze dendritic spines distinctively, while providing an overview of the brain morphology.

14-month-old mouse brains were dissected and stained using Golgi's method (see chapter 4.3.2). Dendrites of cortical layer V pyramidal neurons as well as hippocampal CA1 pyramidal neurons were imaged with a brightfield microscope. The gross morphology of the *Cyfip2* conditional knockout mice brains was comparable to control mice, with no obvious changes in cell layering or morphological abnormalities (Supp. Figure 10).

2.5.1. *Cyfip2* conditional knockout mice have increased number of spines

In order to investigate whether CyFIP2 has a role in the maintenance of dendritic spines in the hippocampus, we counted the number of spines in the proximal regions of CA1 dendrites (up to 100 µm from the soma) and calculated the spine density (Figure 24). Apical dendrites (dendrites extending into the *stratum radiatum*) of *Cyfip2* conditional knockout mice had higher density of spines compared to the control mice in both the primary branches (Figure 24B) and secondary branches (Figure 24C). In the basal dendrites (extending towards *stratum oriens*) the spine density levels were unchanged in the primary branches (Figure 24D), but increased in the secondary branches (Figure 24E). This increase in the total number of spines could be a mechanism of the brain to compensate for the reduced input from the pre-synaptic site (see chapter 2.3).

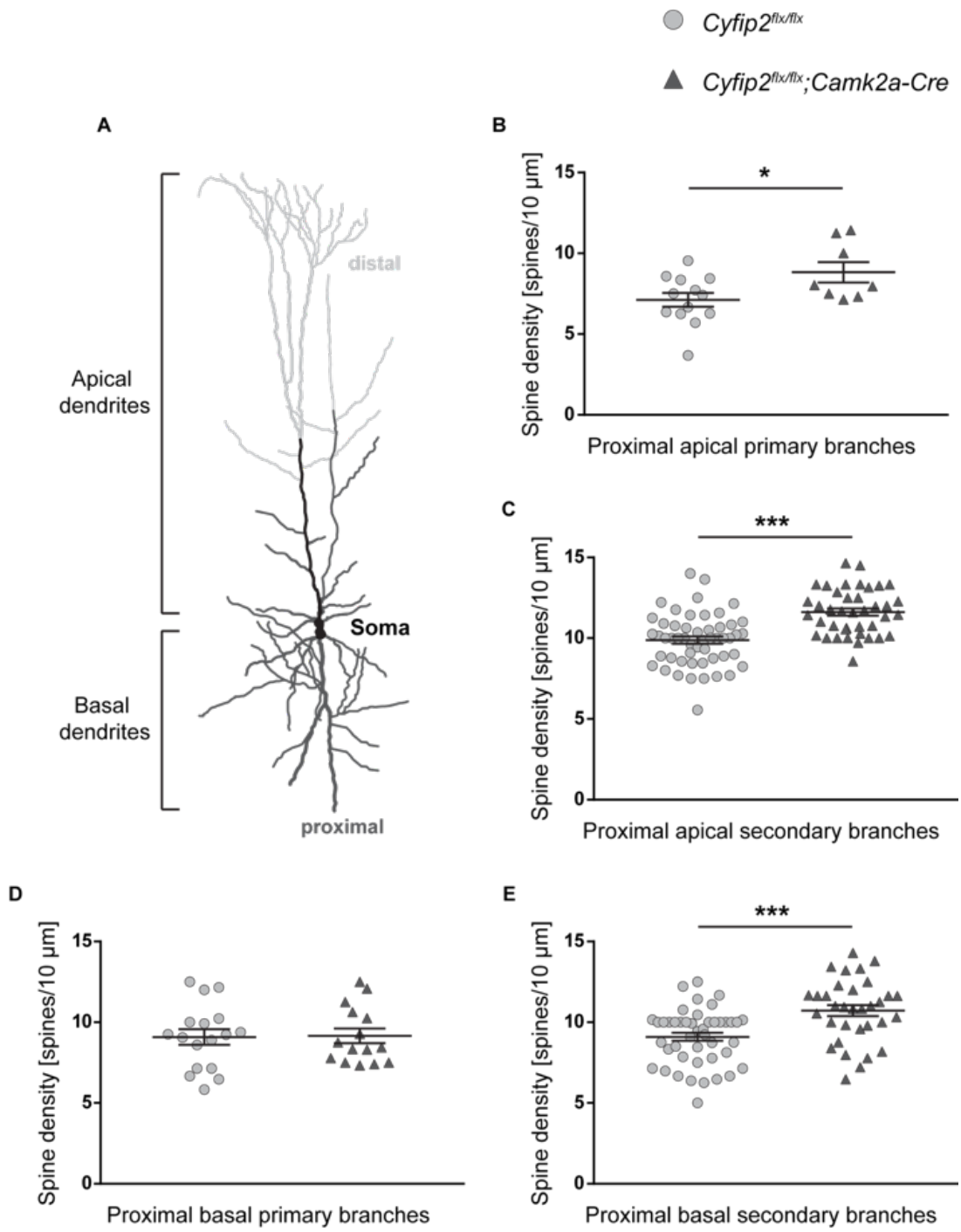

Figure 24. Spine density in hippocampal CA1 neurons of 14-month-old mice is increased upon CyFIP2 loss.
(A) Scheme of a pyramidal neuron, showing the basal and apical dendrites. In the proximal region of the dendrites of pyramidal CA1 neurons spine density is increased in apical (B) primary ($p=0.03$) and (C) secondary ($p=0.6\times10^{-6}$) as well as in basal (E) secondary ($p=0.19\times10^{-3}$) branches, with no difference in (D) primary ($p=0.92$) branches at 14 months of age. n=2 animals per genotype. In all graphs, each data point represents one neuron. Two-tailed t-test; *$p<0.05$, ***$p<0.001$. Error bars represent s.e.m.

2.5.2. CyFIP2 loss leads to decreased mature/immature spine ratios

During the formation of a spine, an F-actin rich filopodia-like protrusion extends from the dendrite. Upon input from the pre-synaptic site, the spine matures through the branching of actin filaments with the help of ABPs such as the ARP2/3. Branching of actin filaments helps to form a mushroom-like structure, which leads to AMPA receptor enrichment and greater glutamate-induced currents (Lai and Ip, 2013). Since the branching of actin filaments relies on actin nucleators such as the ARP2/3 complex, which is activated by the WRC, we tested the effect of CyFIP2 loss on spine maturation in *Cyfip2* conditional knockout mice.

Figure 25A shows examples of Golgi stained CA1 pyramidal neurons from control and *Cyfip2*$^{flx/flx}$*;Camk2a-Cre* mice. Spines of proximal dendrites (up to 100 µm from the soma) were distinguished as immature (filopodia, indicated with *) and mature (mushroom, indicated with #). The mature/immature spine ratio was calculated in a given distance. In the apical dendrites (extending towards *stratum radiatum*) of *Cyfip2* conditional knockout mice, the mature/immature spine ratios were significantly reduced compared to the control mice both in primary branches (Figure 25B) and secondary branches (Figure 25C). This phenotype was also observed in the basal dendrites (extending towards *stratum oriens*), where the mature/immature spine ratios were decreased in both primary (Figure 25D) and secondary branches (Figure 25E).

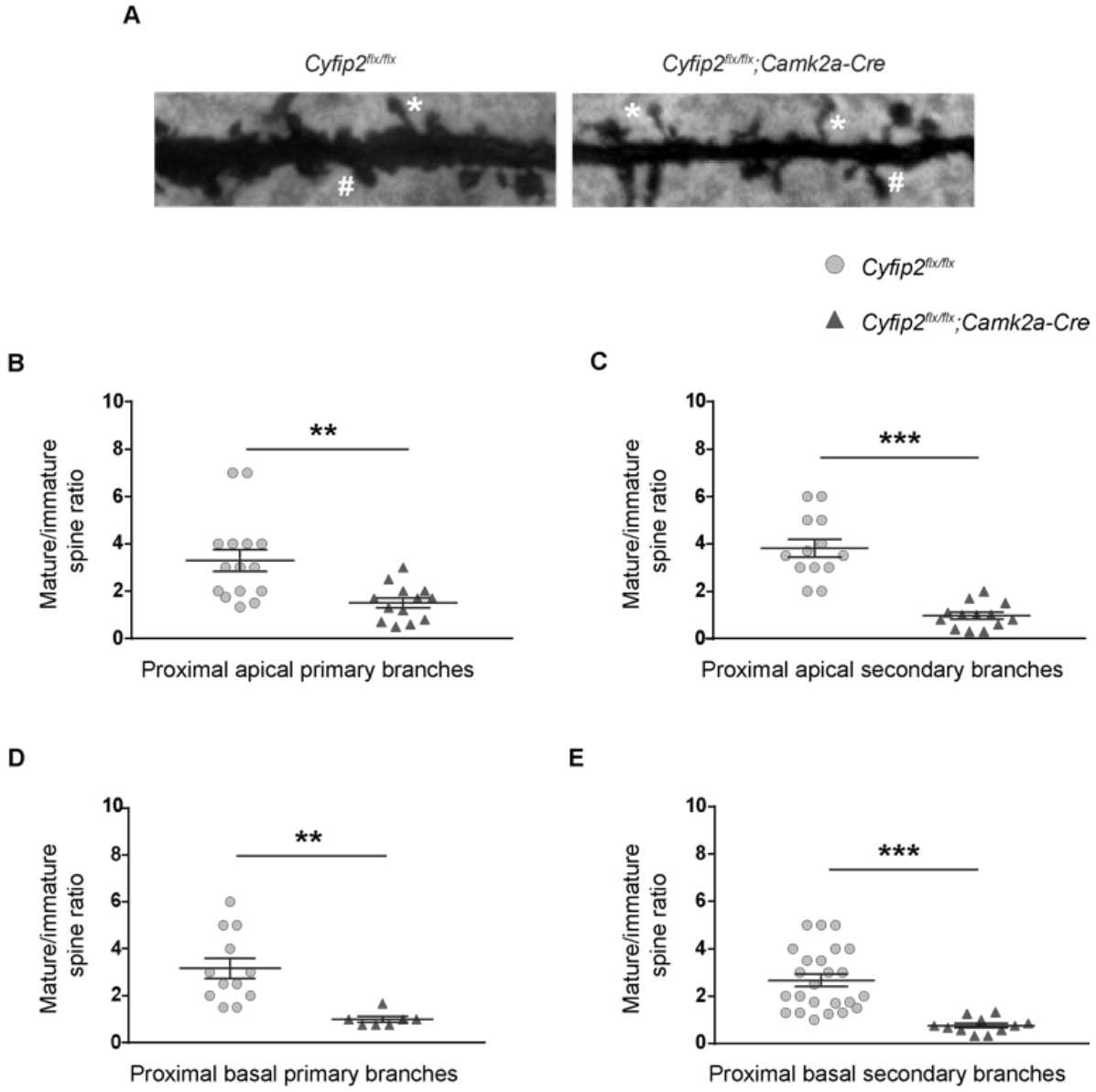

Figure 25. CA1 hippocampal neurons of 14-month-old *Cyfip2* knockout mice have significantly reduced mature/immature spine ratios.
(A) Exemplary Golgi staining images of dendritic branches used to identify spines and sort them into mature (stubby, mushroom – indicated with #) or immature (filopodia – indicated with *). The ratio of mature to immature spines was calculated along the proximal region of the dendrites in pyramidal CA1 neurons and plotted. The mature/immature spine ratios were significantly reduced in both apical (B) primary ($p=0.002$) and (C) secondary ($p=1.9\times10^{-7}$) as well as in basal (D) primary ($p=0.002$) and (E) secondary ($p=3.7\times10^{-5}$) branches compared to the controls. n=2 animals per genotype. In all graphs each data point represents one neuron. Data was normally distributed according to the Shapiro-Wilk test in (C-E). Solid lines represent mean ± s.e.m, two-tailed t-test. Data in (B) was not normally distributed. Solid lines represent median ± interquartile range; Mann-Whitney test. **p≤0.01, ***p≤0.001.

Both the shrinkage of pre-synaptic boutons and the decreased mature/immature spine ratios could be correlated to an upregulation of autophagy in the neurons. Autophagy is a degradation system of cells that removes or recycles organelles, aggregated

proteins and infectious agents upon metabolic stress (Bento *et al.*, 2016). In macroautophagy, double membrane vesicles (called autophagosomes) carry the substrates into the lysosome via actin filaments, where they are degraded through lysosomal hydrolysis (Yu, Chen and Tooze, 2018).

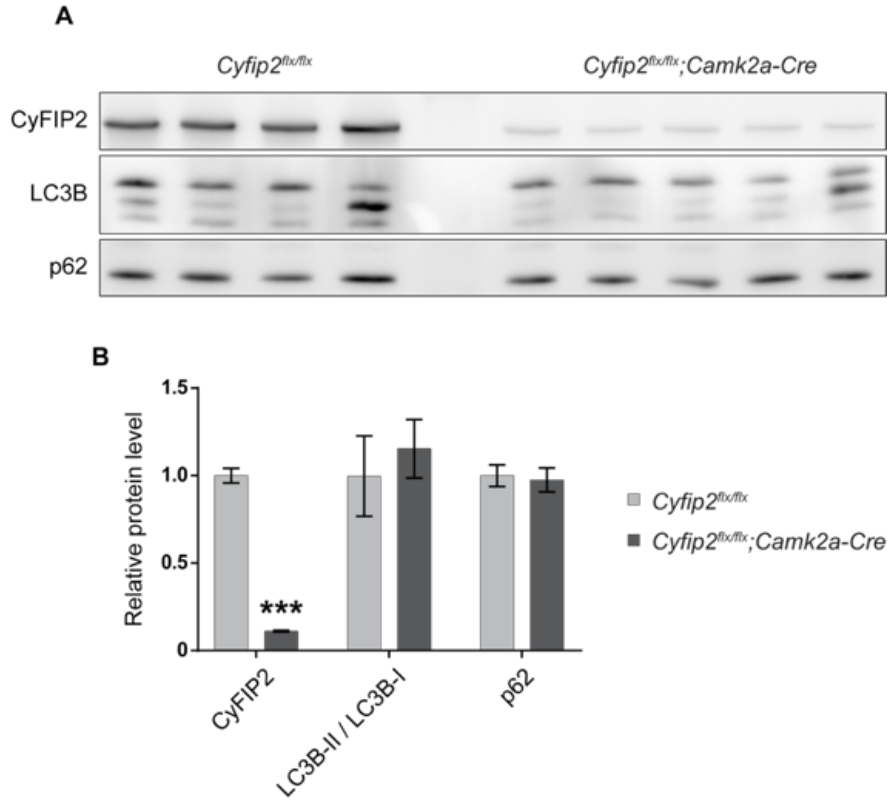

Figure 26. Synaptic loss in hippocampus is not caused by autophagy.
(A) Western blots of hippocampal total lysates from P330 control and *Cyfip2* conditional knockout mice, probed with anti-LC3B and anti-p62 antibodies. (B) The protein levels of autophagy marker p62 (p=0.789) and LC3B-II/LC3B-I ratios (p=0.599) were unaltered in *Cyfip2*$^{flx/flx}$*;Camk2a-Cre* mice, showing no increase or decrease in autophagy. Coomassie stainings performed on the membrane were used as calibration control. n=4 animals for controls and n=5 animals for *Cyfip2*$^{flx/flx}$*;Camk2a-Cre* mice. Two-tailed t-test; ***p<0.001. Error bars represent s.e.m.

To examine whether the morphological defects in synapses of *Cyfip2* conditional knockout mice are due to autophagy, markers of autophagy were quantified by western blotting. The microtubule-associated protein light chain 3B (LC3B) is a protein ubiquitously expressed in the cytoplasm of mammalian tissues. The cytoplasmic form of LC3B (LC3B-I) during the process of autophagy is conjugated to phosphatidylethanolamine leading to the formation of the LC3B-II, which is recruited to the autophagosomal membrane (Tanida, Ueno and Kominami, 2008). The LC3B-II/LCB-I ratio is used as a marker of autophagy, where an increase represents higher

levels of autophagosome incorporated LC3B, thus an increase of autophagy in the cell. Another marker for autophagy is the sequestosome 1 (SQSTM1, also named p62), which non-covalently interacts with ubiquitin or polyubiquitin chains. Thereon, it delivers the cargo to the autophagosome through its LC3 interacting domain (Liu *et al.*, 2016).

The LC3B-II/LC3B-I ratio and the level of p62 were both unchanged in total hippocampal lysates of *Cyfip2* conditional knockout mice, compared to controls (Figure 26). These results suggested that the loss of CyFIP2 does not lead to an increase in autophagy in hippocampal neurons. Therefore, we can conclude that the morphological defects observed in the *Cyfip2*$^{-/-}$ synapses are not due to increased autophagy.

2.6. Behavioral analysis of *Cyfip2* conditional knockout mice

Shrinkage of the pre-synaptic boutons, decreased mature/immature spine ratios and an increase in APP levels in the hippocampus of *Cyfip2* conditional knockout mice all pointed to possible memory disturbances in these mice. In order to test this, we performed open-field, Y-maze and NOR experiments in control and *Cyfip2*$^{flx/flx}$*;Camk2a-Cre* mice at age P330.

2.6.1. *Cyfip2* conditional knockout mice show decreased exploratory behavior

The open-field test is a behavioral assay that is used to study the exploration, locomotion and anxiety-like phenotypes of mice (Carter and Shieh, 2010). The mouse is placed in an open arena and allowed to explore it for a certain time. The movements of the mouse are tracked using a camera and locomotion is measured by the distance the mouse travels. The arena is divided into two virtual zones: center and periphery, and the number of entries into these zones together with the number of rearings is used as a measure of exploration. The time and distance the mouse travels in these

two zones are indicators of anxiety-like behavior. In the test, the mouse is expected to spend more time (or travel more distance) in the periphery of the field, so the time spent (or distance travelled) in the center is inversely correlated to anxiety-like behavior (Crawley and Paylor, 1997). The rearing behavior, during which the mice put their weight on the hind legs, lifting the front ones, is a behavioral phenotype shown by mice placed in a novel environment. It is used as a score to assess exploratory (in the center zone) and escape (in the periphery zone, along the walls of the field) behaviors (van Abeelen, 1970).

In order to investigate these phenotypes upon loss of CyFIP2, an open-field test was performed with P330 control and *Cyfip2* conditional knockout mice. After being transported to the experimental room, the mice were habituated for either 30 minutes or 1 hour before the start of the test. Following this, the mice were allowed to freely explore the novel arena for 10 minutes (Figure 27). Interestingly, we observed differences between the behavior of the mice after different habituation times, except for the total travelled distance (Supp. Figure 14A,B) and average speed (Supp. Figure 14C,D), which were consistently unchanged between the two genotypes. Following 30 minutes of habituation, *Cyfip2* conditional knockout mice entered the two zones significantly less than the controls (Figure 27A). The distance travelled (Figure 27E) and the time spent (Figure 27C) in the center of the open field were significantly less for *Cyfip2*$^{flx/flx}$*;Camk2a-Cre* mice than for the controls after 30 minutes of habituation, whereas the time spent in the periphery was significantly higher for the *Cyfip2* conditional knockout mice (Figure 27C).

Figure 27. *Cyfip2* conditional knockout mice show reduced exploratory behavior and a habituation-sensitive anxiety-like phenotype in the open field test.
A 10-minute open-field test was performed after the mice were habituated to the experimental room either for (A,C,E,G) 30 minutes or (B,D,F,H) 1 hour. Testing area was divided into two virtual zones: center (35 % of the arena) and periphery. *Cyfip2* conditional knockout mice showed (A) decreased locomotion (p=0.004) and anxiety-like phenotype during the test after 30 minutes of habituation, observed by less (C) time (p=0.02) and (E) distance spent (p=0.007) in the center. In the test performed after 1 hour of habituation, (B) the total locomotion of the conditional knockout mice was similar to the controls (p=0.354). The (D) time (center, p=0.943; periphery, p=0.938) and (F) distance spent (center, p=0.239; periphery, p=0.244) in the two virtual zones were comparable between the two genotypes, pointing to no anxiety-like behavior. (G, H) The number of rearings in the center of the area was significantly smaller for *Cyfip2*$^{flx/flx}$*;Camk2a-Cre* mice compared to controls, indicating a reduced exploratory behavior after both (G) 30 minutes and (H) 1 hour habituation. (A,C,E,G) n=8 animals for controls and n=9 animals for *Cyfip2*$^{flx/flx}$*;Camk2a-Cre* mice. (B,D,F,H) n=11 animals per genotype. Two-tailed t-test, *p<0.05. Error bars represent s.e.m.

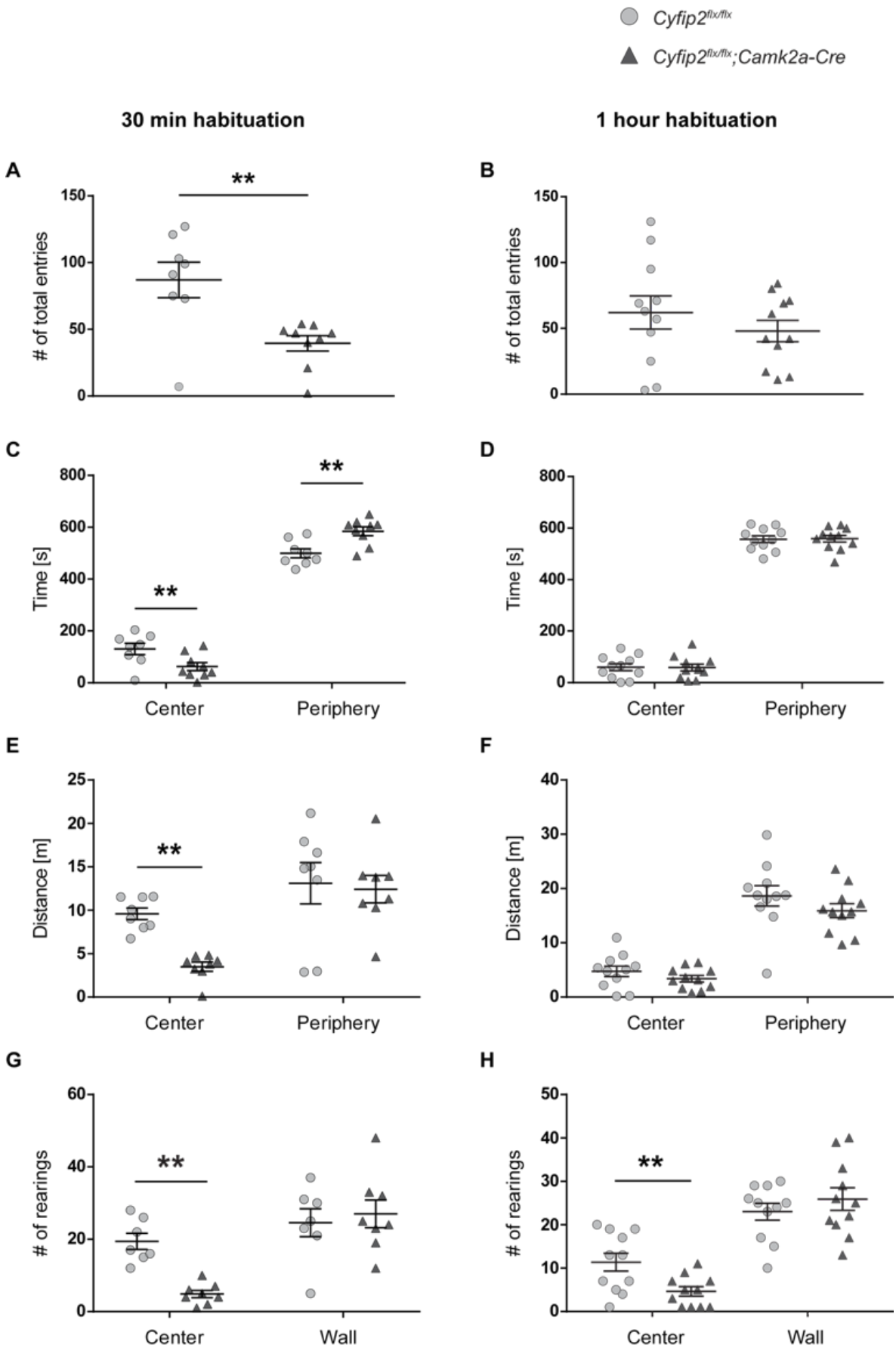
Cyfip2flx/flx
Cyfip2flx/flx;Camk2a-Cre
30 min habituation
1 hour habituation
A
B
C
D
E
F
G
H
# of total entries
Time [s]
Distance [m]
# of rearings
**
Center
Periphery
Wall

These behaviors, pointing to an anxiety-like phenotype in *Cyfip2* conditional knockout mice, were not visible after 1 hour of habituation. The mice showed comparable number of total entries (Figure 27B), as well as similar time spent (Figure 27D) and distance travelled (Figure 27F) in the two zones, which suggested that the anxiety-like behavior is mild and only observed when the mice are under particularly stressful conditions. After both habituation times, *Cyfip2* conditional knockout mice showed less rearing behavior in the center of the open field, whereas the rearings at the periphery were comparable (Figure 27G,H). Overall, CyFIP2 loss led to a mild (habituation-sensitive) anxiety-like phenotype with decreased exploratory behavior.

2.6.2. *Cyfip2* conditional knockout mice have unaltered working memory

The Y-maze is a test used to measure spatial working memory, exploration and autistic-like behavior in mice (Hughes, 2004). In a Y-maze experiment, the mouse is confronted with the exploration of a maze that has 3 corridors that form a Y-shape. The mouse is placed at one end of a corridor and is allowed to explore the maze for 10 minutes. The Y-maze is a suitable test for the assessment of working memory. As the mouse travels through the corridors, it uses spatial cues to remember the last visited arm. The mouse is expected to enter the arms in an alternating sequence, since mice prefer to explore novel environments. A spontaneous alternation occurs when the mouse successfully enters three different arms (*e.g.* X-Y-Z). An alternate-arm return represents a failure of alternation, when mice return to an arm after entering a second arm (*e.g.* X-Y-X). Lastly, a same-arm return is scored when the mouse exits and re-enters the same arm (*e.g.* X-X). Same-arm return is further used as a measure for autistic-like behaviors, as repetitive behaviors are a hallmark of autism (Chang, Cole and Costa, 2017). The latency of mice to exit the first corridor (or arm) in a Y-maze is representative of anxiety-like behavior, whereas total number of entries into the arms is used as a measure of exploration.

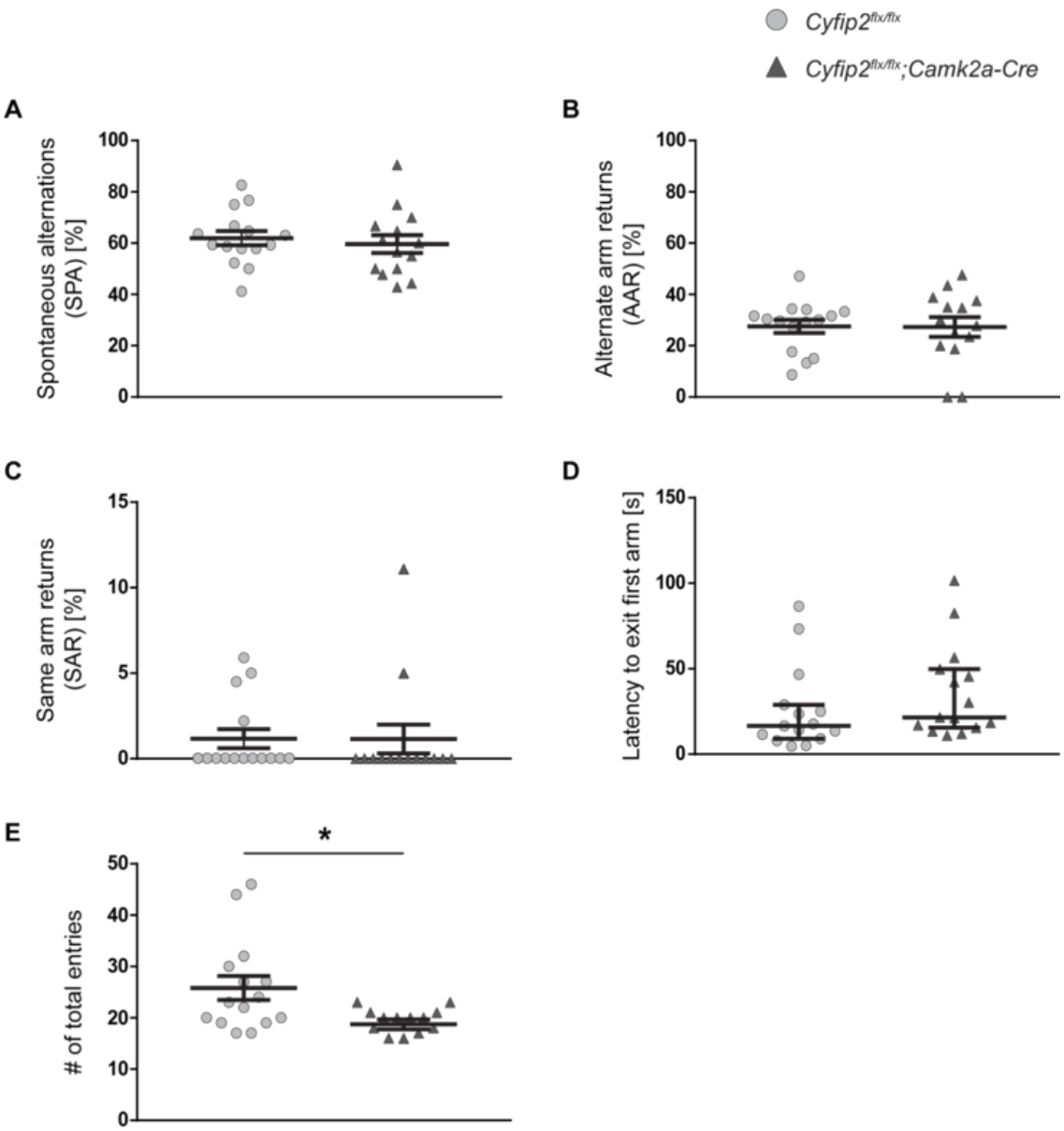

Figure 28. *Cyfip2* conditional knockout mice have unaltered working memory.
Cyfip2$^{flx/flx}$*;Camk2a-Cre* mice at P330 age show conserved working memory in the Y-maze with unaltered (A) spontaneous alternations (p=0.606) and (B) alternate-arm returns (p=0.959). *Cyfip2* conditional knockout mice do not show (C) repetitive behavior, assessed by the unaltered same-arm returns (p=0.982) in the Y-maze. (D) The latency to exit the first arm is only tendentially increased (p=0.287) in *Cyfip2* knockout mice, indicating no overt anxiety-like phenotype. *Cyfip2*$^{flx/flx}$*;Camk2a-Cre* mice display reduced exploratory behavior, indicated by (E) decreased total number of entries (p=0.011) into the arms of the Y-maze. n=15 animals for controls and n=14 animals for *Cyfip2*$^{flx/flx}$*;Camk2a-Cre* mice. Two-tailed t-test; *p<0.05. Error bars represent s.e.m.

To test short-term working memory, a Y-maze experiment was performed with control and *Cyfip2* conditional knockout mice at age P330 (Figure 28). In both genotypes spontaneous alternations, alternate-arm returns and same-arm return sequences were comparable, suggesting no defects of short-term working memory in *Cyfip2*

conditional knockout mice. Latency to exit the first arm was not significantly different, but it was tendentially increased in *Cyfip2*$^{flx/flx}$*;Camk2a-Cre* mice, confirming a not overt anxiety-like behavior. However, *Cyfip2* conditional knockout mice entered less arms in total compared to the controls (Figure 28E), in agreement with the decreased exploratory behavior observed in the open-field test.

2.6.3. CyFIP2 loss does not affect object recognition memory

A common test used to measure short-term memory is the NOR test. The NOR consists of three stages: habituation, familiarization and test. In the habituation phase, the mouse is placed in an open-field arena and allowed to explore the area for 10 minutes. This is performed in order to reduce effects of the novel environment during the objects exploration phases. One day later, the mouse is placed in the same open-field arena that has two identical objects (★) in the periphery. The mouse spends 10 minutes with the objects, free to explore them. 1 hour later, one of the objects is replaced with a novel object (●) that has a different color, shape and texture. The mouse is placed again in the arena and explores the new object configuration for 10 minutes. The time that the mouse spends exploring (smelling, climbing) the novel object and the old object is compared to measure the object recognition memory of mice. As mice have a preference for novelty, they are expected to spend more time exploring the new object (●), and a failure to do so suggests a memory defect.

We performed the NOR test in control and *Cyfip2*$^{flx/flx}$*;Camk2a-Cre* mice at age P330 (Figure 29). In the familiarization phase, mice from both genotypes spent almost equal time interacting with each of the two identical objects. This proved that the mice did not have a preference for either one of the objects or their location. During the test phase, both control and *Cyfip2* conditional knockout mice spent significantly longer time with the novel object compared to the older one. This indicated that mice from both genotypes recognized the novel object. These results collectively showed that the conditional knockout of *Cyfip2* does not lead to short-term memory defects in aged mice.

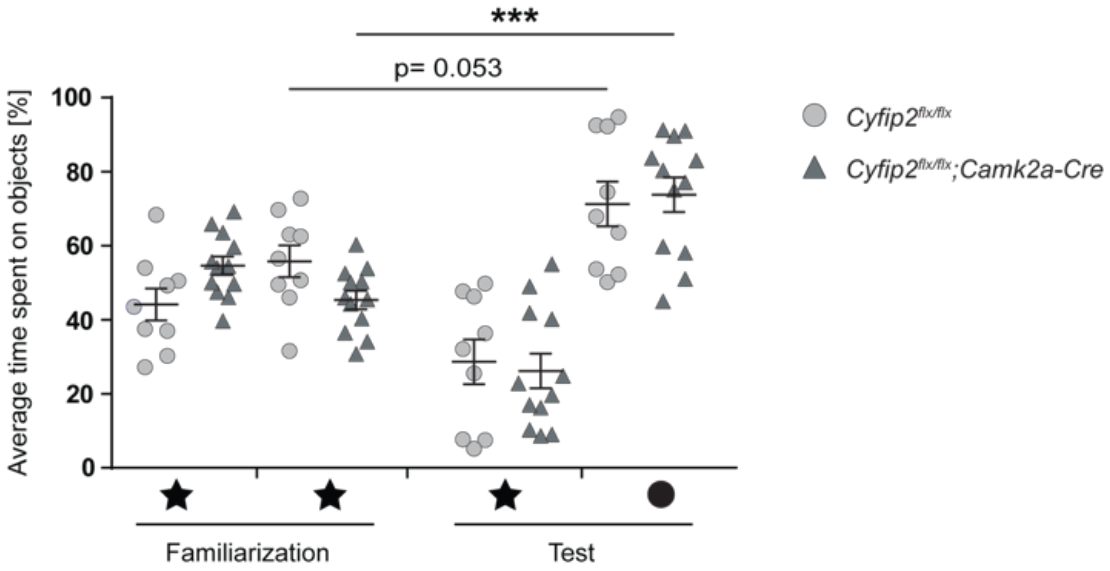

Figure 29. *Cyfip2* conditional knockout mice have conserved object recognition memory. In a novel object recognition test, *Cyfip2* conditional knockout mice were able to recognize the novel object, spending significantly more time interacting with it during the test phase ($p=2.3x10^{-5}$), which was conducted one hour after the familiarization phase. The mice do not show a preference for any of the objects or their location in the familiarization phase, since the time they spend with both objects are similar (~50 %). n=9 animals for controls and n=12 animals for *Cyfip2$^{flx/flx}$;Camk2a-Cre* mice. Two-tailed t-test; ***p<0.001. Error bars represent s.e.m.

3. Discussion

3.1. CyFIP2 is expressed in glutamatergic and cholinergic neurons but not in glia cells

Studies on the role of CyFIP have been mainly focused on the ubiquitously expressed CyFIP1 paralogue. Due to the perinatal lethality of the *Cyfip2*$^{-/-}$ mice, the function of the brain prominent paralogue has only been studied using heterozygous animals. Although its importance in embryonic development is clear from the perinatal lethality phenotype, the role of CyFIP2 in the adult brain has so far been investigated to a limited detail. To study the role of CyFIP2 in the adult mouse, it is important to know in which cell types the protein is expressed. Once the expression pattern of CyFIP2 is known, tissue- or cell-specific knockout mouse models can be generated and analyzed in detail to assess the role of CyFIP2. Previous studies in our lab using a *Cyfip2-LacZ* reporter mouse line showed the expression of CyFIP2 mainly in the CNS, in contrast to its ubiquitously expressed homologue CyFIP1. In particular, CyFIP2 appeared to be expressed predominantly in the cortex and hippocampus (Hauck, unpublished), in line with work from another research group based on a different *Cyfip2-LacZ* reporter mouse model (Han *et al.*, 2015). This led to the assumption that it might be mainly expressed in excitatory neurons, since they represent ~90 % of the neurons in these regions. In this work we went a step further, determining which cell types in the brain express CyFIP2. We performed co-immunofluorescence studies on brain sections, co-labelling CyFIP2 together with specific neuronal and non-neuronal markers. All glutamatergic neurons of the brain, identified by the specific marker NRGN, showed CyFIP2 expression (Figure 11), confirming our hypothesis. Furthermore, other excitatory neurons, such as the large striatal cholinergic neurons, expressed comparable levels of CyFIP2. Surprisingly, dopaminergic neurons completely lacked CyFIP2 (Figure 11). It is still to be seen if adrenergic, serotonergic and the variegated population of inhibitory neurons would express CyFIP2.

In contrast to excitatory neurons, there was no co-localization of the CyFIP2 signal with the glial markers IBA1, MBP or S100β, suggesting that all three subtypes of glial cells are devoid of CyFIP2 (Figure 12).

The expression pattern of CyFIP2 in glutamatergic neurons of the cortex and hippocampus hints at a role of CyFIP2 in excitatory synaptic transmission and possibly learning and memory. Therefore, we generated a conditional knockout mouse model using the *Camk2a-Cre* mouse line, a well-established system to delete genes in glutamatergic neurons of cortex and hippocampus.

When brain slices from these mice were stained using immunofluorescence, no CyFIP2 staining was observed in the NRGN-positive cells (Supp. Figure 1). Seldom, CyFIP2 expressing neurons were observed in the hippocampal pyramidal neuron layer or cortex, but these cells were never NRGN-positive. These observations confirmed both the efficiency and specificity of the conditional knockout, as well as the specificity of the CyFIP2 antibody used for stainings.

3.2. CyFIP2 is crucial for WRC integrity and regulation of dynamic actin filaments

In the conditional knockout mouse, we first analyzed the efficiency of CyFIP2 deletion in cortex and hippocampus. CyFIP2 expression analysis in the cortex and hippocampus of knockout mice at different ages after the expression of the Cre recombinase revealed a strikingly long half-life for CyFIP2, ~12 days (Figure 13), which was significantly higher than the reported half-life of CyFIP2 in HEK293 cells (8.5 hours) (Kumar *et al.*, 2013). In mammalian cultured cells, the half-life of a protein can vary between 0.5-35 hours. Studies in mice have shown that the turnover of proteins is typically slower in the brain, with an average of ~9 days compared to ~3 days in the liver (Price *et al.*, 2010; Toyama and Hetzer, 2013). Nonetheless, CyFIP2 had an even longer half-life compared to long-living neuronal proteins. This could be due to the fact that CyFIP2 forms a very stable complex with NAP1 and the other WRC components, leading to a slower degradation.

An additional possible explanation for the different stability between brain and HEK293 cells could be the different isoform of CyFIP2 expressed in the brain compared to the other organs. In the brain, due to pre-mRNA A → I editing, CyFIP2 has a glutamate at its 320 aa position (320E), in place of a lysine elsewhere in the organism (320K)

(Levanon *et al.*, 2004; Hauck, unpublished). The lysine residue in these cells may be a potential target for ubiquitin binding, leading to its proteasomal degradation. The requirement for high stability of CyFIP2 in neurons may be supported by the distribution of its mRNA in the neuron as well as its function. Cellular fractionation experiments from mouse hippocampi revealed that the *Cyfip2* mRNA is found mainly in the cell body, conversely to *Cyfip1* mRNA that is enriched in synapses (Pilo Boyl, unpublished). Therefore, the long half-life of CyFIP2 may be necessary to ensure the transport of the protein from the soma to the distal ends of the neurons (mostly in axons, as shown in this work) where it functions to remodel actin cytoskeleton and dynamics. This notion is supported in a previous work, where CyFIP2 was shown to be transported along the axons of retinal ganglion cells in a zebrafish model (Cioni *et al.*, 2018).

Structural studies on the WRC demonstrated that its three smaller components, ABI, WAVE and HSPC300, bind to the two large proteins NAP1 and CyFIP, which serve as a scaffold (Chen *et al.*, 2010). Previous studies on the single knockout and knockdown of some WRC components revealed a dramatic decrease of the other members. ABI1 knockout cells showed decreased WAVE1/2, NAP1, CyFIP levels whereas the ABI2 levels were increased possibly to compensate for the loss of its paralogue (Dubielecka *et al.*, 2011). In third instar larval extracts of HSPC300$^{-/-}$ *Drosophila*, CyFIP, ABI and SCAR (analogue of WAVE in *Drosophila*) protein levels were decreased significantly (Qurashi *et al.*, 2007). The knockdown of *Cyfip1* in cultured mouse cortical neurons transduced with shRNAs resulted in a decrease of *Cyfip2*, *Nap1*, *Abi1* and *Hspc300* mRNA levels (Abekhoukh *et al.*, 2017). In agreement with these results, NAP1, ABI1 and WAVE2 protein levels were decreased in the *Cyfip1*$^{+/-}$ mice and *Cyfip1*$^{-/-}$ ES cells (Stöcker, 2015). Analysis of the *Cyfip2* conditional knockout mice showed a similar result, with significantly decreased protein levels of NAP1, WAVE1, ABI1 and HSPC300 (Figure 14). As CyFIP2 forms the WRC together with all these proteins, this results suggest the regulation of WRC co-members upon CyFIP2 loss. ABI2 and WAVE3, which also might form a WRC together with CyFIP2, showed no significant change or high variance in expression levels, respectively. CyFIP1 level was almost unaltered in the conditional knockout mice at P70, as shown in previous studies on the *Cyfip2*$^{+/-}$ mice (Han *et al.*, 2015; Tiwari *et al.*, 2016). However, CyFIP1 levels showed a tendency to increase in the hippocampus of the

Cyfip2 conditional knockout mice. In fact, in aged (>11 months) mice, CyFIP1 levels significantly increased, possibly as a compensatory mechanism to balance the loss of CyFIP2 (data not shown).

The decreased WRC levels upon CyFIP2 loss may lead to decreased ARP2/3 activation in the neurons, possibly leading to less complex actin networks through defects in branching. Interestingly, an F/G-actin separation analysis at 10,000 x *g* in an embryonic (E18.5) *Cyfip2*$^{-/-}$ brain showed conserved F/G-actin ratios (Hauck, unpublished). Since in this embryonic stage there is little formation of pre-synaptic boutons and no dendritic spine formation, the stable actin network is conserved. To better study the effect of CyFIP2 depletion in actin dynamics of the adult mouse brain, F and G-actin levels were measured in more finely fractionated forebrain lysates (Figure 15). In *Cyfip2* conditional knockout mice, F/G-actin ratios were conserved in the nucleic and cytosolic fractions, which contain the bulkier, stable actin filaments that form the basal cytoskeleton. When we analyzed the smaller actin filaments that can only be collected in the 100,000 x *g* ultraspin fraction, we observed a significant increase of filamentous actin compared to the control mice. Although the ultraspin fraction represents only ~2 % of the whole actin in the analyzed tissues, it is the most dynamic pool of actin, playing roles in synaptic dynamics. This dynamic actin pool is involved in processes such as spine maturation and pre-synaptic vesicle exocytosis, where branching of actin filaments is known to be a crucial process.

There are two main possible explanations for the conserved stable actin filaments in the *Cyfip2* conditional knockout mice. Firstly, CyFIP1 levels are unchanged (even slightly increased) in these mice upon *Cyfip2* deletion. Therefore, the WRC formed with CyFIP1 can still function to activate the ARP2/3 complex for the nucleation of branched actin filaments. The CyFIP1 WRC may be involved in the formation of stable actin filaments in the neuron, whereas the CyFIP2 WRC may be responsible for dynamic events. Secondly, although the WRC is the main activator of the ARP2/3 complex, other NPFs such as the class I members WASP, WASH, WHAMM and JMY as well as class II NPFs such as cortactin also function to activate the ARP2/3 complex and produce branched actin networks (Rottner, Hänisch and Campellone, 2010).

Hence, activation of the ARP2/3 complex by the CyFIP2 WRC might represent a small fraction of all actin branching events in the neuron, dominated by the other NPFs.

3.3. Cyfip2 conditional knockout mice show molecular and morphological signs of neurodegeneration with no memory defects

The actin cytoskeleton plays crucial roles in the pre-synaptic vesicle cycle and in post-synaptic receptor trafficking, as well as in the morphological changes of dendritic spines during LTP and LTD (Matus, 2000; Zhai *et al.*, 2001; Hotulainen and Hoogenraad, 2010). All these processes require actin to form branched networks, through the activation of the WRC. As previously mentioned (see chapter 2.2.2 and 3.2), loss of CyFIP2 leads to the decrease of WRC levels in the knockout neurons. Therefore, it is plausible to expect morphological defects of synapses in mice lacking CyFIP2.

In order to study synaptic morphology, we performed ultrastructural analysis of the hippocampus by EM. In both CA1 and CA3 areas of the *Cyfip2*$^{flx/flx}$*;Camk2a-Cre* mice, pre-synaptic terminals showed significantly smaller bouton areas (Figure 19), implying a structural collapse of the pre-synaptic bouton following CyFIP2 loss. These collapsed boutons also had a lower density of synaptic vesicles (Figure 19), which pointed to defects in pre-synaptic vesicle exocytosis and synaptic transmission in the hippocampus. Electrophysiological recordings confirmed the reduced pre-synaptic release probability with decreased frequency of mEPSC events in *Cyfip2*$^{-/-}$ CA1 neurons (Figure 16) and increased paired-pulse ratios in Schaffer collaterals (Figure 18).

We hypothesized that the shrinkage of pre-synaptic boutons as well as defects in pre-synaptic vesicle exocytosis may be accompanied by changes in molecular composition of the pre-synapse over time. In the cortex, pre-synaptic protein levels were in general unaltered in both P130 (Supp. Figure 3) and P330 (Supp. Figure 4) mice. However, when we measured pre-synaptic protein levels, we observed an increase in the levels of several pre-synaptic proteins (VAMP2, SNAP25, MUNC18

and SYN1) in the hippocampus of aged mice (Figure 20, Supp. Figure 2). Most of these proteins are involved in the docking and fusion of vesicles, whereas SYN1 serves as a link between the vesicles and the actin cytoskeleton (Hirokawa, 1989; Rizo and Südhof, 2002). Therefore, the increase of pre-synaptic protein levels during aging appears to be a compensatory mechanism of the neurons to counter the decrease of pre-synaptic vesicle exocytosis efficiency due to the shrinkage of the synapse and the substantial loss of vesicle density.

The shrinkage of pre-synaptic boutons upon CyFIP2 loss and the previous studies on the *Cyfip2*$^{+/-}$ mice showing an Alzheimer's-like phenotype (Tiwari *et al.*, 2016) pointed to a possible role of CyFIP2 in neurodegeneration. Since our mouse model had a complete deletion of CyFIP2 in the hippocampus, where the most prominent AD pathology is observed, we expected an enhanced AD phenotype in *Cyfip2*$^{flx/flx}$*;Camk2a-Cre* mice. Yet we could only observe mildly increased APP levels in hippocampal synaptosomes (Figure 21), and not in hippocampal total lysates (Supp. Figure 6) of aged mice, as it was previously observed in the *Cyfip2*$^{+/-}$ mice (Tiwari *et al.*, 2016). This suggested that the loss of CyFIP2 leads to a localized dysregulation of APP translation in the synapse, reminiscent of FMRP mode of action. While CyFIP1 has been shown to function in FMRP-dependent regulation of mRNA translation through eIF4E binding (Napoli *et al.*, 2008; De Rubeis *et al.*, 2013), a potential role of CyFIP2 in mRNA translation regulation was never formally shown. We show here, for the first time, that CyFIP2, similarly to CyFIP1, can be found in the cap-binding complex, in a m^{7}GTP beads pull-down experiment (Figure 23). However, it is important to note that we observed a very transient, weak interaction between both CyFIPs and the cap-binding complex, which was easily dissociated by repeated washes of the beads. Conversely to previous work by Tiwari et al., we did not observe any differences in APP and BACE1 levels in cortical total lysates (Supp. Figure 7) or synaptosomes (Supp. Figure 8) of the *Cyfip2*$^{+/-}$ mice, which was in fact in line with observations by Han et al.

Neurodegeneration, in addition to synaptic loss, is characterized by the loss of neurons and the appearance of astrogliosis due to tissue damage caused by accumulation of cellular debris. When we analyzed aged *Cyfip2* conditional knockout mice, we did not

observe any loss of neurons, although a mild astrogliosis was visible in the hippocampus (Figure 22) and cortex (Supp. Figure 9). This effect could be due to the collapsing of the pre-synaptic boutons upon defects in actin branching, inducing a higher astrocytic activity.

Spine maturation following persistent stimulation from the pre-synaptic terminal is accepted as the morphological basis of learning and the formation of long-term memory. With a lack of adequate stimuli from the pre-synaptic site, we hypothesized that the *Cyfip2* conditional knockout mice might show defects in memory formation and/or maintenance. Despite the morphological (pre-synaptic shrinkage) and molecular (increased APP levels) predisposition, *Cyfip2* conditional knockout mice did not show defects in working memory or short-term memory, assessed by Y-maze (Figure 28) and NOR (Figure 29) tests, respectively. This was partially unexpected since previous studies on the *Cyfip2*$^{+/-}$ mice showed impairments in retention of spatial memory in a MWM (Tiwari *et al.*, 2016). However, it is important to note that the MWM is a highly stress-inducing test for mice, which forces mice to perform the learning assignment as a survival task. Although this might reveal phenotypes that are too mild to be observed with a less stress-inducing test, in mice with anxiety-like behaviors the results may be altered due to the anxiety-like phenotype and not explicitly due to a memory defect.

3.4. CyFIP2 loss leads to an FXS-like phenotype in the post-synapse

Despite biochemical and morphological indications, a neurodegeneration phenotype was not confirmed in the *Cyfip2* conditional knockout mice. Thereon we focused on the link of CyFIP2 with FMRP, which shows significant phenotypes in dendritic spine morphology (Han *et al.*, 2015). At P130, the average PSD length of CA3 neurons was increased in *Cyfip2* conditional knockout mice, possibly in a first attempt to make up for the loss of contact surface from the pre-synaptic site, whereas in the CA1, the average PSD length was unchanged (Figure 19). These findings were supported by conserved amplitudes and rise/decay times of mEPSC in *Cyfip2*$^{-/-}$ CA1 neurons, pointing to conserved membrane properties and AMPA receptor distribution in the

post-synaptic terminals (Figure 16). Although there were no obvious post-synaptic changes in the P130 mice, we speculated that the persistent lack of adequate pre-synaptic input may induce dendritic spines defects in the aged mice.

The morphological analysis of the brains of aged (14-month-old) mice revealed comparable cortical layering and number of neurons between the two genotypes (Supp. Figure 10). Detailed analysis of dendritic spines in *Cyfip2* conditional knockout mice revealed increased total spine density in both CA1 neurons of the hippocampus (Figure 24) and layer V (Supp. Figure 11) neurons of the cortex. Nevertheless these spines were mainly immature by their morphology (Figure 25, Supp. Figure 12). Comparably, in *Cyfip2*$^{+/-}$ mice, total spine numbers were reported unchanged in the hippocampus (Han *et al.*, 2015), with decreased mature/immature spine ratios (Tiwari *et al.*, 2016). In the case of CyFIP2 loss, the dendritic spine morphology is possibly altered due to three different mechanisms. The significant reduction of WRC levels due to the absence of CyFIP2 directly affects actin polymerization, which could prevent spine maturation or favor the activity of non-branching actin nucleators, such as formins. Indirectly, since CyFIP2 loss leads to pre-synaptic shrinkage accompanied by decreased vesicle exocytosis and synaptic transmission, the decreased input from the pre-synapse is likely not enough to trigger adequate post-synaptic response to activate downstream signaling pathways (such as CAMK2A) necessary for spine maturation. The decreased pre-synaptic input is possibly also the reason for the increased total spine number, an attempt to increase post-synaptic neurons activation. However, due to the lack of sufficient input (since pre-synaptic terminal density is heavily decreased), these spines are unable to develop, thus remaining immature. Lastly, the alterations in spine morphology could be explained by the possible role of CyFIP2 in mRNA translational regulation. CyFIP2 loss might lead to decrease in translational control of mRNA targets (such as APP) that affect spine morphology, as in FXS. However, this effect might not be as severe as in the case of the *Fmr1*$^{-/-}$ mice, since CyFIP1 may partly compensate for the translational regulation function of CyFIP2 mRNA targets. Since the selection of the mRNAs depends on FMRP, it is reasonable to think that both CyFIPs act indiscriminately in regulating FMRP target mRNAs translation. Therefore, the loss of CyFIP2 is only decreasing the total amount of available synaptic eIF4E-BP to fulfill this function, which might even be partially

compensated by the CyFIP1 increase, as seen starting as a tendency in P70 mice (Figure 14) but ending with a significant increase in aged mice (data not shown).

The increase of total spine number with decreased mature/immature spine ratio observed in the *Cyfip2* conditional knockout mouse is also a hallmark of the well-described FXS mouse model, the *Fmr1*$^{-/-}$ mouse. In fact, in the *Fmr1*$^{-/y}$*;Cyfip2*$^{+/-}$ double mutant mice, the densities of total cortical spines and of immature spines were further increased compared to the *Fmr1*$^{-/y}$ mice (Han *et al.*, 2015), suggesting an effect of CyFIP2 decrease in dendritic spine development and morphology. Along with the dendritic spine phenotype, the *Fmr1*$^{-/-}$ mouse model is characterized by repetitive behaviors, hyperactivity, increased locomotion and short-term memory defects (Kazdoba *et al.*, 2014). *Cyfip2* conditional knockout mouse, on the other hand, showed decreased locomotion in both open-field (Figure 27, Supp. Figure 14) and Y-maze (Figure 28) tests, by significantly entering the arms fewer times compared to controls. The mice also showed less rearings, indicating decreased exploratory behavior. The open-field test performed after different habituation times revealed a mild difference in the anxiety response of the *Cyfip2* conditional knockout mice (Figure 27). This lack of a clear anxiety phenotype was also true for the *Cyfip1*$^{+/-}$ mice, which showed normal behavior in the open-field test (Bozdagi *et al.*, 2012).

Another consequence of the dendritic spine defects observed in *Cyfip2* conditional knockout mice might be ASD-like phenotypes. Increase in spine numbers and decreased mature/immature spine ratios have also been observed in ASD (Martínez-Cerdeño, 2017). CyFIP involvement in autism has been proposed previously. Genome-wide expression profiling of ASD patients tissue databases has identified significant upregulation of *Cyfip1* mRNA due to a duplication in 15q11-q13 region of the genome, encompassing the *Cyfip1* gene (Nishimura *et al.*, 2007). Microdeletion of the 15q11.2 region in Prader-Willi patients, which contains *Cyfip1*, has been associated with the ASD phenotype of the patients (Doornbos et al., 2009). *Cyfip1*$^{+/-}$ mice have been shown to display ASD-like behaviors, such as reduced preference for novelty and enhanced inhibitory avoidance extinction during fear conditioning (Bozdagi *et al.*, 2012; Domínguez-Iturza *et al.*, 2019). Recently, using RT-qPCR, the levels of both *Cyfip1* and *Cyfip2* mRNA were shown to be elevated in the blood of ASD

patients (Noroozi *et al.*, 2018). The *Cyfip2* conditional knockout mice did not show repetitive, autistic-like behaviors (Figure 28), as previously reported for the *Cyfip2*$^{+/-}$ mice using a different test, the marble burrowing task (Tiwari *et al.*, 2016) and showed normal preference for novelty in a NOR test (Figure 29). Despite the lack of some elements of the ASD phenotype, *Cyfip2* conditional knockout mice demonstrated decreased breeding rates, suggesting decreased social interactions. The social aspect could be explored more deeply, for example a male intruder test or the three chamber social interaction and social preference test could be performed to accurately measure social behaviors in these mice. Moreover communication was not yet addressed in *Cyfip2* conditional knockout mice. Specific tests that measure ultrasound acoustic vocalizations of males in the presence of a female odor or of pups separated from their mother could shed light on this other aspect relevant for ASD.

A possible molecular mechanism that could explain the pre-synaptic shrinkage phenotype as well as defects in spine maturation is autophagy. Previous work on mice lacking ATG7, an enzyme involved in the formation of autophagosomal vesicles, in dopaminergic neurons showed a decreased number of synaptic vesicles and attenuated release of dopamine (Hernandez *et al.*, 2012). This suggested that autophagy is directly involved in the regulation of synaptic vesicle density and consequently exocytosis in the pre-synapse. Following studies pointed to the idea that pre-synaptic autophagy is distinct from basal autophagy and is activity-dependent. The cytoskeletal proteins BSN (Bassoon) and PCLO (Piccolo) were found to be negative regulators of pre-synaptic autophagy in hippocampal neurons. The double knockdown of these proteins led to increased autophagosomal vesicles in pre-synaptic boutons, resulting in the progressive loss of synaptic vesicle pools via degradation (Waites *et al.*, 2013; Reimer *et al.*, 2017). In the post-synapse, autophagy was shown to be involved in the degradation of neurotransmitter receptors and spine pruning. Deletion of ATG7 in excitatory neurons showed an increased number of spines, which were accompanied by autistic-like behaviors in mice (Tang *et al.*, 2014). In light of these findings, we analyzed the levels of autophagy markers in the hippocampus (Figure 26) and cortex (Supp. Figure 13) of the *Cyfip2* conditional knockout mice, finding no alterations. Our data suggest that the synaptic collapse observed upon CyFIP2 loss is not due to an increase in autophagy, supporting the

hypothesis that it is likely caused by a structural collapse due to the lack of branched actin formation.

3.5. Conclusions and outlook

In this thesis, for the first time, we showed the expression of CyFIP2 in different cell types of the brain. Using immunofluorescence, we showed CyFIP2 expression in glutamatergic and cholinergic neurons (see chapter 2.1.1), whereas dopaminergic cells lacked CyFIP2. Glial cells were devoid of CyFIP2 (see chapter 2.1.2).

Further, we demonstrated the role of CyFIP2 in the adult mouse brain using a conditional knockout mouse model, deleting the protein in glutamatergic neurons of the cortex and hippocampus. Upon deletion of the protein starting at ~P18, we showed that CyFIP2 has a strikingly long half-life which leads to its complete loss only at P70 (see chapter 2.2.1). This was significantly higher than the half-life of CyFIP2 observed in cell culture. One explanation for this could be the different isoform found in the brain (320E) compared to the rest of the organism (320K), which possibly protects the brain isoform from degradation through ubiquitination. An interesting question is how the half-life of CyFIP1 compares to CyFIP2 in the brain. From work in our lab, it is known that the mRNA levels of *Cyfip1* were enriched in the synapses whereas *Cyfip2* mRNA was mainly found in the soma (Pilo Boyl, unpublished). The transport of CyFIP2 along the axons to the distal ends of neurons may require the long half-life observed in this thesis, which may not be needed for CyFIP1 due to its mRNA being in the synaptic compartments.

With the loss of CyFIP2, levels of all known co-members of the WRC were significantly reduced (see chapter 2.2.2). However, the loss of the CyFIP2-WRC did not lead to alterations in the levels of the stable F-actin pool (see chapter 2.2.3). Upon CyFIP2 loss, protein levels of CyFIP1 remained almost unchanged, with a tendency for increase. Indeed, this increase became clearer in older age, where CyFIP1 might be compensating for the loss of CyFIP2. A CyFIP1 conditional knockout mouse model under the *Camk2a* promoter might provide insights into how the two paralogues compare to each other during development and in the adult brain.

Our data showed that the loss of CyFIP2 leads to a dramatic shrinkage of pre-synaptic boutons in the hippocampus (see chapter 2.3.3), which leads to defects in excitatory synaptic transmission and vesicle exocytosis (see chapter 2.3.1). On the post-synaptic site, CyFIP2 loss resulted in an increased number of spines (see chapter 2.5.1). However, when analyzed in detail, we observed that these spines were mainly immature (see chapter 2.5.2). This was possibly due to both lack of adequate pre-synaptic stimulation and defects in actin branching through the WRC. According to our data, autophagy was not the molecular mechanism for the observed defects (see chapter 2.5.2). Hitherto, one known upstream regulator of CyFIP (and the WRC) is RAC1, which has been shown to regulate spine morphology upon activation by NMDA receptors signaling during synaptic transmission. Signaling pathways regulating pre-synaptic maintenance are so far unknown, CyFIP2 may be an important regulator of pre-synaptic morphology both in the developing and the adult brain.

Although *Cyfip2* conditional knockout mice showed dramatic defects in both pre- and post-synaptic morphology, as well as increased APP levels in hippocampal synapses, no obvious behavioral impairments were observable in aged mice (see chapter 2.6). Previous work on the *Cyfip2*$^{+/-}$ mice showed defects in the retention of spatial memory in an MWM test. Our data from the NOR (see chapter 2.6.3) and Y-maze (see chapter 2.6.2) tests, which asses short-term and working memory, showed no memory defects in the *Cyfip2* conditional knockout mice. This led to the hypothesis that the test performed in this work may be too mild to uncover limited memory defects as a result of decreased mature spines upon CyFIP2 loss. Further behavioral studies using MWM or fear conditioning could reveal the possible learning and/or memory defects in these mice.

4. Methods

4.1. Molecular biology

4.1.1. Genomic DNA extraction

In order to extract genomic DNA, mouse tails or ear punches were put in 200 µl of DNA extraction buffer with 0.5 µg/µl proteinase K. Proteins in the biopsies were digested at 55˚C o/n. Next day, the samples were mixed briefly and 100 µl saturated NaCl solution was added. The tubes were shaken rigorously for 1 minute and centrifuged at 14000 RPM for 15 minutes at RT. 230 µl of the supernatant was added into 500 µl of absolute ethanol, resulting DNA to flocculate. Samples were centrifuged at 14000 RPM for 1 minute and the supernatant was removed using a Pasteur pipette. The leftover solution was dried at 37˚C for 5 minutes and pellet was resuspended in 200 µl Milli-Q H_2O by shaking ~30 minutes at 37˚C.

4.1.2. Polymerase chain reaction (PCR)

PCR is a method used in molecular biology to multiply the number of DNA sequences using thermal cycling. In this method, primers that are complementary to the target DNA sequence are used together with a DNA polymerase in order to amplify the targeted DNA sequence exponentially (Yang and Mahmood, 2012).

The (genomic) DNA was denatured at 94-98˚C for 30 seconds to 2 minutes, separating the leading and lagging strand of DNA to serve as ssDNA (single-stranded DNA) templates for the reaction. Specific primers, which are ~18-25 nucleotide (nt) long oligonucleotide sequences, complementary to the ssDNA templates annealed to them at ~55-65°C for 15-90 seconds. These pairs of primers targeted both the 5´-3´ (sense/forward) and 3’-5’ (antisense/reverse) direction of the DNA and form the basis for the polymerization to begin. The DNA was then polymerized using the *Taq* polymerase (isolated from *Thermus aquaticus*) that elongates the primers in the 5’-3’ direction at 72°C by catalyzing the incorporation of freely available dNTPs in the reaction buffer. For the catalytic function of *Taq* polymerase, divalent Mg^{2+} ions were provided in the solution as $MgCl_2$. This process of denaturation, annealing and elongation was repeated in 25-35 cycles which exponentially (2^n, n= number of cycles) multiplies the number of targeted DNA sequence.

4.1.2.1. Use of mice and genotyping by PCR

Mice were kept according to legal regulations. Breeding and experiments were approved under AZ84-02.04.2017.A088 and AZ81-02.04.2019.A241. To determine the genotypes of mice, genomic DNA was extracted as described in chapter 4.1.1 and PCR was performed as follows.

4.1.2.1.1. *Cyfip2-flx* PCR

The following PCR reaction was performed to determine whether the mice had floxed *Cyfip2* genes, using primers (703, 718, 753) listed in chapter 5.5 (Figure 30). 1 µl of genomic DNA was added in 19 µl of PCR master mix.

Table 1. *Cyfip2-flx* genotyping PCR master mix preparation protocol.

PCR reagent	Concentration	Amount (in µl)
Milli-Q H2O		12.45
PCR-flexi-buffer	5x	4
MgCl2	25 mM	1.2
dNTPs	10 mM	0.4
703/753	20 µM	0.5
718/753	20 µM	0.25
Taq polymerase	5 u/µl	0.2

Table 2. *Cyfip2-flx* genotyping PCR conditions.

Temperature	Time	
98 °C	2 min	
96 °C	30 sec	(35 cycles)
56 °C	60 sec	
72 °C	30 sec	
72 °C	5 min	

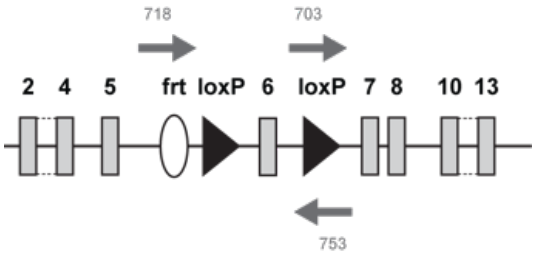

Figure 30. Primers for *Cyfip2-flx* PCR.
Two forward primers (703 and 718) were combined with a reverse primer (753) to check for floxed Cyfip2 alleles and possible deletions, respectively.

4.1.2.1.2. *Camk2a-Cre* PCR

To determine whether the mice had Cre recombinase under the *Camk2a* promoter, the following PCR reaction was made using primers (386, 387, 618) listed in chapter 5.5. 1 µl of genomic DNA was added in 19 µl of PCR master mix.

Table 3. *Camk2a-Cre* genotyping PCR master mix preparation protocol.

PCR reagent	Concentration	Amount (in µl)
Milli-Q H2O		12.2
PCR-flexi-buffer (5x)	5x	4
MgCl2 (25 mM)	25 mM	1.2
dNTPs (10 mM)	10 mM	0.4
386/618 (20 µM)	20 µM	0.5
386/387 (20 µM)	20 µM	0.5
Taq polymerase (5 u/µl)	5 u/µl	0.2

Table 4. *Camk2a-Cre* genotyping PCR conditions.

Temperature	Time	
98 °C	2 min	
96 °C 58 °C 72 °C	30 sec 30 sec 40 sec	(30 cycles)
72 °C	5 min	

4.1.3. Gel electrophoresis

Agarose gel electrophoresis is a common method in molecular biology, which is used to separate DNA fragments according to size (Stellwagen, 2009). Due to the phosphate residues on their backbone, nucleic acids are negatively charged, therefore they can be run on a gel towards the cathode (+) using an electrical current. The sizes of DNA fragments are then compared to a marker with known sized bands to determine PCR products.

To visualize the products of PCR, 10 µl of PCR products were loaded on 1.5-2.5 % (w/v) agarose gels prepared in 1x TAE buffer. The gels were ran at a constant voltage of 90 V for 20 minutes-1 h. The agarose gels contained ethidium bromide (7-9 µl from 10 mg/ml stock in 100 ml gel), which intercalates to DNA and fluoresces under UV light, making the DNA visible.

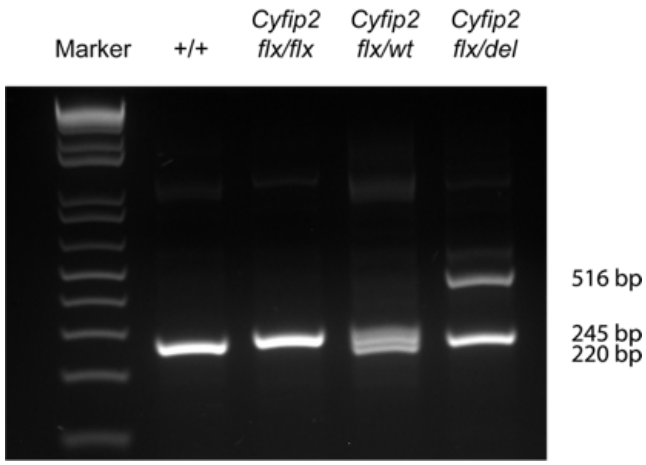

Figure 31. *Cyfip2*-flx genotyping results. The combination of primers 703 & 753 resulted in a wt band for Cyfip2 with 220 bp and a loxP3 band at 245 bp. The primers 718 & 753 were used to check for possible deletions in the locus, which resulted in a fragment of 516 bp.

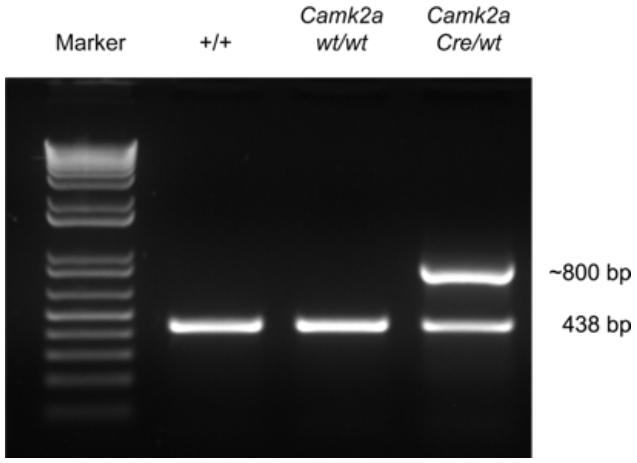

Figure 32. *Camk2a*-Cre genotyping results.
The combination of primers 386 & 618 resulted in a wt band for *Camk2a* with 438 bp. The Cre allele at ~800 bp resulted from the combination of primers 386 & 387.

4.2. Biochemistry

4.2.1. Protein isolation from tissue

In order to isolate proteins from brain tissues, mice were sacrificed by cervical dislocation and decapitated. The brains were removed quickly and cortex, hippocampus and cerebellum were dissected. Tissues were either shock frozen in liquid N_2 and stored -80˚C or were directly homogenized to prepare lysates.

To prepare total protein lysates, (fresh or frozen) tissues were homogenized in 2x SDS loading buffer (1 ml for one cortex hemisphere or cerebellum, 200 µl for two hippocampi), in a glass/teflon douncer at 600 RPM with 10 slow strokes. Homogenized samples were then transferred in an Eppendorf tube and placed on a heating block at 99˚C for 10 minutes. Samples were briefly vortexed every two minutes to ensure lysis of proteins. After the tubes were cooled down at RT, lysates were placed in -20˚C for storage.

4.2.2. Protein quantification

To quantify the amount of proteins in a sample, Bradford assay was used. Bradford assay is a colorimetric assay that relies on the absorbance shift of the Coomassie Brilliant Blue dye (Bradford, 1976). Coomassie Brilliant Blue is a dye that is used in biochemistry to stain proteins by binding to their carboxyl and amino groups noncovalently and electrostatically, respectively. The dye has a brown color with an absorbance of 465 nm when it is not bound to any protein. The formation of the protein-dye complex stabilizes the anionic form of the dye while producing a blue color at 595 nm. This shift in the absorption is measured by a spectrophotometer, which is calibrated by using serial dilutions of a known protein (in this case BSA) against a blank sample (lysis buffer) that does not contain any protein. The absorbance of samples were plotted against the protein (BSA) concentration in the sample to obtain the calibration curve for a certain Bradford reagent.

4 µl of tissue lysate (or Milli-Q H_2O for the blank sample) was boiled with 1 µl of 5x SDS loading buffer and boiled at 99˚C for 2-3 minutes. The samples were diluted 10 times by adding 45 µl of Milli-Q H_2O and 12.5 µl of the diluted sample was added in 1 ml of Bradford reagent. For samples that were already in 2xSDS loading buffer, 10 µl of the sample (or 2x SDS loading buffer for the blank sample) was added in 1 ml of Bradford reagent. The measured absorbance of samples against their respective blank was divided by the slope of the calibration curve to calculate the protein concentration of samples in µg/µl.

4.2.3. Discontinuous SDS-polyacrylamide gel electrophoresis

SDS-polyacrylamide gel electrophoresis (SDS-PAGE) is a method used in molecular biology to separate proteins in a given sample according to their molecular weight (Manns, 2011). The proteins are denatured and negatively charged by SDS and β-mercaptoethanol is used to reduce the disulfide bonds.

In order to separate proteins, the samples were run through polyacrylamide gels consisting of two different parts. The top part of the gel, stacking gel, is a 4 % acrylamide gel with a pH of 6.8 and it is used to concentrate the samples to a thin line. The resolving gel is the bottom part of the discontinuous gel that had a pH of 8.8 and had an acrylamide concentration of 10 % or 15 %. The concentration of acrylamide was chosen according to the molecular weight of the proteins that were investigated. For bigger proteins that have high molecular weight, a 10 % acrylamide gel was chosen, whereas for smaller proteins, a 15 % acrylamide gel with a dense mesh of polymers were preferred in order to achieve high separation resolution. The gels were placed in PAGE chambers filled with SDS running buffer. Samples were loaded in the wells on top of the stacking gel and electrodes were placed over the chambers. Negatively charged samples were ran towards the cathode at 80 V for ~30 minutes. Once they reached the resolving gel, voltage was increased to 150 V and samples were ran until they flowed out of the gel.

4.2.4. Western blotting

To detect specific proteins in a sample, proteins ran on acrylamide gels were transferred onto PVDF membranes using western blotting (see chapter 4.2.4.1) (Yang and Mahmood, 2012). Afterwards, specific antibodies were used in combination to luminescent detection methods (see chapter 4.3.4.2).

4.2.4.1. Submerged transfer

Transfer of proteins from an acrylamide gel onto the PVDF membranes were performed via a wet blot, in which the so called “transfer sandwich” is submerged in a buffer.

Following the SDS-PAGE, gels were removed from the chambers and placed in the transfer solution along with other components. The transfer sandwich was prepared by placing a sponge, two Whatman papers, acrylamide gel, methanol activated PVDF membrane, two more Whatman papers and another sponge in between a tightly closed casket. The caskets were placed in transfer chambers that were filled with cold Towbin transfer buffer and an ice block was placed to keep the system from overheating during transfer. The proteins were transferred to the PVDF membrane by the application of a voltage of 110 V for 70 minutes or 20 V o/n.

4.2.4.2. Enhanced chemiluminescence detection

Following the transfer of proteins, the membranes were washed quickly with 1x NCP and were blocked in membrane blocking solution for 30 minutes at RT. Specific primary antibodies targeting desired proteins were incubated o/n at 4˚C. The next day, membranes were washed three times with 1x NCP for 15 minutes at RT on a shaker. Secondary antibodies conjugated to HRP were incubated for 30 minutes at RT and were washed three times with 1x NCP for 10 minutes at RT on a shaker. In the end, the membranes were developed using enhanced chemiluminescent (ECL) solution.

The ECL solution was prepared by mixing two parts, A and B in 1:1 ratio. Solution A contained luminol and solution B contained H_2O_2. In the presence of H_2O_2 and HRP, thus only where the secondary antibodies were bound, luminol was oxidized. Upon oxidization, luminol emits a light signal at 450 nm, which was measured using a luminescent image analyzer with a CCD camera (LAS 4000 mini).

4.2.4.3. Western blot quantification

To compare the relative protein levels in different samples, the signal (light emitted) from the ECL reaction was used. Multi Gauge V3.0 software was used to quantify the signal intensity of each protein on different lanes and gels. Different gels were compared by using a common sample which was loaded on all gels.

4.2.4.3.1. Coomassie staining of membranes

A conventional method to normalize loading errors and possible deviation in transfer of proteins to the membrane is the use of standard proteins (such as GAPDH, gamma tubulin or actin) in tissues. However, this method is only reliable in when lysates of same tissues are compared since the expression of these proteins vary depending on the tissues. In order to overcome this problem and normalize proteins reliably, a Coomassie staining was performed on the membranes at the end of each western blot experiment.

Once all the proteins were imaged using ECL method, the membranes were placed in Coomassie staining solution for 5 minutes on a shaker at RT. The membranes were then washed with destaining solution for 2-3 minutes on the shaker at RT. Membranes were air dried on a Whatman paper until the parts that do not contain proteins turned white. The dried membranes were then imaged using a scanner and the total protein levels were measured using Multi Gauge software (Figure 33).

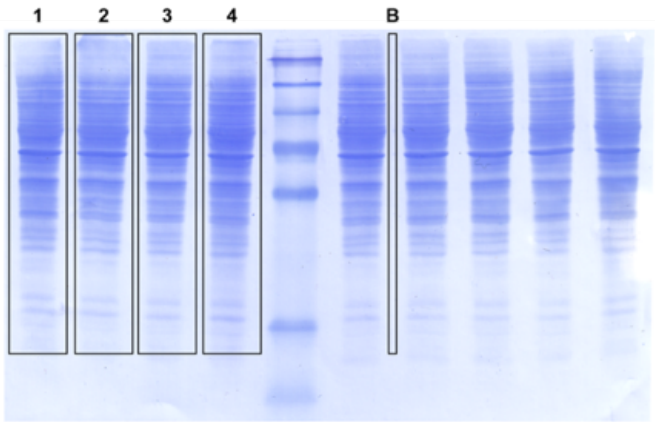

Figure 33. Quantification of Coomassie stained PVDF membranes.
Using Multi Gauge software, areas were defined around the Coomassie stained proteins for each lane (as shown in lanes 1, 2, 3 and 4). For the background (B), an area between the lanes was chosen. Using a densiometric analysis, the signal from the background was subtracted from the signals in each lane, resulting in the true signal from the total proteins. The signal from an antibody was then divided to the total protein signal from its respective lane for normalization.

4.2.6. Analysis of cellular fractions

In order to determine F/G-actin levels in different cellular fractions, the following protocol was followed. First the mice were sacrificed by cervical dislocation and the brains were quickly removed. One hemisphere of cortex was dissected together with hippocampus, while the striatum was removed. The cortex and hippocampus were dounced in lysis buffer with 1 mM PMSF inhibitor at 600 RPM on ice with 10 slow strokes. The homogenate was left on ice for 5 minutes for lysis. The samples were centrifuged at 200 x *g* for 5 minutes at 4°C (nucleic fraction). The pellet was resuspended in 300 µl 2x SDS loading buffer and 30 µl of 5x SDS loading buffer was added on 150 µl of the supernatant. From the remaining supernatant, 1 ml was taken and was centrifuged at 10,000 x *g* for 10 minutes at 4°C (cytosolic fraction). The pellet was resuspended in 100 µl 2x SDS loading buffer and 30 µl of 5x SDS loading buffer was added on 150 µl of the supernatant. 650 µl of the cytosolic fraction supernatant was centrifuged at 100,000 x *g* for 30 minutes at 4°C (ultraspin fraction). The pellet was resuspended in 100 µl 2x SDS loading buffer and 30 µl of 5x SDS loading buffer was added on 150 µl of the supernatant. All samples were boiled at 99°C for 10 minutes and then were run on 10 % acrylamide gels.

4.2.7. Synaptosomal preparation

To prepare synaptosomes, either one hemisphere of cortex or both hippocampi were dissected quickly. Both tissues were homogenized in a homogenizing buffer at 250 RPM on ice with 10 slow strokes. Samples were centrifuged at 3,000 x *g* for 10 minutes at 4°C. The supernatants were recovered and further centrifuged at 14,000 x *g* for 12 minutes at 4°C. Synaptosomes were resuspended in Krebs-Ringer buffer and ~40-45 % (v/v) Percoll was added. After gentle mixing, samples were centrifuged at 14000 RPM for 2 minutes at 4°C. Enriched synaptosomes floating on the surface were recovered by aspirating the underlying solution with a syringe. The synaptosomes were washed with 1 ml of Krebs-Ringer buffer. After a 30 seconds centrifugation at 14000 RPM, cortical and hippocampal synaptosomes were resuspended in 600 and 200 µl Hepes-Krebs buffer, respectively. 5x SDS loading buffer was added on the samples and they were boiled at 99°C for 10 minutes.

4.2.8. m^7GTP pull-down

In a eukaryotic cell, the cap-dependent translation of mRNAs begin by the binding of 40S subunit of the ribosome to the 5' cap, which is a 7-methyl-guasosine (m7GpppX) structure. The eIF4E is a protein involved in directing ribosomes to the 5' cap, thus initiating the translation. To determine the potential involvement of CyFIP2 in translation regulation, a pull-down experiment was performed using m^7GTP coated Sepharose beads that mimic the 5' cap of an mRNA. 50 µl slurry of m^7GTP-Sepharose beads were spun down and the EtOH was removed. Beads were equilibrated with 500 µl PBS with 1 mg/ml BSA at 4°C for 30 minutes on a rotating wheel. The resin was washed off twice with 500 µl of buffer P. One half of a mouse brain (excluding cerebellum) was slowly dounced ~10 times in 5 ml of buffer P including protease inhibitor cocktail and 40 u/ml RNAseOut at 600 RPM. The lysates were incubated 15 minutes on ice and then centrifuged at 14,000 x *g* at 4°C for 10 minutes. ~700 µg of the supernatant (input) was added onto the beads and incubated for 2 hours at 4°C on a rotating wheel. After the incubation, the supernatant (unbound fraction) was collected and the beads were washed either three times with 1 ml of buffer P or one time with 400 µl of buffer P. After the last wash, 2 x SDS was added onto the beads and boiled for 10 minutes at 99°C. The elution (bound fraction) was collected from the beads. The samples were loaded on a 10 % acrylamide gel and western blotting was performed.

4.3. Histology

4.3.1. Preparation of gelatin-coated slides

A common adhesive reagent used to ensure sections holding on the slides during the washing and staining procedures is gelatin. For the Golgi stainings, chrome alum gelatin solution covered slides were used. Microscope slides were placed vertically in a glass staining rack filled with warm (50°C) chrome alum solution on a magnetic stirrer shortly and then were airdried o/n at RT.

4.3.2. Golgi stainings

Golgi's method is a silver staining method developed by Camillo Golgi to stain nervous tissue (Kang *et al.*, 2017). The staining of neurons is achieved by micro crystallization of silver chromate, which is formed by mixing $HgCl_2$, K_2CrO_4 and $K_2Cr_2O_7$. For the Golgi stainings of brains, a kit from FD NeuroTechnologies was used. At least 24 hours before the starting of stainings, the impregnation solution (20 ml/mouse) was prepared by mixing equal volumes of solution A and B under the fume hood. The solution was placed in dark at RT, unstirred. The next day, mice were sacrificed by cervical dislocation and the brains were removed quickly. After a brief wash in Milli-Q H_2O to remove blood from the surface, they were immersed in 10 ml of impregnation solution and placed on a shaker in the dark at RT. The impregnation solution was replaced on the next day. After three weeks of incubation in the impregnation solution, the brains were transferred into the washing solution (solution C) on a shaker in the dark at 4°C. The solution was replaced after the first 24 hours of immersion and, in total, the brains were kept in solution C for three days. 200 µm coronal sections were cut in PBS using a vibratome and were placed on gelatin-coated slides with a drop of solution C. Excess solution was suctioned with a pipette and absorbed with a filter paper. Sections were left to dry at RT in the dark, o/n. The next day, slides were placed vertically in a glass staining rack and were rinsed with Milli-Q H_2O twice, 2 minutes each. Sections were placed in freshly prepared staining solution (by mixing 35 ml of solution D, 35 ml solution E and 70 ml of Milli-Q H_2O) for 10 minutes on a shaker at RT. After the staining, the sections were rinsed in Milli-Q H_2O twice, 4 minutes each. The sections were then dehydrated in 50 %, 75 %, 95 % and absolute ethanol for 1 minute each on a shaker. Lastly, the sections were cleared in xylene three times, 4 minutes each and were mounted with Entellan. After an o/n drying, brightfield images of cortex and hippocampus were taken using a brightfield microscope.

4.3.1.1. Dendritic spine analysis

The advantage of Golgi's method comes from the random deposition of silver precipitates, which leads to staining in only a random subset of neurons. This random staining makes it possible to visualize the complex dendritic morphologies of neurons

in the brain. In order to visualize dendritic spines of cortical (layer V) and hippocampal (CA1) neurons, brightfield z-stack images (with 1 µm pitch) were taken using a 60x objective in a brightfield microscope. Number of immature (thin) and mature (stubby and mushroom) spines were counted on a dendritic branch and the length of the area was measured. Number of spines per 10 µm area were counted using Image J cell count plugin.

4.3.3. Quantitative electron microscopy

For a quantitative analysis of bouton changes in hippocampal regions CA1 and CA3, electron microscopy was performed by a collaboration with Dr. David Lutz (Ruhr-Universität Bochum). Animals were anaesthetized with sodium pentobarbital and perfused transcardially by a fixative solution containing 4 % paraformaldehyde and 1 % glutaraldehyde in 0.1 M sodium cacodylate buffer (pH 7.4). Fixed brains were isolated and stored in fixative solution at 4°C o/n, washed in PBS, and sectioned coronally on a vibratome at a thickness of 200 µm. The sections were post-fixed in 1 % OsO_4 for 30 minutes. After rinsing in distilled water and dehydration in an ascending series of ethanol (block-staining with 0.5 % uranyl acetate in 70 % ethanol), the hippocampi were embedded in Epon and hardened at 65°C for two days. Thin sections from *stratum lucidum* of area CA3 and *stratum radiatum* of area CA1 were cut on an ultratome and mounted on butvar-coated 50-mesh copper grids. Sections were post-stained with lead citrate and subjected to electron microscopy (6,600x magnification). The area of the pre-synaptic bouton profiles and synaptic vesicle density per bouton area were assessed. To avoid multiple measurements of the same bouton, randomized sections 5 µm apart from each other were analyzed and at least 10 micrographs per mouse in the cohorts of four animals per condition were used.

4.3.4. Immunofluorescence

Mice were sacrificed by cervical dislocation and the brains were quickly removed from the head. Excessive blood was cleaned with a wet paper and the brains were fixed in 4 % PFA/PBS for ~40 hours at 4°C on a shaker. After fixation, coronal brain sections of 25 µm thickness were cut using a vibratome. After the slicing, sections were stored

in 1x PBS with 0.1 % NaN_3 at 4°C. The sections were transferred to 24-well plates with an aluminum foil lid and were post-fixed for 20 minutes in 4 % PFA/PBS at RT on a shaker. Afterwards the slices were treated with 1 % SDS and 5 % mercaptoethanol for 5 minutes at RT for the unmasking of covered epitopes. Slices were then washed three times with PBT for 1 minute at RT on a shaker, which was followed by three washes of PBT-Glycine for 10 minutes at RT. The slices were then blocked for 2 hours at RT with blocking solution containing 5 % NGS, 0.05 % gelatin and 50 mM glycine in PBT. After the blocking, slices were washed three times for 5 minutes with PBT. 250 µl of primary antibodies were incubated as described in chapter 5.6.1. Slices were washed six times with PBT for 5 minutes and 250 µl of respective secondary antibodies (1:500) were incubated for 2 hours at RT on a shaker. After six times washing with PBT for 5 minutes, sections were incubated with the DNA binding Draq5 (1:1000) and DAPI (1:5000) dyes for 30 minutes and 5 minutes, respectively. Lastly, sections were washed for 5 minutes with PBT at RT and were mounted on slides with Mowiol mounting medium containing 5 % of antifading reagent n-propyl-gallate (NPG). Immunofluorescence images were taken using the LSM 510 Meta confocal microscope.

4.4. Electrophysiology

To determine the effect of *Cyfip2* deletion on synaptic physiology, electrophysiological recordings were performed as described in master thesis work by Özer, 2015 (*Electrophysiological Analysis of Hippocampal Synaptic Properties in a Cyfip2 Conditional Knockout Mouse Model*). The methods used are briefly explained in following chapters.

4.4.1. Preparation of mouse brains for recordings

For the preparation of acute brain slices, mice were sacrificed by cervical dislocation and were decapitated. The brains were quickly removed and transferred into ice-cold sucrose-ACSF (artificial cerebrospinal fluid). The cerebellum and frontal third of the brain were cut off using a scalpel. The brain was cut along the midline into two hemispheres and a 10˚ cut (Bischofberger et al., 2006) was made on the dorsal side.

The hemispheres were then glued on the dorsal side onto the holder plate. Brains were placed in the vibratome tray containing slushy ice-cold sucrose-ACSF that was constantly gassed with carbogen (5 % CO_2/95 % O_2). 300 µm thick horizontal whole-brain slices were cut. After cutting, the slices were incubated in sucrose-ACSF at 35˚C for 15 min. The slices were then incubated in ACSF at room temperature, bubbled with carbogen, for at least 1 hour before recordings were made. The composition of solutions is described in chapter 5.2.7.

4.4.2. Electrophysiological setup

The electrophysiological experiments were carried out in a recording chamber with a patch-clamp setup. The brain slices were placed in a recording chamber mounted on a stable platform, which served as the specimen stage of the upright microscope. A slice holder, a C-shaped platinum wire with nylon threads, was placed on top of the slice for stabilization. The recording chamber was continuously perfused with carbogenized extracellular solution by a peristaltic pump. The tissue was visualized using an upright bright field microscope with a 10x magnification objective. The microscope was moved in x- and y-directions via an electric micromanipulator and was equipped with an infrared sensitive CCD camera to identify individual cells with a 60x water immersion objective.

An additional micromanipulator was used to move the recording electrode, which was connected to the headstage of the patch-clamp amplifier. For field potential recordings, a manipulator was used to move the stimulation electrode that was connected to a stimulation generator. Both recording and stimulation electrodes were equipped with chlorinated silver wires. The reference electrode, which was also placed in the recording chamber, consisted of an Ag/AgCl disc attached to a lead wire. The manipulators and the microscope were placed on a vibration isolating workstation to ensure stable measurements and were electrically shielded inside a Faraday cage. A vertical puller was used to pull the borosilicate glass pipettes for generating micropipettes. When filled with intracellular solution, recording and stimulation pipettes had resistances of 3-6 MΩ and 1-2 MΩ, respectively. A detailed list of equipment can be found in chapter 5.7.1.

4.4.3. Current-clamp mode

The current-clamp mode is used to measure changes in the membrane potential of the cell while the injected current is controlled by the amplifier. In this mode of recording, the membrane potential is free to vary in response to stimulation by current injection, neurotransmitters or pharmacological drugs.

4.4.3.1. Field recordings

All field recordings were performed using the current-clamp mode of the amplifier. For the field recordings, the recording and stimulation electrodes were filled with the extracellular solution (ACSF). The recording electrode was placed into the tissue, closely underneath the hippocampal CA1 pyramidal cell bodies layer in the *stratum radiatum* (the dendrites level), whereas the stimulation electrode was placed in the Schaffer collaterals. The stimulation electrode introduced currents to the axons at the Schaffer collaterals, depolarized the CA3 fibers and elicited action potentials. This in turn led to neurotransmitter release from the pre-synaptic membrane and generation of excitatory post-synaptic potentials (EPSPs) in the post-synaptic cells of the CA1 region. The currents injected through the stimulation electrode were kept constant and the changes in the sum of membrane potentials of the CA1 pyramidal neurons were recorded.

To dissect excitatory synaptic transmission, inhibitory inputs were blocked by adding 100 µM of the gamma-aminobutyric acid A ($GABA_A$) receptor channel blocker picrotoxin (PTX) to the extracellular solution. For the field recordings in the presence of PTX, a cut was made at the border of CA1 to CA3 in order to block epileptiform bursts in CA1 area.

4.4.3.1.1. Input-output recordings

The Schaffer collaterals were stimulated with pulses of 0.2 ms with current amplitudes of 10 µA, 15 µA, 20 µA, 25 µA and 30 µA. For each stimulation strength, the responses of 20 pulses were averaged to reduce the impact of electrical noise. Excitatory post-

synaptic potentials of the CA1 pyramidal neurons were measured against increasing electrical stimulus to analyze basal synaptic transmission.

4.4.3.1.2. Paired-pulse recordings

In order to analyze pre-synaptic neurotransmitter release probability, paired-pulse recordings were performed. Two adjacent stimulation pulses of 0.2 ms duration with an interval of 50 ms were introduced at the Schaffer collaterals. The responses from 20 trials were averaged to reduce the impact of electrical noise. The amplitude of the current introduced was determined as 50 % of the current giving the maximum EPSP, thus differed between experiments. The ratio of second to first EPSP was used to identify differences in pre-synaptic vesicle release probability.

4.4.4. Voltage-clamp mode

In voltage-clamp mode, currents flowing across the membrane are measured while the cell membrane potential is held at a defined value. In this mode, the amplifier compares the potential of the patched cell to the selected holding potential (-70 mV, if not stated otherwise). Whenever a difference occurs, the amplifier injects sufficient current to the system to keep the cell at the desired holding potential. Therefore, by documenting the current that is needed to compensate the changes in the potential of the membrane, the ion flow over the membrane is measured in an indirect way.

4.4.4.1. Patch-clamp recordings

The electrical properties of the cells were characterized by applying the whole-cell patch-clamp method (Hamill *et al.*, 1981). Briefly, after the recording pipette was filled with intracellular solution, it was moved towards the hippocampal CA1 pyramidal cell layer. Constant pressure was applied to the recording pipette via a tubing system, in order to prevent the plugging of the tip by tissue fragments. When the pipette was near the cell membrane, the overpressure was rapidly released and a mild negative pressure was applied. This led to formation of the cell-attached configuration characterized by the formation of a gigaseal. During this process, the holding potential

was changed from 0 mV to -60 mV. When the pipette resistance exceeded 1-2 GΩ, short pulses of suction were applied to disrupt the cell membrane and thus obtain the whole-cell configuration.

4.4.4.1.1. Miniature excitatory post-synaptic current recordings

To characterize action potential independent spontaneous vesicle release, miniature post-synaptic currents (mPSCs) were recorded. In order to block the generation of sodium driven action potentials (APs), pharmaceutical drugs were used in both extracellular and intracellular solutions. 0.5 µM of the Na^+ channel blocker tetrodotoxin (TTX) was added to the extracellular solutions that were perfused into the recording chamber. The intracellular solution used for mEPSC recordings contained 5 µM of the Na^+/Ca^{2+} exchanger blocker N-Ethyllidocaine bromide (QX-314).
To record miniature excitatory post-synaptic currents (mEPSCs), inhibitory currents were blocked by 100 µM PTX, which was added to the extracellular solution. To increase the frequency of mEPSCs 250 µM Trichlormethiazide (TCM), a drug that decreases the desensitization of post-synaptic AMPA receptors, was also added into the extracellular solution (ACSF).

4.4.5. Data analysis

For the analysis of mEPSCs, the program Mini Analysis (v6.0.7, Synaptosoft) was used. A low pass Butterworth digital filter was applied to the recorded traces to reduce electrical noise. The event threshold was set to 5 mV and ~150-300 events were analyzed for each cell. Averages and cumulative frequencies of event amplitudes and inter-event-intervals (IEIs, time between two adjacent events) were graphed.

Field EPSP (fEPSP) slopes were plotted against stimulation intensities to give input-output (I-O) curves for both genotypes. Paired-pulse ratios (PPRs) were measured as the ratio of the second fEPSP slope to the first one and were plotted against IEIs. Both I-O curves and PPRs were analyzed using Clampfit software.

4.5. Behavior

4.5.1. Open-field

A square open field with the dimensions 46 x 46 cm with ~60 lux light conditions was used for the behavioral testing. The field was divided into two virtual zones, center (square of 27x27 cm) and periphery (46 cm long and 9.5 cm wide corridor). Following 1 hour of habituation time after the transfer to the testing room, each mouse was placed in the center of an open field arena. The mice were then allowed to freely explore the field for 10 minutes, while videos were recorded using a black and white high sensitivity video camera system. The locomotion was analyzed using Stoelting ANY-maze software, while rearings were manually scored. Rearings of the mice, total distance, number of total entries, average time spent and average distance travelled in the center and periphery zones were recorded for investigating the anxiety and exploratory behavior of the mice.

4.5.2. Novel object recognition

In order to determine object memory of mice, a NOR test was performed. The test consisted of three phases; habituation, familiarization and test. In the habituation phase, the mouse was allowed to explore the empty open-field for 10 minutes (as described in chapter 4.5.1). 24 hours later, the mice were placed in the same open field as before with two identical objects placed at an equal distance from each other and close (5 cm) to the walls and were left to explore the objects for 10 minutes (familiarization phase). After the second phase, the mice were returned to their cages for 1 hour before the test phase. During this time, one of the objects was changed with a novel object with a different color and texture. The mice were then placed back in the open field to explore the two objects (known object and novel object) for 10 minutes. The time that the mouse spent on the novel object was used as an indicator of object memory.

4.5.3. Y-maze

A Y-maze with three identical closed arms (35 cm length x 5 cm width x 10 cm height) placed at 120° angle with ~60 lux light conditions was used for the behavioral testing of mice. After 1 hour of habituation time, each mouse was placed at the end of one arm facing the wall and left to explore the maze freely for 10 minutes. Videos were recorded during the exploration time with a black and white high sensitivity video camera system. The total number of entries, the three entries sequences into the arms (defined as spontaneous alternation, SPA, alternate arm return, AAR, and same arm return, SAR), the latency to exit the first arm and rearings were measured to assess the working memory, exploration and anxiety-like behaviors of the mice.

5. Material

5.1. Mouse lines

Line	Reference
Cyfip2-flox	derived from CyFIP2$^{tm1a.1(loxPs)(EUCOMM)Wtsi}$
Cyfip2-flox;Camk2a-Cre	Walter Witke
+/+ (C57BL/6NCtrl)	Charles River

5.2. Solutions and buffers

5.2.1. General solutions

Solution	Compound	Amount
PBS 10x (pH 7.4)	NaCl	1.5 M
	Na_2HPO_4	162 mM
	NaH_2PO_4	38 mM
TBS 10x	Tris-HCl (pH 7.4)	400 mM
	NaCl	1.5 M
4 % PFA (pH 7.4)	PBS 1x	500 ml
(500 ml, filtered)	Formaldehyde	20 g

5.2.2. Solutions for nucleic acid analysis

Solution	Compound	Amount
DNA extraction buffer	Tris-HCl (pH 7.4)	50 mM
	NaCl	100 mM
	EDTA	5 mM
	SDS (20 %)	1 %
	Proteinase K	0.5 µg/µl
DNA loading buffer	Sucrose	40 %
(100 ml)	SDS	0.5 %
	Bromophenol blue	0.25 %
	TE buffer	to 100 ml

TE buffer	Tris-HCl (pH 8.0)	100 mM
	EDTA	1 mM
TAE buffer 50x	Tris-HCl (pH 8.3)	2 M
	Acetic acid	57.1 ml
	EDTA (pH 8.0)	0.05 M
TENT buffer	Tris-HCl (pH 8.3)	20 mM
	EDTA	0.1 mM
	Tween-20	1 %
	Triton-X 100	0.2 %

5.2.3. Solutions for protein analysis

Solution	Compound	Amount
SDS loading buffer 5x	Tris-HCl (pH 6.8)	110 mM
	Glycerol	20 %
	SDS	3.8 %
	β-mercaptoethanol	8 %
	BPB	0.03 % (w/v)
Coomassie destaining solution	Methanol	40 %
	Acetic acid	10 %
Coomassie staining solution *(filtered)*	Methanol	50 %
	Acetic acid	10 %
	Coomassie Brilliant Blue R250	0.1 % (w/v)
ECL solution A *(100 ml)*	Tris-HCl (pH 8.5)	0.1 M
	Luminol stock	1 ml
	p-hydroxy-coumarin stock	0.44 ml
ECL solution B *(100 ml)*	Tris-HCl (pH 8.5)	10 ml
	H_2O_2 (30 %)	64 µl

Luminol stock solution	Luminol in DMSO	250 mM
NCP 10x (pH 8-8.4)	NaCl	1.47 M
	Tris	0.60 M
	Tween-20	0.5 %
p-hydroxy-coumarin stock solution	p-Coumaric Acid in DMSO	90 mM
Towbin transfer buffer	Tris	25 mM
	Glycine	192 mM
	Methanol	20 %
SDS running buffer 10x	Tris	0.25 M
	Glycine	1.92 M
	SDS (20 %)	1 %
Membrane blocking solution	NCP	1x
	Milk powder (non-fat) or BSA	5 %
Polyacrylamide resolving gel 15 % *(50 ml for 7 gels)*	Milli-Q H_2O	15.0 ml
	30 % Acrylamide (1:38)	25.0 ml
	2 M Tris/HCl pH 8.8	9.5 ml
	20 % SDS	250 µl
	10 % APS	320 µl
	TEMED	25 µl
Polyacrylamide resolving gel 10 % *(50 ml for 7 gels)*	Milli-Q H_2O	23.3 ml
	30 % Acrylamide (1:38)	16.7 ml
	2 M Tris/HCl pH 8.8	9.5 ml
	20 % SDS	250 µl
	10 % APS	320 µl
	TEMED	25 µl
Polyacrylamide stacking gel 3.8 % *(30 ml for 7 gels)*	Milli-Q H_2O	18.3 ml
	30 % Acrylamide (1:38)	3.9 ml

	20 % SDS	150 µl
	0.5 M Tris/HCl pH 6.8	7.5 ml
	10 % APS	180 µl
	TEMED^	14 µl
PHEM buffer 10x (pH 6.9)	PIPES	600 mM
	HEPES	250 mM
	EGTA	100 mM
	$MgCl_2$	20 mM
Lysis buffer	PHEM buffer	1x
	Triton-X 100	1 %

5.2.4. Solutions for pull-down

Solution	Compound	Amount
Buffer P	NaCl	150 mM
	HEPES	20 mM
	MgCl2	3.8 %
	Triton X-100	8 %

5.2.5. Solutions for Golgi stainings

Solution	Compound	Amount
Chrome alum solution *(for gelatine-coated slides)*	Gelatine	1.5 g
	$KCr(SO_4)_2$	0.35 g
	Milli-Q	500 ml

5.2.6. Solutions for immunofluorescence

Solution	Compound	Amount
PBT	PBS (pH 8.0)	1x
	Tween-20	0.1 %

PBT-Glycine (pH 7.5)	PBT	1x
	Glycine	200 mM
	NH4Cl	50 mM
Blocking solution	PBT	1x
	NGS	5 %
	Gelatine	0.05 %
	Glycine	50 mM
Unmasking solution	Mercaptoethanol	5 %
	SDS	1 %

5.2.7. Solutions for synaptosomal preparation

Solution	Compound	Amount
Homogenization buffer	Sucrose	0.32 M
	EDTA	1 mM
	BSA	1 mg/ml
	HEPES (pH 7.4)	5 mM
Krebs-Ringer buffer	NaCl	140 mM
	KCl	5mM
	Glucose	5 mM
	EDTA	1 mM
	HEPES (pH 7.4)	10 mM
Hepes-Krebs buffer	NaCl	147 mM
	KCl	3 mM
	Glucose	10 mM
	$MgSO_4$	2 mM
	$CaCl_2$	2mM
	HEPES (pH 7.4)	20 mM

5.2.8. Solutions for electrophysiological recordings

Solution	Compound	Amount
Artificial cerebrospinal fluid (ACSF) *pH 7.3-7.4 at room temperature* *after 15 min of carbogen gassing*	NaCl	126 mM
	KCl	2.5 mM
	$MgSO_4.7H_2O$	1.3 mM
	NaH_2PO_4	1.25 mM
	$NaHCO_3$	26 mM
	Glucose	10 mM
	$CaCl_2$	2 mM
Sucrose based artificial cerebrospinal fluid (Sucrose-ACSF) *pH 7.4 at room temperature after 15 min of carbogen gassing*	Sucrose	105 mM
	NaCl	60 mM
	KCl	2.5 mM
	$MgCl_2.6H_2O$	7 mM
	NaH_2PO_4	1.25 mM
	$NaHCO_3$	26 mM
	Glucose	10 mM
	$CaCl_2$	0.5 mM
Intracellular solution *pH 7.2 at room temperature* *(290 mOS/L)*	Cs-Gluconate	150 mM
	EGTA	0.2 mM
	HEPES	10 mM
	$MgCl_2$	2 mM
	Na-ATP	4 mM
	NaCl	8 mM
	QX-314	5 mM
Pharmacological drugs	Picrotoxin	100 µM
	TCM	250 µM
	Tetrodotoxin	0.5 µM

5.3 Commercial chemicals and reagents

5.3.1. Solid chemicals

Reagent	Manufacturer
Agarose	Biozym
Ammonium persulfate (APS)	Sigma-Aldrich
Bovine serum albumin (BSA)	Pan Biotech
Bromophenol blue	Bio-Rad
$CaCl_2 \cdot 2H_20$	Sigma-Aldrich
Coomassie Brilliant Blue R-250	AppliChem
CsCl	Sigma-Aldrich
CsOH	Sigma-Aldrich
D(+)-Glucose	Sigma-Aldrich
D(+)-Sucrose	VWR
EDTA	AppliChem
EGTA	Sigma-Aldrich
Gelatin	Merck
Gluconate	Sigma-Aldrich
HEPES	Sigma-Aldrich
Immobilized γ-Aminophenyl-m7GTP (C_{10}-spacer) beads	Jena Bioscience
KCl	Sigma-Aldrich
$KCr(SO_4)_2$	Merck
Luminol	Sigma-Aldrich
$MgCl_2 \cdot 6H_20$	AppliChem
$MgSO_4 \cdot 7H_20$	AppliChem
Milk powder (non-fat)	Roth
n-propyl-gallate (NPG)	Sigma-Aldrich
Na-ATP	Sigma
Na-ATP	Sigma-Aldrich
NaCl	Th. Geyer
NaH_2PO_4	AppliChem

$NAHCO_3$	AppliChem
NaN_3	Merck
Paraffin, low-melting	Merck
Picrotoxin	Sigma-Aldrich
PMSF	Sigma-Aldrich
Protease inhibitor cocktail tablets, Complete, EDTA-free	Roche
Proteinase K	Sigma-Aldrich
QX-314	Tocris
TCM	Sigma-Aldrich
Tetrodotoxin	Bio Trend
Tris base	Sigma-Aldrich

5.3.2. Liquid chemicals

Reagent	Manufacturer
β-mercaptoethanol	Sigma-Aldrich
Acetic acid glacial	VWR
Acrylamide (30 %)	Merck
Bradford reagent	Witke Lab
Dimethyl sulfoxide (DMSO)	Sigma-Aldrich
dNTPs	Promega
Entellan	Merck
Ethanol	Sigma-Aldrich
Ethidiumbromide (1 %)	VWR
FD Rapid GolgiStain kit	FD NeuroTechnologies
Glycine	Roth
Go-*Taq* polymerase	Promega
HEPES	Life Technologies
Hydrochloric acid (HCl) (37 %)	VWR

Isopropanol	VWR
Methanol	VWR
$MgCl_2$	Promega
Mowiol 4-88	Roth
Nitrogen	German-Cryo
Normal goat serum (NGS)	Vector Laboratories
PCR-flexi-buffer (5x)	Promega
Percoll	VWR
PIPES	Roth
RNaseOUT Recombinant Ribonuclease Inhibitor	Invitrogen
Sodium dodecyl sulfate (SDS)	AppliChem
TEMED	VWR
Triton-X 100	Roche
Tween-20	Sigma-Aldrich
Xylene	Roth

5.3.3. Markers

Reagent	Manufacturer
1 kb Plus DNA Ladder	Invitrogen
SeeBlue Plus2 Pre-Stained Standard	Invitrogen

5.4. Laboratory material

5.4.1. Plastic ware

Name	Manufacturer
22G needle	BD
Eppendorf tubes (1.5 ml, 2 ml)	Roth
Falcon tubes (15 ml, 50 ml)	Sarstedt
Latex gloves	Semperit
Pasteur pipettes	Sarstedt
PCR tubes	4titude

Pipette tips (20 µl, 200 µl, 1000 µl)	Sarstedt
Pipette tips (plugged)	Brand
Pipettes (5 ml, 10 ml, 20 ml, 50 ml)	Sarstedt
Snap-cap tubes	Falcon
Syringe	BD

5.4.2. Glass ware

Name	Manufacturer
Glass bottles (50 ml, 100 ml, 250 ml, 500 ml, 1000 ml)	Schott
Microscope slides	VWR
Pasteur pipettes	Brand

5.5. Oligonucleotides

Oligo (Witke lab archive #)	Sequence (5'-3' direction)
aCaMKII-1 (as) (#618)	ATG TGT CAG CGC CTA ACT CTG
C2EULoxP2-for (#718)	AGG GCC TTT GCA GGA TGG
C2EULoxP3-for (#703)	AGG AAG GCA TTT CCG AG
C2EULoxP3-rev2 (#753)	GGG GAG AGC TGG TAA GAG
MP80 (as) (#387)	CGC ATA ACC AGT GAA ACA GCA T
MP90 (s) (#386)	GGA CCT GGA TGC TGA CGA AG

5.6. Antibodies

5.6.1. Primary Antibodies

Unless stated otherwise, all antibodies were diluted in 5 % milk powder in 1x NCP.

Antigen	Host species	Dilution	Manufacturer
ABI1	Rabbit	WB 1:2000	Sigma-Aldrich
ABI2	Rabbit	WB 1:1000 (in 5 % BSA)	Abcam

Actin (C4)	Mouse	WB 1:5000	MP Biomedicals
APP	Rabbit	WB 1:20000	Abcam
BACE1	Rabbit	WB 1:1000 (in 5 % BSA)	Cell Signaling
CyFIP1 (Sra1)	Rabbit	WB 1:1000	Upstate
CyFIP2 (1C4)	Mouse	WB Hybridoma supernatant	Witke Lab
DNM1 (KG43)	Rabbit	WB 1:1000	Witke Lab
eIF4E	Rabbit	WB 1:1000 (in 5 % BSA)	Cell Signaling/NEB
FMRP	Rabbit	WB 1:500 (in 5 % BSA)	Cell Signaling
GFAP	Rabbit	WB 1:2000	Sigma-Aldrich
HSPC300	Mouse	WB Hybridoma supernatant	Stradal Lab
IBA1	Goat	WB 1:500	Novus Biologicals
IBA1	Rabbit	IF 1:750 (o/n, 4°C)	WAKO Chemicals
LC3B (D11)	Rabbit	WB 1:1000 (in 5 % BSA)	Cell Signaling/NEB
MBP	Rabbit	WB 1:1000	Abcam
MBP	Rabbit	IF 1:100 (o/n, 4°C)	Abcam
MUNC18	Mouse	WB 1:1000	BD Transduction
NAP1	Rabbit	WB 1:1000	Molecular Probes
NEUN	Mouse	WB 1:1000	Millipore
NRGN	Rabbit	IF 1:500 (o/n, 4°C)	Proteintech
p-TAU S-262&356	Mouse	WB 1:5000	Elan Pharmaceuticals
p-TAU S-396&404	Mouse	WB 1:500	Peter Davies
p21	Mouse	WB Hybridoma supernatant	Stradal Lab
S100β	Rabbit	IF 1:1000 (o/n, 4°C)	Abcam
SNAP25	Rabbit	WB 1:1000	Sigma-Aldrich

SQSTM1/p62	Rabbit	WB 1:10000	Abcam
Synapsin1	Rabbit	WB 1:1000	Millipore
Synapsin2A	Mouse	WB 1:500	BD Transduction
Synaptophysin	Mouse	WB 1:1000	Sigma-Aldrich
Synaptotagmin1	Rabbit	WB 1:1000	Synaptic Systems
Syntaxin1	Mouse	WB 1:1000	Synaptic Systems
TAU	Rabbit	WB 1:40000	DAKO
TH	Guinea Pig	IF 1:500	Synaptic Systems
VAMP2	Rabbit	WB 1:1000	Synaptic Systems
WAVE1/Scar	Rabbit	WB 1:1000	BD Transduction
WAVE2	Rabbit	WB 1:1000 (in 5 % BSA)	Cell Signaling
WAVE3	Rabbit	WB 1:1000	Cell Signaling

5.6.2. Secondary Antibodies

Antigen species	Conjugate	Host species	Dilution	Manufacturer
Chicken	Alexa-488	Goat	IF 1:500	Abcam
Goat	HRP	Rabbit	WB 1:2000	Pierce
Mouse	HRP	Goat	WB 1:2000	Jackson ImmunoResearch
Mouse	Alexa-488	Goat	IF 1:500	Life Technologies
Mouse	Alexa-555	Goat	IF 1:500	Life Technologies
Rabbit	HRP	Goat	WB 1:2000	Jackson ImmunoResearch
Rabbit	Alexa-555	Goat	IF 1:500	Life Technologies

5.6.3. Dyes

Dye	Dilution	Manufacturer
DAPI	1:5000	Sigma-Aldrich
Draq5	1:1000	Abcam

5.7. Equipment and Software

5.7.1. General Technical Equipment

Equipment	Manufacturer	Model/Version
16-bit data acquisition system	Axon Instruments	Digidata 1320A
50/60 Hz noise eliminator	Quest Scientific	Hum Bug
Agarose gel chamber	EMBL	M100
Amplifier	Axon Instruments	Axopatch 200
Amplifier	NPI Electronic	ELC-03XS
Analytical balance	Kern	ABS 120-4N
Balance	Sartorius	BP 2100 S
Brightfield microscope	Zeiss	Axioskop
Centrifuge	Beckmann	J2-21
Centrifuge	Heraeus	Megafuge 1.0R
Centrifuge	Eppendorf	5415 D
Centrifuge rotor	Beckmann	TLA100, TLA120.2, TLS55, JA-20
Confocal microscope	Carl Zeiss	LSM 510 Meta
Cooling centrifuge	Eppendorf	5417 R
Cryostat	Leica	CM3050 S
Digital monochrome camera	Bosch	LTC0355/50
Digitizer	HEKA Elektronik	LIH8+8
Electron microscope	Phillips	C100
Epoxy embedding medium	Fluka	Epon
Faraday cage	Custom built	
Fluorescence microscope	Keyence	Biorevo BZ-9000

Glass pipettes	Science Products	GB150-8P
Headstage	NPI Electronic	ELC 100M
Heating block	Grant	QBT
High voltage stimulus isolator	WPI	A360LA
Luminescent image analyzer	GE Healthcare	ImageQuant LAS 4000 mini
Magnetic stir plate	Heidolph	MR 3001 K
Manipulator controller	Luigs & Neumann	SM 1
Manipulator controller	Luigs & Neumann	SM 10
Micromanipulator	Luigs & Neumann	Mini 25
Micromanipulator	Luigs & Neumann	Mini 23
Micropipette puller	Narishige	PP-830
Microtome	Leica	RM2245
Monitor	Pieper	IM-M-1432-O-IQ
Oscilloscope	Tektronix	TDS 210
PAGE chamber	Hoefer	Mighty Small II (SE250/SE260)
PCR machine	Bio-Rad	T100
Peristaltic pump	Gilson	Minipuls 3
pH meter	InoLab	pH Level 2
Pipetboy	Brand	Accu-jet
Pipettes	Rainin	
Power supply (for agarose gels)	Pharmacia	GPS200/400
Power supply (for PAGE)	Bio-Rad	Power PAC 200/300
PVDF transfer membrane	Millipore	Immobilon-P
Razor blades for vibratome	Electron Microscopy Sciences	Feather double edge blade
Shaker	Heidolph	Duomax 1030
Slice chamber temperature controller	Luigs & Neumann	Temperaturcontroller VII
Slice cooling station	Julabo	F10

Spectrophotometer	Amersham Pharmacia	Ultrospec 3000 pro
Stage manipulator	Luigs & Neumann	Combi 25
Thermo-Shaker	Grant	HC24N
Tissue stirrer	IDL	RED 10
Ultracentrifuge	Beckmann Coulter	Optima MAX-XP
Ultratome	Leica	Ultracut
UV imager	Bio-Rad	Gel Doc XR+
Vibration isolation workstation	Newport	LW3036B-OPT
Vibratome (EM)	Leica	VT 10005
Vibratome (fixed tissue)	Leica	VT1200 S
Vibratome (unfixed tissue)	Thermo Scientific	Microm HM 650V
Video camera	Samsung	sc8-300
Vortex	Scientific Industries	Vortex-Genie 2
Water bath	GFL	1003
Water purifier	Millipore	Q-POD (Milli-Q)
Whatman paper	GE Healthcare	3 MM CHR

5.7.2. Equipment for Behavioral Experiments

Equipment	Description	Manufacturer
Open field	46 x 46 cm open box	Ugo Basile
Y-maze	Three 35 x 5 x 15 cm (L x W x H) arms placed at 120° angle	Ugo Basile

5.7.3. Software

Software	Manufacturer	Version
ANY-maze	Stoelting	5.33
Clampex	Axon Instruments	8.2.0.235
Clampfit	Axon Instruments	10.7
Igor Pro	WaveMetrics	6.01

Image J	NIH	1.45s
Mini Analysis	Synaptosoft	6.0.7
Multi Gauge	Fujifilm	V3.0
Prism	GraphPad	7.02

6. References

van Abeelen, J. H. F. (1970) 'Genetics of rearing behavior in mice', *Behavior Genetics*, 1, pp. 71–76. doi: 10.1007/BF01067372.

Abekhoukh, S. *et al.* (2017) 'New insights into the regulatory function of CYFIP1 in the context of WAVE- and FMRP-containing complexes', *DMM Disease Models and Mechanisms*, 10(4), pp. 463–474. doi: 10.1242/dmm.025809.

Aizenstein, H. J. *et al.* (2008) 'Frequent amyloid deposition without significant cognitive impairment among the elderly', *Archives of Neurology*, 65(11), pp. 1509–1517. doi: 10.1001/archneur.65.11.1509.

Allen, N. J. and Eroglu, C. (2017) 'Cell Biology of Astrocyte-Synapse Interactions', *Neuron*. Elsevier Inc., 96(3), pp. 697–708. doi: 10.1016/j.neuron.2017.09.056.

Aloisi, F. (2001) 'Immune function of microglia', *Glia*, 36(2), pp. 165–179. doi: 10.1002/glia.1106.

Amtul, Z. *et al.* (2002) 'A presenilin 1 mutation associated with familial frontotemporal dementia inhibits γ-secretase cleavage of APP and notch', *Neurobiology of Disease*, 9(2), pp. 269–273. doi: 10.1006/nbdi.2001.0473.

Andersen, P. *et al.* (2007) *The Hippocampus Book*. New York: Oxford University Press. doi: 10.1093/acprof:oso/9780195100273.001.0001.

Andersen, S. S. L. and Bi, G. Q. (2000) 'Axon formation: a molecular model for the generation of neuronal polarity.', *BioEssays*, 22(2), pp. 172–9. doi: 10.1002/(SICI)1521-1878(200002)22:2<172::AID-BIES8>3.0.CO;2-Q.

Attwell, D. and Laughlin, S. B. (2001) 'An energy budget for signaling in the grey matter of the brain', *Journal of Cerebral Blood Flow and Metabolism*, 21(10), pp. 1133–1145. doi: 10.1097/00004647-200110000-00001.

Bamburg, J. R. (1999) 'Proteins of the ADF/cofilin family: essential regulators of actin dynamics.', *Annual review of cell and developmental biology*, 15, pp. 185–230. doi: 10.1146/annurev.cellbio.15.1.185.

Bejanin, A. *et al.* (2017) 'Tau pathology and neurodegeneration contribute to cognitive impairment in Alzheimer's disease', *Brain*, 140(12), pp. 3286–3300. doi: 10.1093/brain/awx243.

Benson, D. L. *et al.* (1992) 'Contrasting patterns in the localization of glutamic acid decarboxylase and Ca2+ /calmodulin protein kinase gene expression in the rat centrat nervous system', *Neuroscience*, 46(4), pp. 825–849. doi: 10.1016/0306-

4522(92)90188-8.

Bento, C. F. *et al.* (2016) 'Mammalian Autophagy: How Does It Work?', *Annual Review of Biochemistry*, 85(1), pp. 685–713. doi: 10.1146/annurev-biochem-060815-014556.

Bernstein, B. W. and Bamburg, J. R. (2010) 'ADF/Cofilin: A functional node in cell biology', *Trends in Cell Biology*. Elsevier Ltd, 20(4), pp. 187–195. doi: 10.1016/j.tcb.2010.01.001.

Bevins, R. A. and Besheer, J. (2006) 'Object recognition in rats and mice: A one-trial non-matching-to-sample learning task to study "recognition memory"', *Nature Protocols*, 1(3), pp. 1306–1311. doi: 10.1038/nprot.2006.205.

Bischofberger, J. *et al.* (2006) 'Patch-clamp recording from mossy fiber terminals in hippocampal slices.', *Nature protocols*, 1(4), pp. 2075–81. doi: 10.1038/nprot.2006.312.

Bliss, T. V. P. and Lømo, T. (1973) 'Long-lasting potentiation of synaptic transmission in the dentate area of the anaesthetized rabbit following stimulation of the perforant path', *The Journal of Physiology*, 232(2), pp. 331–356. doi: 10.1113/jphysiol.1973.sp010273.

Bonaccorso, C. M. M. *et al.* (2015) 'Fragile X mental retardation protein (FMRP) interacting proteins exhibit different expression patterns during development', *International Journal of Developmental Neuroscience*, 42, pp. 15–23. doi: 10.1016/j.ijdevneu.2015.02.004.

Booker, S. A. and Vida, I. (2018) 'Morphological diversity and connectivity of hippocampal interneurons', *Cell and Tissue Research*. Cell and Tissue Research, 373(3), pp. 619–641. doi: 10.1007/s00441-018-2882-2.

De Boulle, K. *et al.* (1993) 'A point mutation in the FMR-1 gene associated with fragile X mental retardation', *Nature Genetics*, 3(1), pp. 31–35. doi: 10.1038/ng0193-31.

Bozdagi, O. *et al.* (2012) 'Haploinsufficiency of Cyfip1 produces fragile X-like phenotypes in mice', *PLoS ONE*, 7(8). doi: 10.1371/journal.pone.0042422.

Braak, H. and Del Tredici, K. (2015) 'The preclinical phase of the pathological process underlying sporadic Alzheimer's disease', *Brain*, 138(10), pp. 2814–2833. doi: 10.1093/brain/awv236.

Bradford, M. (1976) 'A Rapid and Sensitive Method for the Quantitation of Microgram Quantities of Protein Utilizing the Principle of Protein-Dye Binding', *Analytical*

Biochemistry, 72(1–2), pp. 248–254. doi: 10.1006/abio.1976.9999.

Bradke, F. and Dotti, C. C. (1999) 'The role of local actin instability in axon formation', *Science*, 283(5409), pp. 1931–1934. doi: 10.1126/science.283.5409.1931.

Bradl, M. and Lassmann, H. (2010) 'Oligodendrocytes: Biology and pathology', *Acta Neuropathologica*, 119(1), pp. 37–53. doi: 10.1007/s00401-009-0601-5.

Burgin, K. E. *et al.* (1990) 'In situ hybridization histochemistry of Ca2+/calmodulin-dependent protein kinase in developing rat brain.', *The Journal of Neuroscience*, 10(6), pp. 1788–98.

Bushong, E. A. *et al.* (2002) 'Protoplasmic astrocytes in CA1 stratum radiatum occupy separate anatomical domains', *Journal of Neuroscience*, 22(1), pp. 183–192.

Campellone, K. G. and Welch, M. D. (2010) 'A nucleator arms race: cellular control of actin assembly.', *Nature reviews. Molecular cell biology*, 11(4), pp. 237–251. doi: 10.1038/nrm2867.

Carter, M. and Shieh, J. C. (2010) *Guide to Research Techniques in Neuroscience*. doi: 10.1016/B978-0-12-374849-2.00016-1.

Chang, Y. C., Cole, T. B. and Costa, L. G. (2017) 'Behavioral phenotyping for autism spectrum disorders in mice', *Current Protocols in Toxicology*, 2017(May), pp. 1–21. doi: 10.1002/cptx.19.

Chen, B. *et al.* (2014) 'The WAVE Regulatory Complex Links Diverse Receptors to the Actin Cytoskeleton', *Cell*, 156(1–2), pp. 195–207. doi: 10.1016/j.cell.2013.11.048.

Chen, Z. *et al.* (2010) 'Structure and control of the actin regulatory WAVE complex.', *Nature*. Nature Publishing Group, 468(7323), pp. 533–8. doi: 10.1038/nature09623.

Chhabra, E. S. and Higgs, H. N. (2007) 'The many faces of actin: matching assembly factors with cellular structures.', *Nature cell biology*. Nature Publishing Group, 9(10), pp. 1110–21. doi: 10.1038/ncb1007-1110.

Cioni, J. M. *et al.* (2018) 'Axon-Axon Interactions Regulate Topographic Optic Tract Sorting via CYFIP2-Dependent WAVE Complex Function', *Neuron*. Elsevier Inc., 97(5), pp. 1078-1093.e6. doi: 10.1016/j.neuron.2018.01.027.

Crawley, J. N. and Paylor, R. (1997) 'A proposed test battery and constellations of specific behavioral paradigms to investigate the behavioral phenotypes of transgenic and knockout mice.', *Hormones and behavior*, 31(3), pp. 197–211. doi:

10.1006/hbeh.1997.1382.

Crous-Bou, M. *et al.* (2017) 'Alzheimer's disease prevention: From risk factors to early intervention', *Alzheimer's Research and Therapy*. Alzheimer's Research & Therapy, 9(1), pp. 1–9. doi: 10.1186/s13195-017-0297-z.

D'Hooge, R. and De Deyn, P. P. (2001) 'Applications of the Morris water maze in the study of learning and memory.', *Brain research. Brain research reviews*, 36(1), pp. 60–90. doi: 10.1038/nrd3093.

Davenport, E. C. *et al.* (2019) 'Autism and Schizophrenia-Associated CYFIP1 Regulates the Balance of Synaptic Excitation and Inhibition', *Cell Reports*. Elsevier B.V., 26(8), pp. 2037-2051.e6. doi: 10.1016/j.celrep.2019.01.092.

Denker, A. and Rizzoli, S. O. (2010) 'Synaptic vesicle pools: an update', *Frontiers in Synaptic Neuroscience*, 2(OCT), p. 135. doi: 10.3389/fnsyn.2010.00135.

Derivery, E. *et al.* (2009) 'The Wave complex is intrinsically inactive', *Cell Motility and the Cytoskeleton*, 66(10), pp. 777–90. doi: 10.1002/cm.20342.

Dermaut, B. *et al.* (2004) 'A Novel Presenilin 1 Mutation Associated with Pick's Disease but Not β-Amyloid Plaques', *Annals of Neurology*, 55(5), pp. 617–626. doi: 10.1002/ana.20083.

Didry, D., Carlier, M. F. and Pantaloni, D. (1998) 'Synergy between actin depolymerizing factor/cofilin and profilin in increasing actin filament turnover', *Journal of Biological Chemistry*, 273(40), pp. 25602–25611. doi: 10.1074/jbc.273.40.25602.

Dillon, C. and Goda, Y. (2005) 'The actin cytoskeleton: integrating form and function at the synapse.', *Annual Review of Neuroscience*. Annual Reviews, 28(1), pp. 25–55. doi: 10.1146/annurev.neuro.28.061604.135757.

Domínguez-Iturza, N. *et al.* (2019) 'The autism- and schizophrenia-associated protein CYFIP1 regulates bilateral brain connectivity and behaviour', *Nature Communications*, 10(1), pp. 1–13. doi: 10.1038/s41467-019-11203-y.

Dominguez, R. and Holmes, K. C. (2011) 'Actin structure and function.', *Annual review of biophysics*, 40, pp. 169–86. doi: 10.1146/annurev-biophys-042910-155359.

Dubielecka, P. M. *et al.* (2011) 'Essential role for Abi1 in embryonic survival and WAVE2 complex integrity', *Proceedings of the National Academy of Sciences of the United States of America*, 108(17), pp. 7022–7027. doi: 10.1073/pnas.1016811108.

Edbauer, D. *et al.* (2003) 'Reconstitution of γ-secretase activity', *Nature Cell Biology*, 5(5), pp. 486–488. doi: 10.1038/ncb960.

Eden, S. *et al.* (2002) 'Mechanism of regulation of WAVE1-induced actin nucleation by Rac1 and Nck.', *Nature*, 418(6899), pp. 790–793. doi: 10.1038/nature00859.

Elder, G. A., Gama Sosa, M. A. and De Gasperi, R. (2010) 'Transgenic mouse models of Alzheimer's disease.', *The Mount Sinai Journal of Medicine*, 77(1), pp. 69–81. doi: 10.1002/msj.20159.

Esquerda-Canals, G. *et al.* (2017) 'Mouse Models of Alzheimer's Disease', *Journal of Alzheimer's Disease*, 57(4), pp. 1171–1183. doi: 10.3233/JAD-170045.

Fakhoury, M. (2017) 'Microglia and astrocytes in Alzheimer's disease: implications for therapy', *Current Neuropharmacology*, 15, pp. 508–518. doi: 10.2174/1570159x15666170720095240.

Games, D. *et al.* (1995) 'Alzheimer-type neuropathology in transgenic mice overexpressing V717F β-amyloid precursor protein', *Nature*, 373(6514), pp. 523–527. doi: 10.1038/373523a0.

Goley, E. D. and Welch, M. D. (2006) 'The ARP2/3 complex: an actin nucleator comes of age.', *Nature Reviews*, 7(10), pp. 713–726. doi: 10.1038/nrm2026.

Gordon, R. E. (2014) 'Electron Microscopy: A Brief History and Review of Current Clinical Application', in, pp. 119–135. doi: 10.1007/978-1-4939-1050-2_7.

Graus-Porta, D. *et al.* (2001) 'β1-Class integrins regulate the development of laminae and folia in the cerebral and cerebellar cortex', *Neuron*, 31(3), pp. 367–379. doi: 10.1016/S0896-6273(01)00374-9.

Hamill, O. P. *et al.* (1981) 'Improved patch-clamp techniques for high-resolution current recording from cells and cell-free membrane patches', *Pflügers Archiv European Journal of Physiology*, 391(2), pp. 85–100. doi: 10.1007/BF00656997.

Han, K. *et al.* (2015) 'Fragile X-like behaviors and abnormal cortical dendritic spines in Cytoplasmic FMR1-interacting protein 2-mutant mice', *Human Molecular Genetics*, 24(7), pp. 1813–1823. doi: 10.1093/hmg/ddu595.

Hardy, J. and Higgins, G. (1992) 'Alzheimer's disease: the amyloid cascade hypothesis', *Science*, 256(5054), pp. 184–185. doi: 10.1126/science.1566067.

Hernandez, D. *et al.* (2012) 'Regulation of Presynaptic Neurotransmission by

Macroautophagy', *Neuron*, 74(2), pp. 277–284. doi: 10.1016/j.neuron.2012.02.020.

Herring, B. E. and Nicoll, R. A. (2016) 'Long-Term Potentiation: From CaMKII to AMPA Receptor Trafficking', *Annual Review of Physiology*, 78(1), pp. 351–365. doi: 10.1146/annurev-physiol-021014-071753.

Hippius, H. and Neundörfer, G. (2003) 'The discovery of Alzheimer's disease.', *Dialogues in clinical neuroscience*, 5(1), pp. 101–8.

Hirokawa, N. (1989) 'The cytoskeletal architecture of the presynaptic terminal and molecular structure of synapsin 1', *The Journal of Cell Biology*, 108(1), pp. 111–126. doi: 10.1083/jcb.108.1.111.

Hoeffer, C. A. *et al.* (2012) 'Altered mTOR signaling and enhanced CYFIP2 expression levels in subjects with fragile X syndrome', *Genes, Brain and Behavior*, 11(3), pp. 332–341. doi: 10.1111/j.1601-183X.2012.00768.x.

Holcomb, L. *et al.* (1998) 'Accelerated Alzheimer-type phenotype in transgenic mice carrying both mutant amyloid precursor protein and presenilin 1 transgenes.', *Nature Medicine*, 4(1), pp. 97–100.

Holmes, K. C. *et al.* (1990) 'Atomic model of the actin filament.', *Nature*, 347(6288), pp. 44–9. doi: 10.1038/347044a0.

Hotulainen, P. *et al.* (2009) 'Defning mechanisms of actin polymerization and depolymerization during Dendritic spine morphogenesis', *Journal of Cell Biology*, 185(2), pp. 323–339. doi: 10.1083/jcb.200809046.

Hotulainen, P. and Hoogenraad, C. C. (2010) 'Actin in dendritic spines: Connecting dynamics to function', *Journal of Cell Biology*, 189(4), pp. 619–629. doi: 10.1083/jcb.201003008.

Hsia, A. Y., Malenka, R. C. and Nicoll, R. A. (1998) 'Development of excitatory circuitry in the hippocampus.', *Journal of Neurophysiology*, 79(4), pp. 2013–2024. doi: 10.1152/jn.1998.79.4.2013.

Hsiao, K. *et al.* (2016) 'Cyfip1 Regulates Presynaptic Activity during Development', *The Journal of Neuroscience*, 36(5), pp. 1564–1576. doi: 10.1523/JNEUROSCI.0511-15.2016.

Hughes, R. N. (2004) 'The value of spontaneous alternation behavior (SAB) as a test of retention in pharmacological investigations of memory.', *Neuroscience and Biobehavioral Reviews*, 28(5), pp. 497–505. doi: 10.1016/j.neubiorev.2004.06.006.

Ingelsson, M. *et al.* (2004) 'Early Aβ accumulation and progressive synaptic loss, gliosis, and tangle formation in AD brain', *Neurology*, 62(6), pp. 925–931. doi: 10.1212/01.WNL.0000115115.98960.37.

Innocenti, M. *et al.* (2004) 'Abi1 is essential for the formation and activation of a WAVE2 signalling complex.', *Nature cell biology*, 6(4), pp. 319–327. doi: 10.1038/ncb1105.

Jang, E. *et al.* (2013) 'Phenotypic Polarization of Activated Astrocytes: The Critical Role of Lipocalin-2 in the Classical Inflammatory Activation of Astrocytes', *The Journal of Immunology*, 191(10), pp. 5204–5219. doi: 10.4049/jimmunol.1301637.

Kandel, E. R. *et al.* (2012) *Principles of Neural Science*. 5th edn. McGraw-Hill.

Kang, H. W. *et al.* (2017) 'Comprehensive Review of Golgi Staining Methods for Nervous Tissue', *Applied Microscopy*, 47(2), pp. 63–69. doi: 10.9729/AM.2017.47.2.63.

Kasza, Á. *et al.* (2017) 'Studies for improving a rat model of Alzheimer's disease: ICV administration of well-characterized β-amyloid 1-42 oligomers induce dysfunction in spatial memory', *Molecules*, 22(11). doi: 10.3390/molecules22112007.

Kazdoba, T. M. *et al.* (2014) 'Modeling fragile X syndrome in the Fmr1 knockout mouse', *Intractable and Rare Diseases Research*, 3(4), pp. 118–133. doi: 10.5582/irdr.2014.01024.

Kirkpatrick, S. L. *et al.* (2017) 'Cytoplasmic FMR1-Interacting Protein 2 Is a Major Genetic Factor Underlying Binge Eating', *Biological Psychiatry*, 81(9), pp. 757–769. doi: 10.1016/j.biopsych.2016.10.021.

Kobayashi, K. *et al.* (1998) 'p140Sra-1 (specifically Rac1-associated protein) is a novel specific target for Rac1 small GTPase', *Journal of Biological Chemistry*, 273(1), pp. 291–295. doi: 10.1074/jbc.273.1.291.

Koffie, R. M., Hyman, B. T. and Spires-Jones, T. L. (2011) 'Alzheimer's disease: synapses gone cold', *Molecular Neurodegeneration*, 6(1), p. 63. doi: 10.1186/1750-1326-6-63.

Kron, S. J. *et al.* (1992) 'Yeast actin filaments display ATP-dependent sliding movement over surfaces coated with rabbit muscle myosin.', *Proceedings of the National Academy of Sciences of the United States of America*, 89(10), pp. 4466–70.

Krucker, T., Siggins, G. R. and Halpain, S. (2000) 'Dynamic actin filaments are required for stable long-term potentiation (LTP) in area CA1 of the hippocampus', *Proceedings of the National Academy of Sciences of the United States of America*, 97(12), pp. 6856–6861. doi: 10.1073/pnas.100139797.

Kumar, V. *et al.* (2013) 'C57BL/6N Mutation in Cytoplasmic FMRP interacting protein 2 Regulates Cocaine Response', *Science*, 342(6165), pp. 1508–1512. doi: 10.1126/science.1245503.

Lai, K. O. and Ip, N. Y. (2013) 'Structural plasticity of dendritic spines: The underlying mechanisms and its dysregulation in brain disorders', *Biochimica et Biophysica Acta*, 1832(12), pp. 2257–2263. doi: 10.1016/j.bbadis.2013.08.012.

Lane, C. A., Hardy, J. and Schott, J. M. (2018) 'Alzheimer's disease.', *European Journal of Neurology*, 25(1), pp. 59–70. doi: 10.1111/ene.13439.

Ledesma, M. D. and Dotti, C. G. (2003) 'Membrane and cytoskeleton dynamics during axonal elongation and stabilization', *International Review of Cytology*, 227, pp. 183–219. doi: 10.1016/S0074-7696(03)01010-6.

Lee, Y. *et al.* (2017) 'Phosphorylation of CYFIP2, a component of the WAVE-regulatory complex, regulates dendritic spine density and neurite outgrowth in cultured hippocampal neurons potentially by affecting the complex assembly', *NeuroReport*, 28(12), pp. 749–754. doi: 10.1097/WNR.0000000000000838.

Leger, M. *et al.* (2013) 'Object recognition test in mice', *Nature Protocols*, 8(12), pp. 2531–2537. doi: 10.1038/nprot.2013.155.

Levanon, E. Y. *et al.* (2004) 'Systematic identification of abundant A-to-I editing sites in the human transcriptome', *Nature Biotechnology*, 22(8), pp. 1001–1005. doi: 10.1038/nbt996.

Liu, W. J. *et al.* (2016) 'P62 Links the Autophagy Pathway and the Ubiqutin-Proteasome System Upon Ubiquitinated Protein Degradation', *Cellular and Molecular Biology Letters*, 21(1), pp. 1–14. doi: 10.1186/s11658-016-0031-z.

Liu, X.-B. and Murray, K. D. (2012) 'Neuronal excitability and calcium/calmodulin-dependent protein kinase type II: location, location, location.', *Epilepsia*, 53 Suppl 1, pp. 45–52. doi: 10.1111/j.1528-1167.2012.03474.x.

Livingston, G. *et al.* (2017) 'Dementia prevention, intervention, and care', *The Lancet*, 390(10113), pp. 2673–2734. doi: 10.1016/S0140-6736(17)31363-6.

Lodish, H. *et al.* (2000) 'The Dynamics of Actin Assembly', in *The Dynamics of Actin Assembly*. 4th edn, p. Molecular Cell Biology. doi: 10.1017/CBO9781107415324.004.

Machesky, L. M. (1994) 'Purification of a cortical complex containing two unconventional actins from Acanthamoeba by affinity chromatography on profilin-agarose', *The Journal of Cell Biology*, 127(1), pp. 107–115. doi: 10.1083/jcb.127.1.107.

Manns, J. M. (2011) 'SDS-polyacrylamide gel electrophoresis (SDS-PAGE) of proteins', *Current Protocols in Microbiology*, (SUPPL. 22), pp. 1–13. doi: 10.1002/9780471729259.mca03ms22.

Marra, V. *et al.* (2012) 'A Preferentially Segregated Recycling Vesicle Pool of Limited Size Supports Neurotransmission in Native Central Synapses', *Neuron*, 76(3), pp. 579–589. doi: 10.1016/j.neuron.2012.08.042.

Martínez-Cerdeño, V. (2017) 'Dendrite and spine modifications in autism and related neurodevelopmental disorders in patients and animal models', *Developmental Neurobiology*, 77(4), pp. 393–404. doi: 10.1002/dneu.22417.

Massimi, M. (2008) *Characterization of Profilin2 Complexes in the Mouse*. Rheinische Friedrich-Wilhelms-Universität Bonn.

Matus, A. (2000) 'Actin-based plasticity in dendritic spines', *Science*, 290(5492), pp. 754–758. doi: 10.1126/science.290.5492.754.

Michalski, J. P. and Kothary, R. (2015) 'Oligodendrocytes in a nutshell', *Frontiers in Cellular Neuroscience*, 9, pp. 1–11. doi: 10.3389/fncel.2015.00340.

Miermans, C. A. *et al.* (2017) 'Biophysical model of the role of actin remodeling on dendritic spine morphology', *PLoS ONE*, 12(2), pp. 1–14. doi: 10.1371/journal.pone.0170113.

Minichiello, L. *et al.* (1999) 'Essential Role for TrkB Receptors in Hippocampus-Mediated Learning', *Neuron*, 24(2), pp. 401–414. doi: 10.1016/S0896-6273(00)80853-3.

Morales, M., Colicos, M. A. and Goda, Y. (2000) 'Actin-dependent regulation of neurotransmitter release at central synapses', *Neuron*, 27(3), pp. 539–550. doi: 10.1016/S0896-6273(00)00064-7.

Morris, G. M. (1981) 'Spatial Localization Does Not Require Local Cues', *Learning and Motivation*, 260, pp. 239–260.

Mullane, K. and Williams, M. (2019) 'Preclinical Models of Alzheimer's Disease: Relevance and Translational Validity', *Current Protocols in Pharmacology*, 84(1), pp. 1–28. doi: 10.1002/cpph.57.

Müller, U. C., Deller, T. and Korte, M. (2017) 'Not just amyloid: Physiological functions of the amyloid precursor protein family', *Nature Reviews Neuroscience*, 18(5), pp. 281–298. doi: 10.1038/nrn.2017.29.

Mullins, R. D., Heuser, J. a and Pollard, T. D. (1998) 'The interaction of Arp2/3 complex with actin: nucleation, high affinity pointed end capping, and formation of branching networks of filaments.', *Proceedings of the National Academy of Sciences of the United States of America*, 95(11), pp. 6181–6186. doi: 10.1073/pnas.95.11.6181.

Murphy-Royal, C. *et al.* (2017) 'Astroglial glutamate transporters in the brain: Regulating neurotransmitter homeostasis and synaptic transmission', *Journal of Neuroscience Research*, 95(11), pp. 2140–2151. doi: 10.1002/jnr.24029.

Napoli, I. *et al.* (2008) 'The Fragile X Syndrome Protein Represses Activity-Dependent Translation through CYFIP1, a New 4E-BP', *Cell*, 134(6), pp. 1042–1054. doi: 10.1016/j.cell.2008.07.031.

Neher, E. and Sakmann, B. (1976) 'Single-channel currents recorded from membrane of denervated frog muscle fibres.', *Nature*, 260(5554), pp. 799–802. doi: 10.1038/260799a0.

Nimchinsky, E. A., Sabatini, B. L. and Svoboda, K. (2002) 'Structure and Function of Dendritic Spines', *Annual Review of Physiology*, 64(1), pp. 313–353. doi: 10.1146/annurev.physiol.64.081501.160008.

Nishimura, Y. *et al.* (2007) 'Genome-wide expression profiling of lymphoblastoid cell lines distinguishes different forms of autism and reveals shared pathways', *Human Molecular Genetics*, 16(14), pp. 1682–1698. doi: 10.1093/hmg/ddm116.

Noroozi, R. *et al.* (2018) 'Cytoplasmic FMRP interacting protein 1/2 (CYFIP1/2) expression analysis in autism', *Metabolic Brain Disease*, 33(4), pp. 1353–1358. doi: 10.1007/s11011-018-0249-8.

Nowicki, S. T. *et al.* (2007) 'The Prader-Willi Phenotype of Fragile X Syndrome', *Journal of Developmental & Behavioral Pediatrics*, 28(2), pp. 133–138. doi: 10.1097/01.DBP.0000267563.18952.c9.

O'Brien, R. J. and Wong, P. C. (2011) 'Amyloid precursor protein processing and

Alzheimer's disease.', *Annual review of neuroscience*, 34(1), pp. 185–204. doi: 10.1146/annurev-neuro-061010-113613.

Olton, D. S. and Samuelson, R. J. (1976) 'Journal of Experimental Psychology : Animal Behavior Processes Remembrance of Places Passed : Spatial Memory in Rats', *J Exp Psychol: Anim Behav Process*, 2(2), pp. 97–116.

Pak, C. W., Flynn, K. C. and Bamburg, J. R. (2008) 'Actin-binding proteins take the reins in growth cones.', *Nature reviews. Neuroscience*, 9(2), pp. 136–147. doi: 10.1038/nrn2236.

Pantaloni, D., Carlier, M. F. and Coue, M. (1984) 'The critical concentration of actin in the presence of ATP increases with the number concentration of filaments and approaches the critical concentration of actin-ADP', *Journal of Biological Chemistry*, 259(10), pp. 6274–6283.

Parra, P., Gulyás, A. I. and Miles, R. (1998) 'How many subtypes of inhibitory cells in the hippocampus?', *Neuron*, 20(5), pp. 983–993. doi: 10.1016/S0896-6273(00)80479-1.

Pathania, M. *et al.* (2014) 'The autism and schizophrenia associated gene CYFIP1 is critical for the maintenance of dendritic complexity and the stabilization of mature spines.', *Translational Psychiatry*, 4, p. e374. doi: 10.1038/tp.2014.16.

Pelkey, K. A. *et al.* (2017) 'Hippocampal gabaergic inhibitory interneurons', *Physiological Reviews*, 97(4), pp. 1619–1747. doi: 10.1152/physrev.00007.2017.

Pereda, A. E. (2014) 'Electrical synapses and their functional interactions with chemical synapses', *Nature Reviews Neuroscience*, 15(4), pp. 250–263. doi: 10.1038/nrn3708.

Perry, V. H. and Teeling, J. (2013) 'Microglia and macrophages of the central nervous system: The contribution of microglia priming and systemic inflammation to chronic neurodegeneration', *Seminars in Immunopathology*, 35(5), pp. 601–612. doi: 10.1007/s00281-013-0382-8.

Peters, A. and Kaiserman-Abramof, I. R. (1970) 'The small pyramidal neuron of the rat cerebral cortex. The perikaryon, dendrites and spines.', *The American Journal of Anatomy*, 127(4), pp. 321–55. doi: 10.1002/aja.1001270402.

Pilo Boyl, P. *et al.* (2007) 'Profilin2 contributes to synaptic vesicle exocytosis, neuronal excitability, and novelty-seeking behavior.', *The EMBO journal*, 26(12), pp. 2991–3002. doi: 10.1038/sj.emboj.7601737.

Pittman, A. J., Gaynes, J. a. and Chien, C.-B. B. (2010) 'Nev (cyfip2) is required for retinal lamination and axon guidance in the zebrafish retinotectal system', *Developmental Biology*, 344(2), pp. 784–794. doi: 10.1016/j.ydbio.2010.05.512.

Pollard, T. D. (2016) 'Actin and Actin-Binding Proteins.', *Cold Spring Harbor perspectives in biology*. Cold Spring Harbor Laboratory Press, 8(8). doi: 10.1101/cshperspect.a018226.

Price, J. C. *et al.* (2010) 'Analysis of proteome dynamics in the mouse brain', *Proceedings of the National Academy of Sciences*, 107(32), pp. 14508–14513. doi: 10.1073/pnas.1006551107.

Qurashi, A. *et al.* (2007) 'HSPC300 and its role in neuronal connectivity', *Neural Development*, 2(1), pp. 1–13. doi: 10.1186/1749-8104-2-18.

Raux, G. *et al.* (2000) 'Dementia with prominent frontotemporal features associated with L113P presenilin 1 mutation', *Neurology*, 55(10), pp. 1577–1578.

Reimer, R. J. *et al.* (2017) 'Bassoon Controls Presynaptic Autophagy through Atg5', *Neuron*, 93(4), pp. 897-913.e7. doi: 10.1016/j.neuron.2017.01.026.

dos Remedios, C. G. *et al.* (2003) 'Actin binding proteins: regulation of cytoskeletal microfilaments.', *Physiological Reviews*, 83(2), pp. 433–473. doi: 10.1152/physrev.00026.2002.

Rizo, J. and Südhof, T. C. (2002) 'SNAREs and Munc18 in synaptic vesicle fusion', *Nature Reviews Neuroscience*, 3(8), pp. 641–653. doi: 10.1038/nrn898.

Romero, S. *et al.* (2004) 'Formin is a processive motor that requires profilin to accelerate actin assembly and associated ATP hydrolysis', *Cell*, 119(3), pp. 419–429. doi: 10.1016/j.cell.2004.09.039.

Rottner, K., Hänisch, J. and Campellone, K. G. (2010) 'WASH, WHAMM and JMY: Regulation of Arp2/3 complex and beyond', *Trends in Cell Biology*, 20(11), pp. 650–661. doi: 10.1016/j.tcb.2010.08.014.

Rotty, J. D., Wu, C. and Bear, J. E. (2013) 'New insights into the regulation and cellular functions of the ARP2/3 complex.', *Nature Reviews*. Nature Publishing Group, 14(1), pp. 7–12. doi: 10.1038/nrm3492.

De Rubeis, S. *et al.* (2013) 'CYFIP1 Coordinates mRNA Translation and Cytoskeleton Remodeling to Ensure Proper Dendritic Spine Formation', *Neuron*, 79(6), pp. 1169–1182. doi: 10.1016/j.neuron.2013.06.039.

Saller, E. *et al.* (1999) 'Increased apoptosis induction by 121F mutant p53.', *The EMBO journal*, 18(16), pp. 4424–37. doi: 10.1093/emboj/18.16.4424.

San Miguel-Ruiz, J. E. and Letourneau, P. C. (2014) 'The role of Arp2/3 in growth cone actin dynamics and guidance is substrate dependent.', *The Journal of neuroscience : the official journal of the Society for Neuroscience*, 34(17), pp. 5895–908. doi: 10.1523/JNEUROSCI.0672-14.2014.

Schenck, A. *et al.* (2001) 'A highly conserved protein family interacting with the fragile X mental retardation protein (FMRP) and displaying selective interactions with FMRP-related proteins FXR1P and FXR2P.', *Proceedings of the National Academy of Sciences*, 98(15), pp. 8844–9. doi: 10.1073/pnas.151231598.

Schenck, A. *et al.* (2003) *CYFIP/Sra-1 Controls Neuronal Connectivity in Drosophila and Links the Rac1 GTPase Pathway to the Fragile X Protein*, *Neuron*.

Shen, J. and Kelleher, R. J. (2007) 'The presenilin hypothesis of Alzheimer's disease: Evidence for a loss-of-function pathogenic mechanism', *Proceedings of the National Academy of Sciences of the United States of America*, 104(2), pp. 403–409. doi: 10.1073/pnas.0608332104.

Simons, M. and Trajkovic, K. (2006) 'Neuron-glia communication in the control of oligodencrocyte function and myelin biogenesis', *Journal of Cell Science*, 119(21), pp. 4381–4389. doi: 10.1242/jcs.03242.

Singec, I. *et al.* (2004) 'Neurogranin is expressed by principal cells but not interneurons in the rodent and monkey neocortex and hippocampus', *Journal of Comparative Neurology*, 479(1), pp. 30–42. doi: 10.1002/cne.20302.
Sofroniew, M. V. and Vinters, H. V. (2010) 'Astrocytes: Biology and pathology', *Acta Neuropathologica*, 119(1), pp. 7–35. doi: 10.1007/s00401-009-0619-8.

Spence, E. F. *et al.* (2016) 'The Arp2/3 complex is essential for distinct stages of spine synapse maturation, including synapse unsilencing', *Journal of Neuroscience*, 36(37), pp. 9696–9709. doi: 10.1523/JNEUROSCI.0876-16.2016.

Spires-Jones, T. L. *et al.* (2009) 'Passive immunotherapy rapidly increases structural plasticity in a mouse model of Alzheimer disease', *Neurobiology of Disease*, 33(2), pp. 213–220. doi: 10.1016/j.nbd.2008.10.011.

Steffen, A. *et al.* (2004) 'Sra-1 and Nap1 link Rac to actin assembly driving lamellipodia formation.', *The EMBO journal*, 23(4), pp. 749–59. doi: 10.1038/sj.emboj.7600084.

Stellwagen, N. C. (2009) 'Electrophoresis of DNA in agarose gels, polyacrylamide gels and in free solution', *ELECTROPHORESIS*, 30(S1), pp. S188–S195. doi: 10.1002/elps.200900052.

Stöcker, S. (2015) *Function of the Cytoplasmic FMRP Interacting Protein 1 (CyFIP1) in mouse*. Rheinische Friedrich-Wilhelms-Universität Bonn.

Sturchler-Pierrat, C. *et al.* (1997) 'Two amyloid precursor protein transgenic mouse models with Alzheimer disease-like pathology', *Proceedings of the National Academy of Sciences of the United States of America*, 94(24), pp. 13287–13292. doi: 10.1073/pnas.94.24.13287.

Takenawa, T. and Miki, H. (2001) 'WASP and WAVE family proteins: key molecules for rapid rearrangement of cortical actin filaments and cell movement.', *Journal of Cell Science*, 114(Pt 10), pp. 1801–1809.

Takenawa, T. and Suetsugu, S. (2007) 'The WASP-WAVE protein network: connecting the membrane to the cytoskeleton.', *Nature Reviews*, 8(1), pp. 37–48. doi: 10.1038/nrm2069.

Tang, G. *et al.* (2014) 'Loss of mTOR-Dependent Macroautophagy Causes Autistic-like Synaptic Pruning Deficits', *Neuron*, 83(5), pp. 1131–1143. doi: 10.1016/j.neuron.2014.07.040.

Tanida, I., Ueno, T. and Kominami, E. (2008) 'LC3 and autophagy - Methods in Molecular Biology', *Methods in Molecular Biology*, 445(2), pp. 77–88. doi: 10.1007/978-1-59745-157-4-4.

Thameem Dheen, S., Kaur, C. and Ling, E.-A. (2007) 'Microglial Activation and its Implications in the Brain Diseases', *Current Medicinal Chemistry*, 14(11), pp. 1189–1197. doi: 10.2174/092986707780597961.

Tiwari, S. S. *et al.* (2016) 'Alzheimer-related decrease in CYFIP2 links amyloid production to tau hyperphosphorylation and memory loss', *Brain*, 139(10), pp. 2751–2765. doi: 10.1093/brain/aww205.

Tiwari, S. S. and Suresh, S. (2016) *A study of putative p25 modulated synaptic molecules -CYFIP1, CYFIP2 and CSP -in Alzheimer's Disease*. King's College London.

Torres, M. *et al.* (2012) 'Defective lysosomal proteolysis and axonal transport are early pathogenic events that worsen with age leading to increased APP metabolism and synaptic Abeta in transgenic APP/PS1 hippocampus', *Molecular Neurodegeneration*,

7(1). doi: 10.1186/1750-1326-7-59.

Toyama, B. H. and Hetzer, M. W. (2013) 'Protein homeostasis: live long, won't prosper', *Nature Reviews Molecular Cell Biology*, 14(1), pp. 55–61. doi: 10.1038/nrm3496.

Verheij, C. *et al.* (1993) 'Characterization and localization of the FMR-1 gene product associated with fragile X syndrome', *Nature*, 363(6431), pp. 722–724. doi: 10.1038/363722a0.

Vorhees, C. V. and Williams, M. T. (2006) 'Morris water maze: Procedures for assessing spatial and related forms of learning and memory', *Nature Protocols*, 1(2), pp. 848–858. doi: 10.1038/nprot.2006.116.

Waites, C. L. *et al.* (2013) 'Bassoon and Piccolo maintain synapse integrity by regulating protein ubiquitination and degradation', *EMBO Journal*, 32(7), pp. 954–969. doi: 10.1038/emboj.2013.27.

Weston, L., Coutts, a. S. and La Thangue, N. B. (2012) 'Actin nucleators in the nucleus: an emerging theme', *Journal of Cell Science*, 125(15), pp. 3519–3527. doi: 10.1242/jcs.099523.

Winder, S. J. (2005) 'Actin-binding proteins', *Journal of Cell Science*, 118(4), pp. 651–654. doi: 10.1242/jcs.01670.

Witke, W. *et al.* (1998) 'In mouse brain pro lin I and pro lin II associate with regulators of the endocytic pathway and actin assembly', *Embo J.*, 17(4), pp. 967–976.

Witke, W. (2004) 'The role of profilin complexes in cell motility and other cellular processes.', *Trends in Cell Biology*, 14(8), pp. 461–9. doi: 10.1016/j.tcb.2004.07.003.

Witte, H., Neukirchen, D. and Bradke, F. (2008) 'Microtubule stabilization specifies initial neuronal polarization', *Journal of Cell Biology*, 180(3), pp. 619–632. doi: 10.1083/jcb.200707042.

Wohrle, D. *et al.* (1992) 'A microdeletion of less than 250 kb, including the proximal part of the FMR-I gene and the fragile-X site, in a male with the clinical phenotype of fragile-X syndrome', *American Journal of Human Genetics*, 51(2), pp. 299–306.

Yang, P.-C. and Mahmood, T. (2012) 'Western blot: Technique, theory, and trouble shooting', *North American Journal of Medical Sciences*, 4(9), p. 429. doi: 10.4103/1947-2714.100998.

Yu, L., Chen, Y. and Tooze, S. A. (2018) 'Autophagy pathway: Cellular and molecular mechanisms', *Autophagy*, 14(2), pp. 207–215. doi: 10.1080/15548627.2017.1378838.

Zhai, R. G. *et al.* (2001) 'Assembling the Presynaptic Active Zone', *Neuron*. Ahmari, 29(1), pp. 131–143. doi: 10.1016/S0896-6273(01)00185-4.

Zhang, Y. *et al.* (2019) 'Smaller Body Size, Early Postnatal Lethality, and Cortical Extracellular Matrix-Related Gene Expression Changes of Cyfip2-Null Embryonic Mice', *Frontiers in Molecular Neuroscience*, 11. doi: 10.3389/fnmol.2018.00482.

Zucker, R. S. and Regehr, W. G. (2002) 'Short-Term Synaptic Plasticity', *Annual Review of Physiology*, 64(1), pp. 355–405. doi: 10.1146/annurev.physiol.64.092501.114547.

7. Appendix

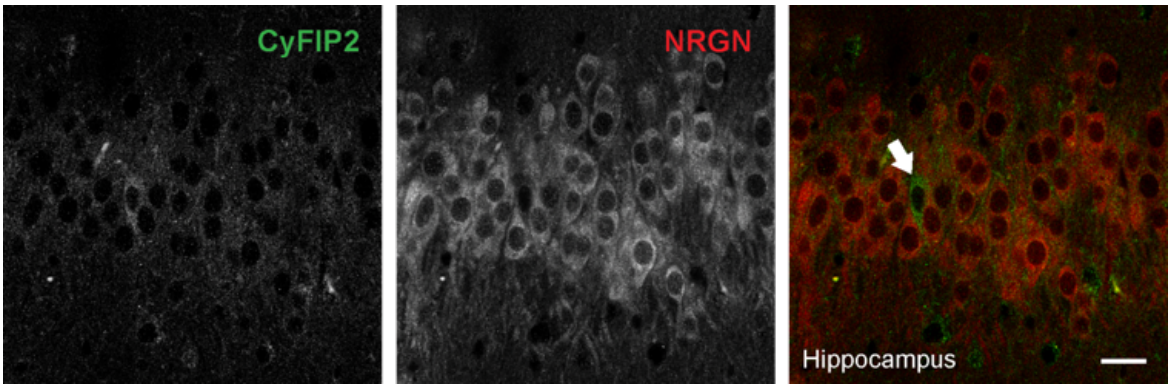

Supplementary Figure 1. Immunofluorescence staining of the *Cyfip2* conditional knockout mouse brain. In the CA1 region of the *Cyfip2* conditional knockout mice, where the protein is deleted in glutamatergic neurons, CyFIP2 expression can be observed only in a neuron (arrow) that is devoid of NRGN staining. Scale bar: 20 µm.

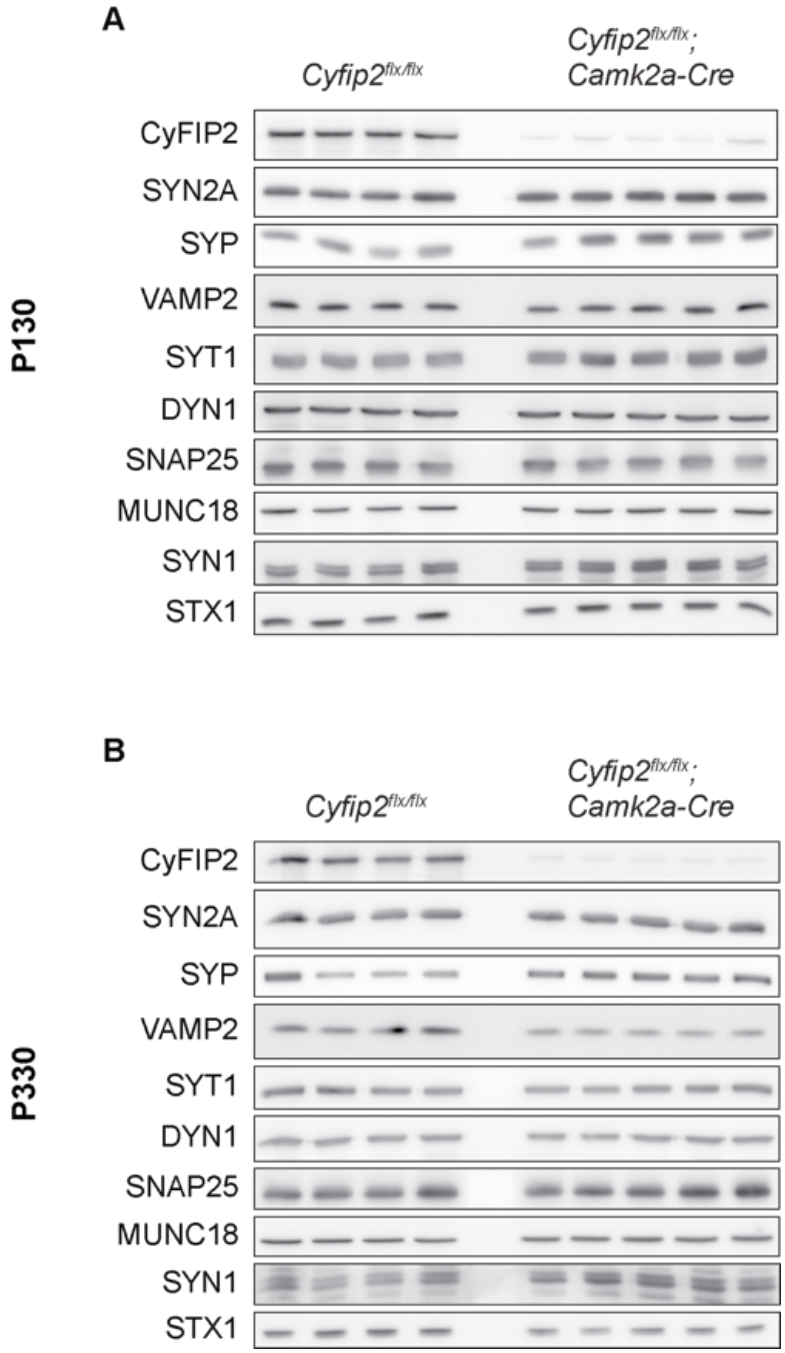

Supplementary Figure 2. Western blots showing the levels of pre-synaptic markers at ages P130 and P330.
Western blots of hippocampal total lysates from control and *Cyfip2*$^{flx/flx}$*;Camk2a-Cre* mice at ages (A) P130 and (B) P330. Figure 20 shows the quantification of these blots. n=4 animals for controls and n=5 animals for *Cyfip2*$^{flx/flx}$*;Camk2a-Cre* mice.

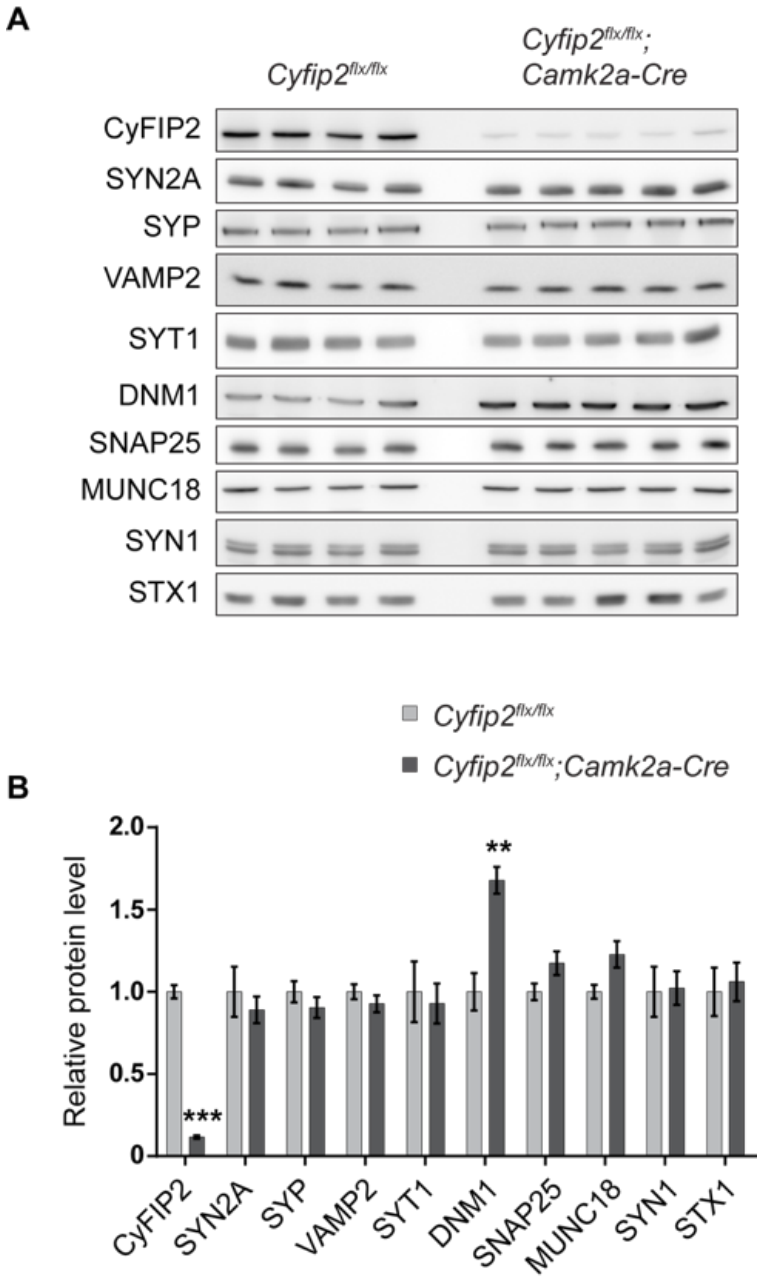

Supplementary Figure 3. Pre-synaptic protein levels are not altered in cortical lysates of P130 *Cyfip2* conditional knockout mice.
(A) Western blots from cortical lysates of P130 control and *Cyfip2* conditional knockout mice, probed with different antibodies for pre-synaptic markers. (B) Quantification of blots (shown in A) do not show any difference in the levels of pre-synaptic markers, except for an increase in DNM1. Coomassie stainings performed on the membrane were used as a loading control. n=4 animals for controls and n=5 animals for *Cyfip2*$^{flx/flx}$*;Camk2a-Cre* mice. Two-tailed t-test; **p<0.01, **p<0.001. Error bars represent mean ± s.e.m.

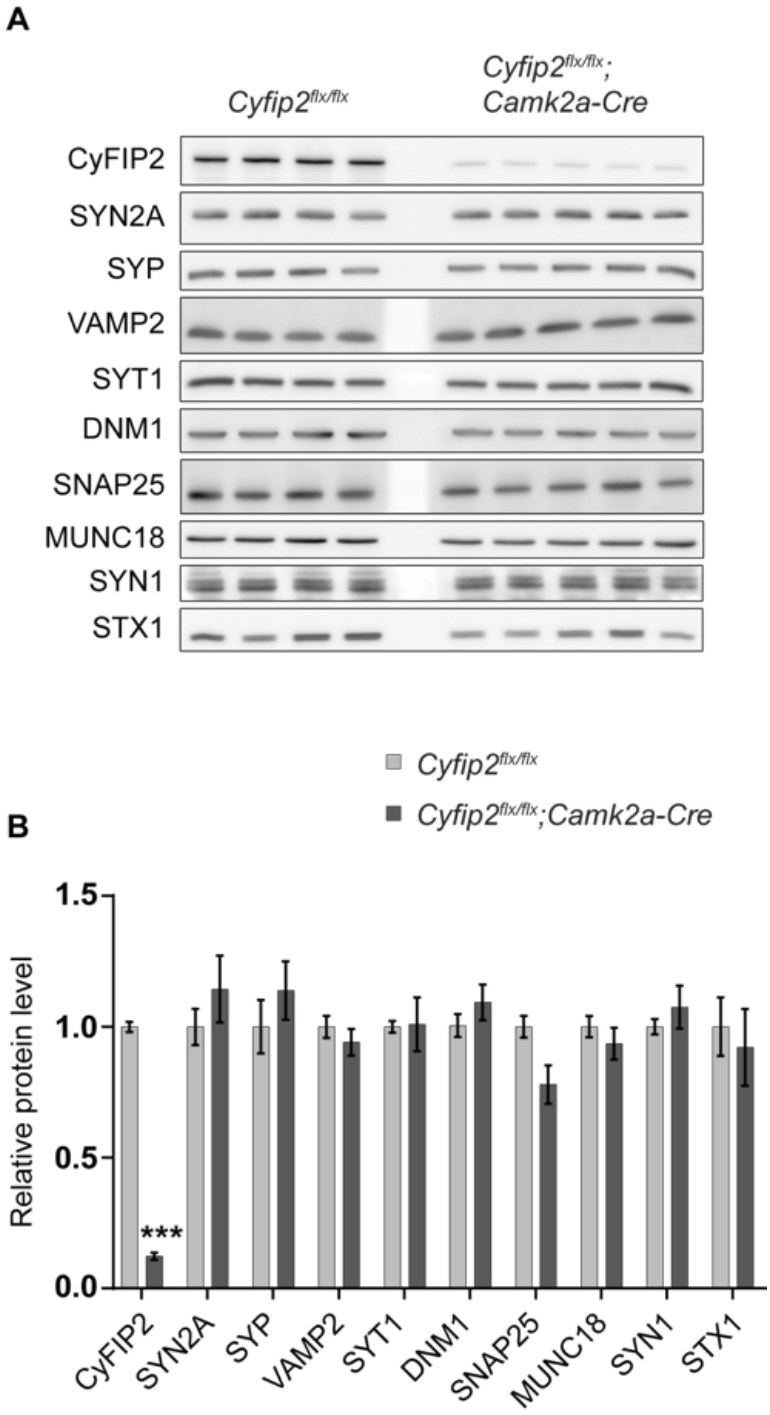

Supplementary Figure 4. Cortical pre-synaptic protein levels of P330 *Cyfip2* conditional knockout mice are unchanged with age.
(A) Western blots from cortical lysates of P330 control and *Cyfip2* conditional knockout mice, probed with different antibodies for pre-synaptic markers. (B) Quantification of blots (shown in A) do not show any difference in the levels of pre-synaptic markers compared to the controls, except for a slight decrease in SNAP25 levels. Coomassie stainings performed on the membrane were used as a loading control. n=4 animals for controls and n=5 animals for *Cyfip2*$^{flx/flx}$*;Camk2a-Cre* mice. Two-tailed t-test; *p<0.05, **p<0.001. Error bars represent mean ± s.e.m.

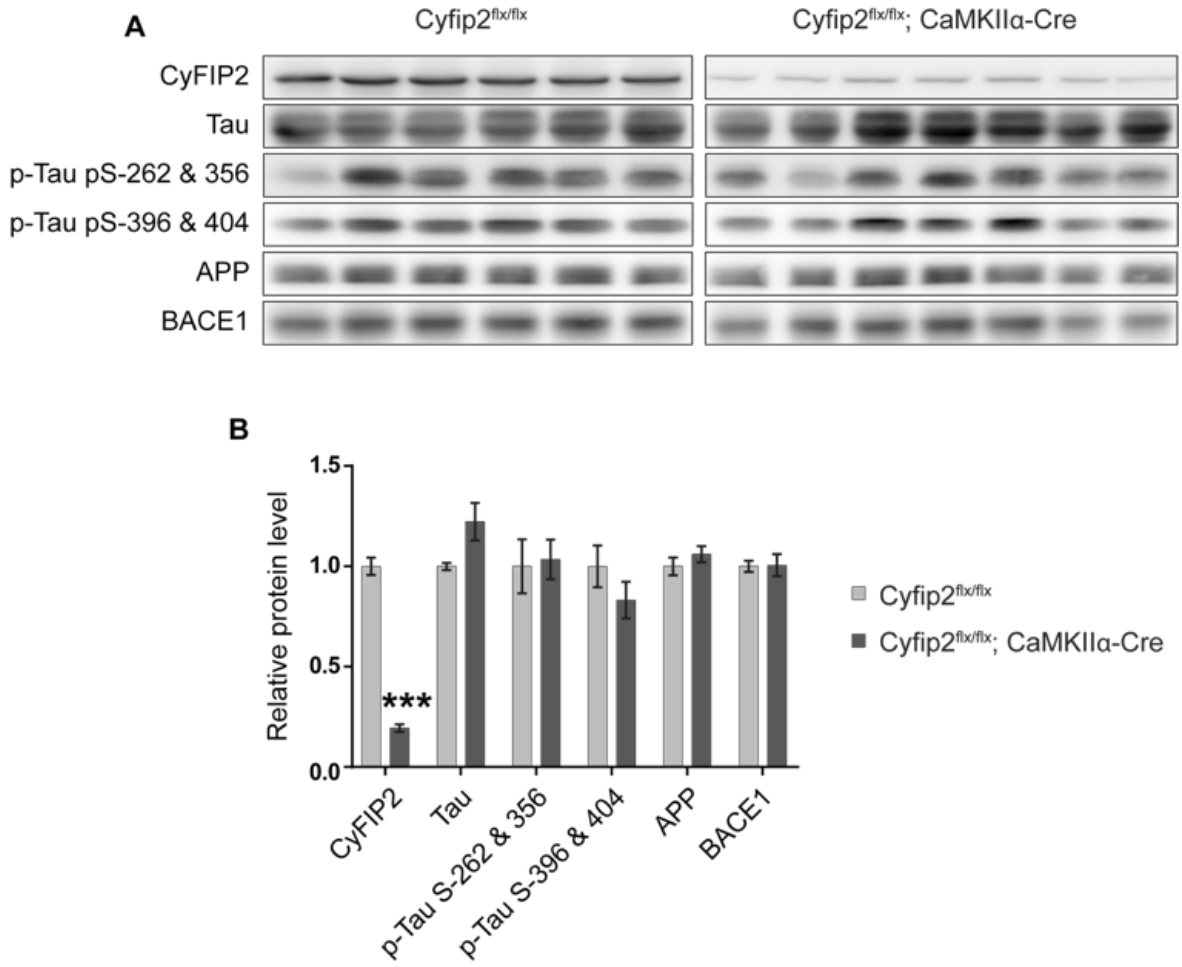

Supplementary Figure 5. P330 the *Cyfip2* conditional knockout mice show conserved Alzheimer's marker levels in the cortex.
(A) Western blots showing the levels of different Alzheimer's markers in the cortices of P330 control and conditional knockout mice. (B) Quantification of blots (shown in A) show no difference in the expression of Alzheimer's markers. Coomassie stainings performed on the membrane were used as a loading control. n=6 animals for controls and n=7 animals for *Cyfip2$^{flx/flx}$;Camk2a-Cre* mice. Two-tailed t-test; ***p<0.001. Error bars represent mean ± s.e.m.

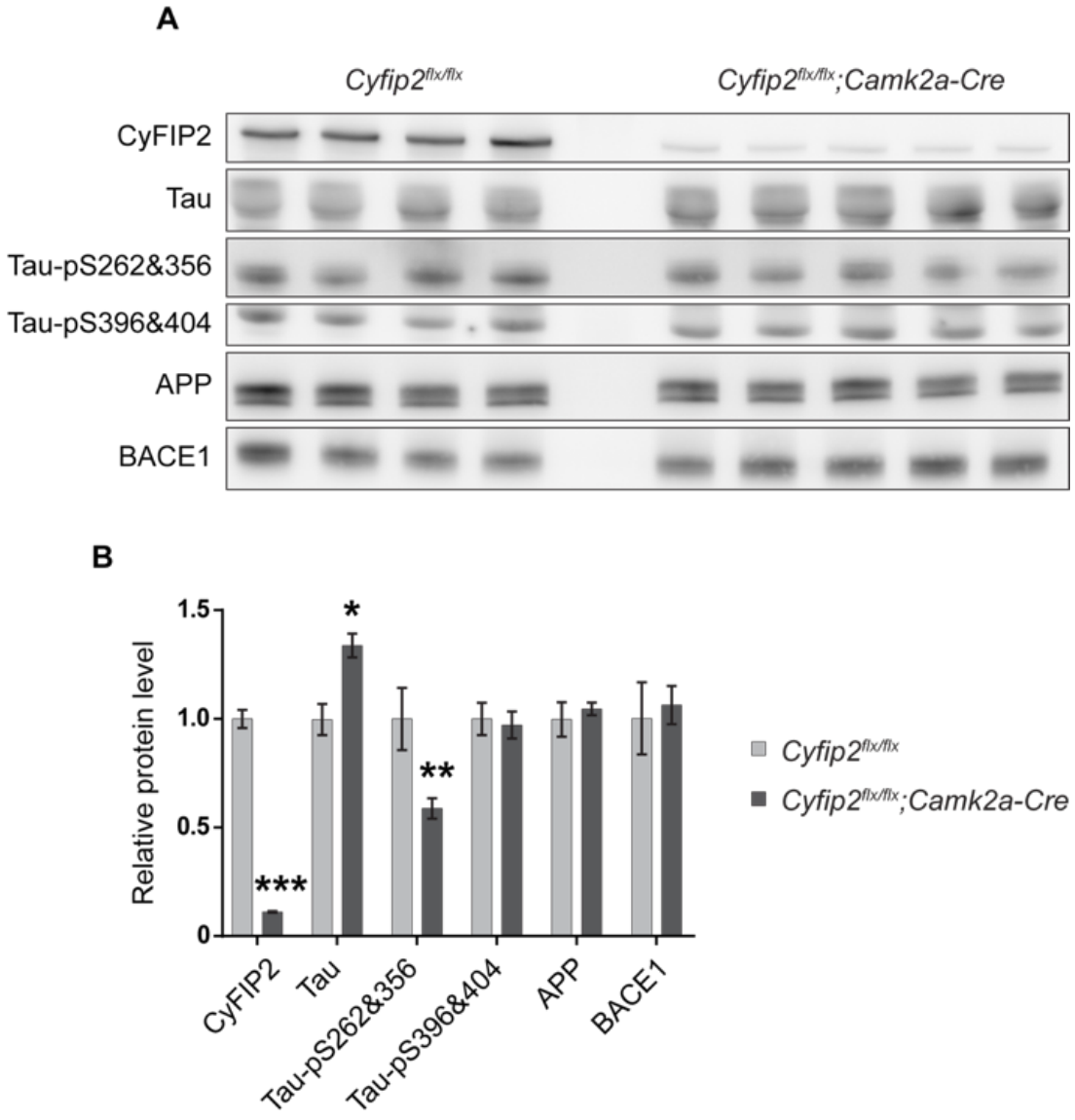

Supplementary Figure 6. Complete loss of CyFIP2 in the glutamatergic neurons of the hippocampus does not lead to the biochemical alterations of Alzheimer's disease.
(A) Western blots showing levels of different Alzheimer's markers in the hippocampi of P330 control and Cyfip2 conditional knockout mice. (B) Quantification of blots in A show increased total Tau and decreased Tau p-S262&356 levels, but in general no difference in the expression of Alzheimer's markers. Coomassie stainings performed on the membrane were used as calibration control. n=4 animals for controls and n=5 animals for Cyfip2flx/flx;Camk2a-Cre mice. Two-tailed t-test; *p<0.05, **p<0.01, ***p<0.001. Error bars represent mean ± s.e.m.

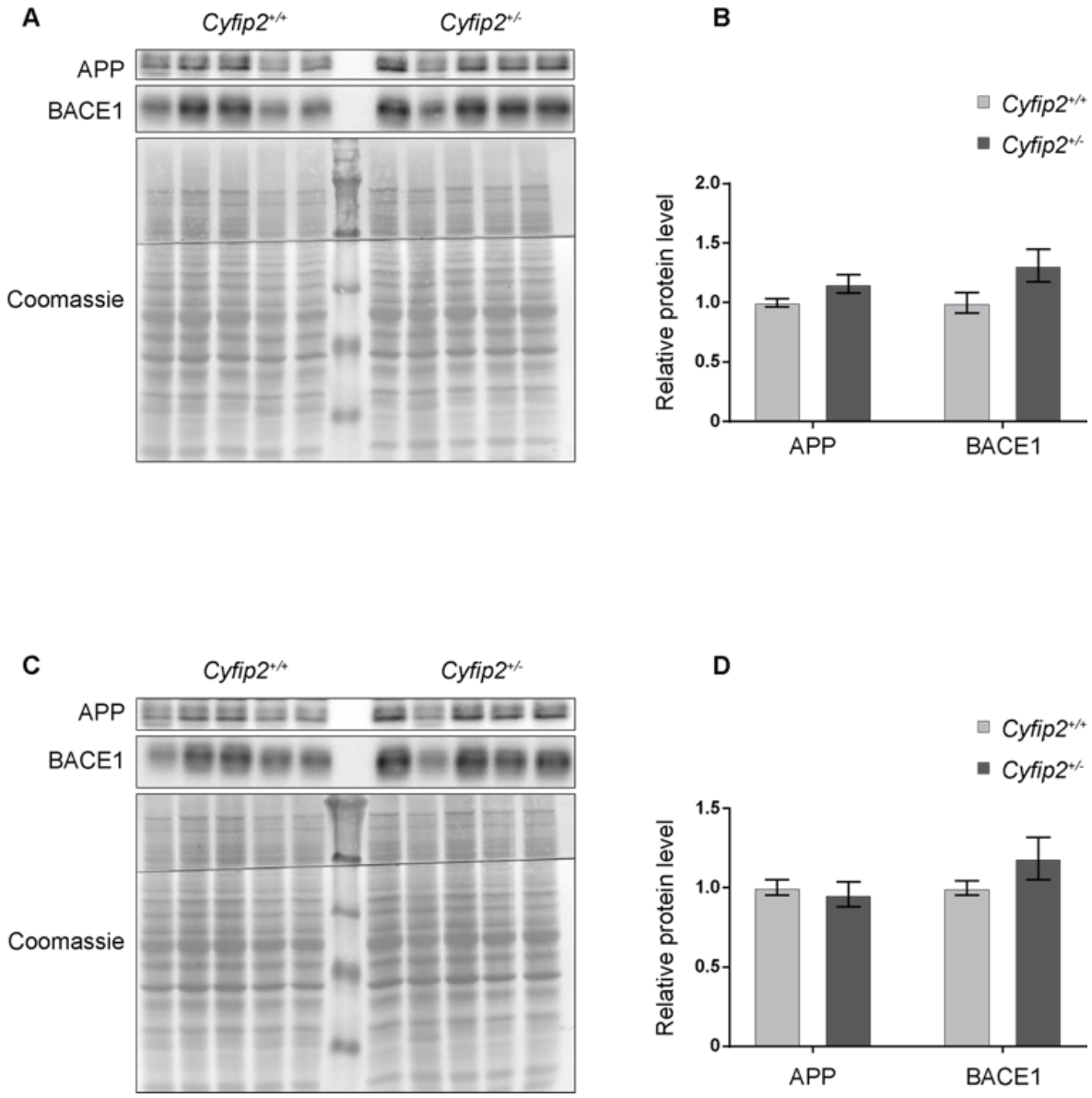

Supplementary Figure 7. *Cyfip2*$^{+/-}$ mice have conserved levels of Alzheimer's markers in total cortical and hippocampal lysates.
Western blots showing the levels of different Alzheimer's markers in (A) cortical and (C) hippocampal lysates of ~7 months old control and *Cyfip2*$^{+/-}$ mice. (B, D) Quantification of blots (shown in A, C) show no difference in the expression of APP and BACE1 in Cyfip2$^{+/-}$ mice. Coomassie stainings performed on the membrane were used as a loading control. n=5 animals per genotype. Error bars represent mean ± s.e.m.

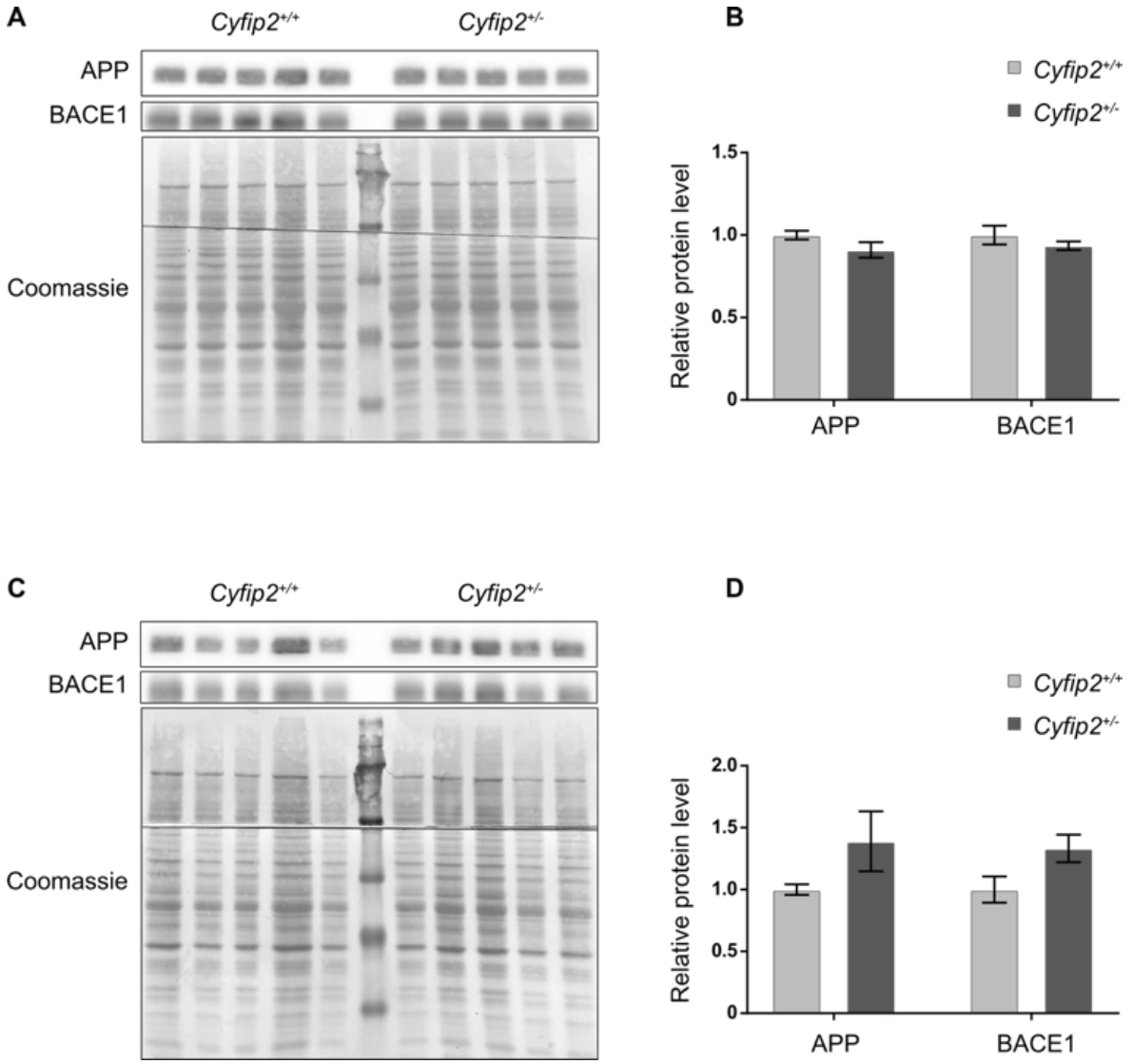

Supplementary Figure 8. *Cyfip2*$^{+/-}$ mice have conserved levels of Alzheimer's markers in cortical and hippocampal synaptosomes.
Western blots showing the levels of different Alzheimer's markers in (A) cortical and (C) hippocampal synaptosomes of ~7 months old control and *Cyfip2*$^{+/-}$ mice. (B, D) Quantification of blots (shown in A, C) show no difference in the expression of APP and BACE1 in Cyfip2$^{+/-}$ mice. Coomassie stainings performed on the membrane were used as a loading control. n=5 animals per genotype. Error bars represent mean ± s.e.m.

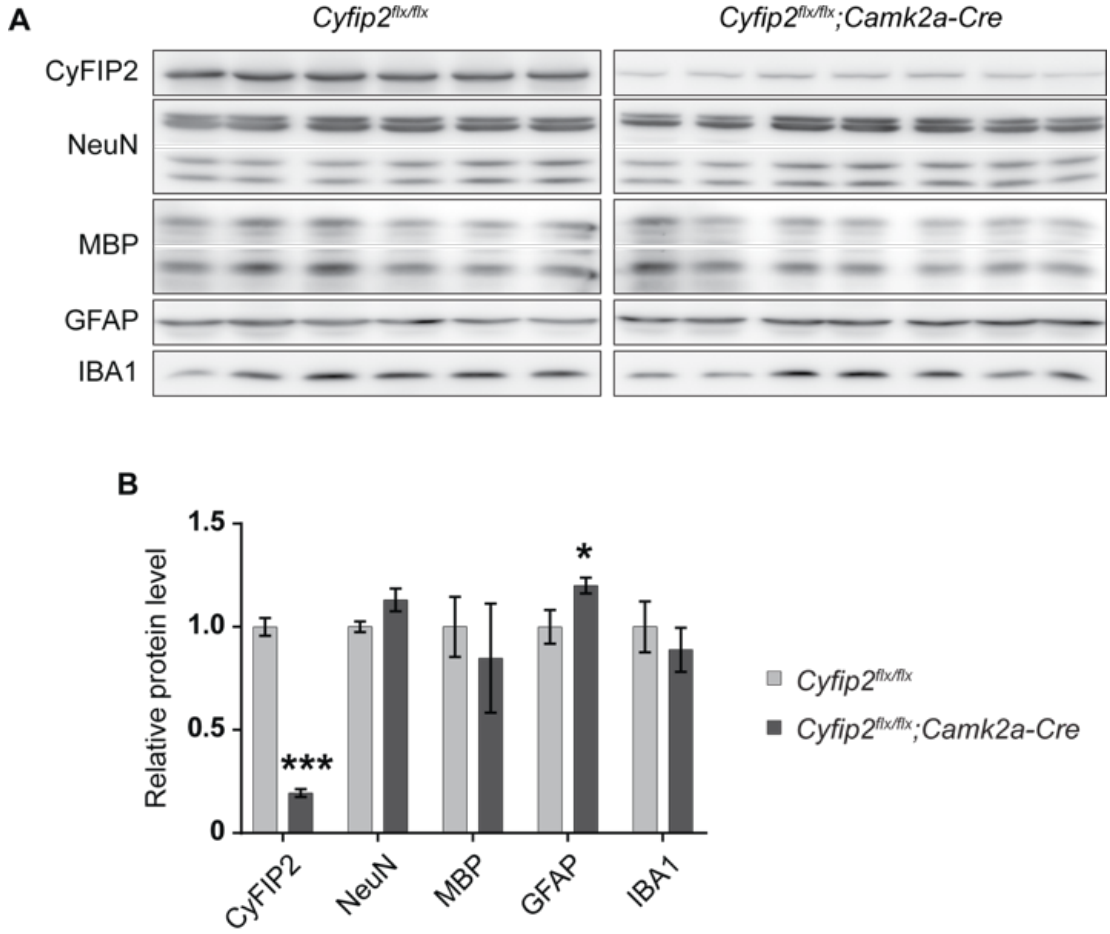

Supplementary Figure 9. *Cyfip2* conditional knockout mice show slightly increased astrogliosis in the cortex.
(A) Western blots of cortical total lysates probed with antibodies against neuronal and glial marker proteins. (B) *Cyfip2*$^{flx/flx}$*;Camk2a-Cre* mice show no differences in the neuronal and glial markers, except a slight but significant increase in the astrocyte marker GFAP, pointing to increased astrogliosis. Coomassie stainings performed on the membrane were used as a loading control. n=6 animals for controls and n=7 animals for *Cyfip2*$^{flx/flx}$*;Camk2a-Cre* mice. Two-tailed t-test; *p<0.05, ***p<0.001. Error bars represent mean ± s.e.m.

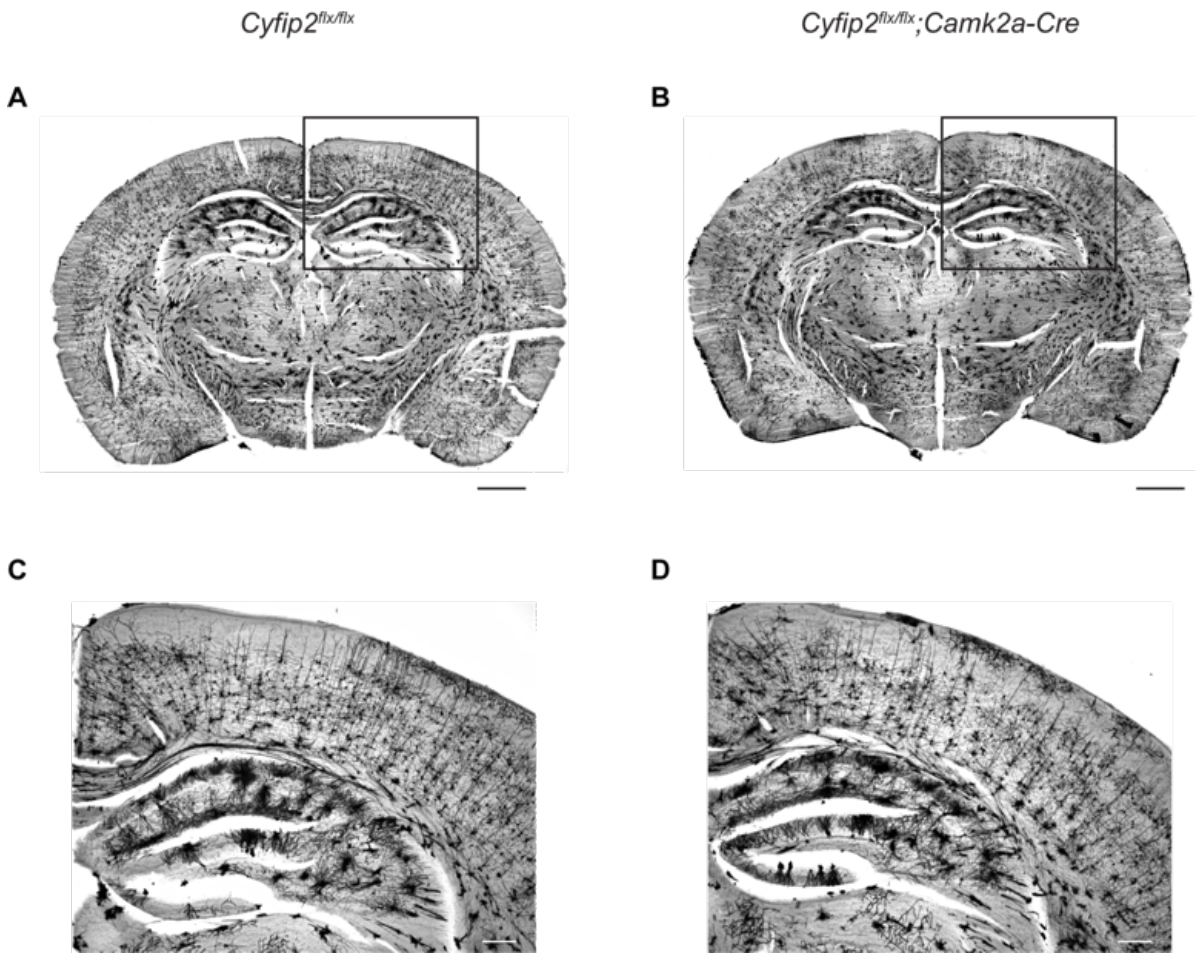

Supplementary Figure 10. *Cyfip2* conditional knockout does not lead to defects in gross morphology.
200 µm coronal slices of brains from (A) control and (B) *Cyfip2*$^{flx/flx}$*;Camk2a-Cre* mice, stained with Golgi staining method show no defects in the morphology of the brain (indicated areas are shown in C and D). (C, D) Cortical layering and hippocampal organization are unaltered in the *Cyfip2* conditional knockout mice. (A) and (B) scale bars – 1mm; (C) and (D) scale bars – 100 µm.

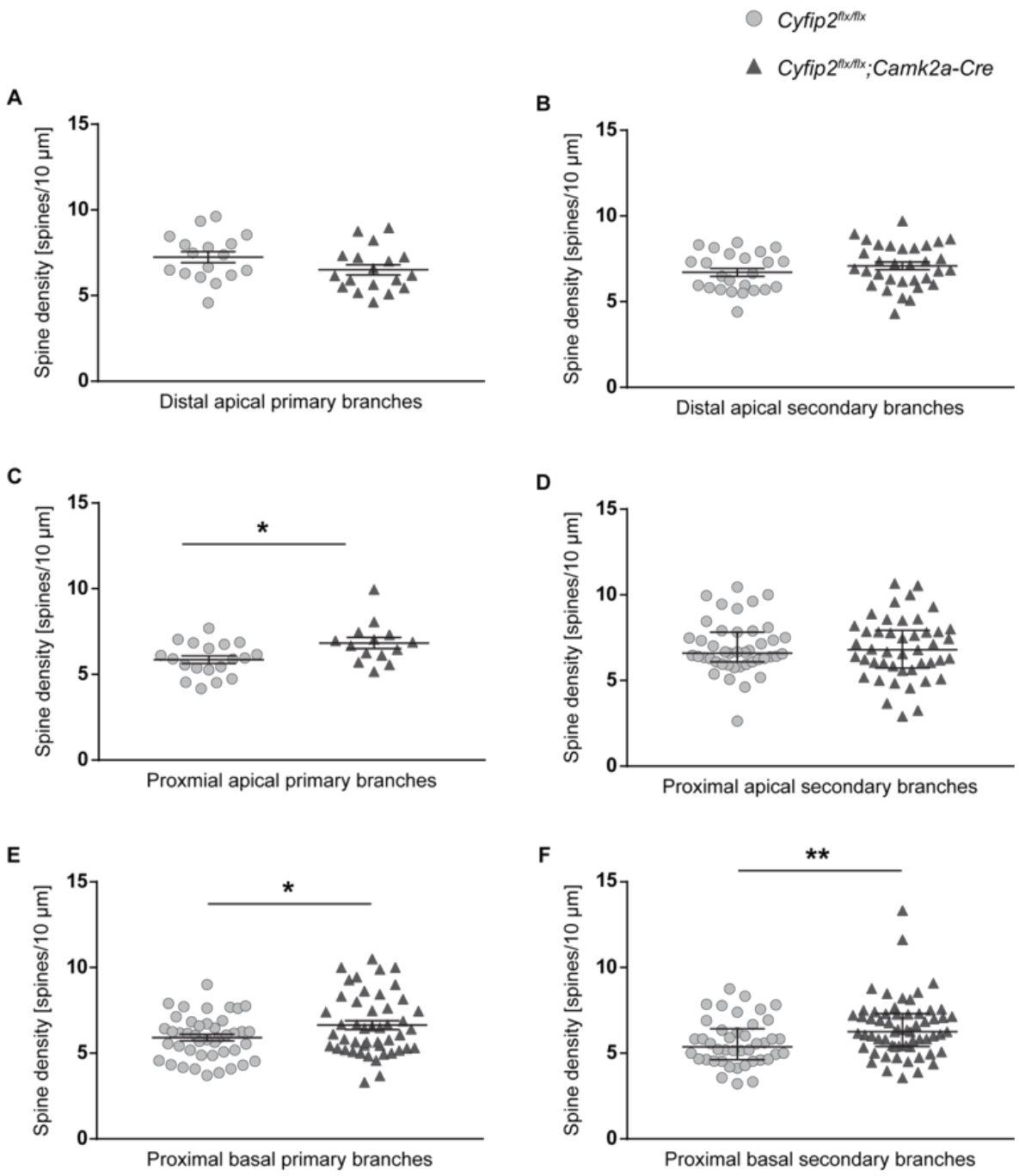

Supplementary Figure 11. Total number of spines are altered in cortical layer 5 pyramidal neurons of *Cyfip2* conditional knockout mice.
(A) Primary and (B) secondary branches on distal (100 µm from soma) regions of neurons show no difference in spine density between the genotypes. The proximal regions of dendrites in *Cyfip2* conditional knockout mice show increased spine density in the (C) apical primary, (E) basal primary and (F) secondary branches whereas the spine density is conserved in (D) apical secondary branches. n=x animals for controls and n=2 animals for both genotypes. In all graphs each data point represents one neuron. Error bars in (A, B, C, E) represent mean ± s.e.m.; Two-tailed t-test. Error bars in (D, F) represent median ± interquartile range; Mann-Whitney test, *p≤0.05, ** p≤0.01.

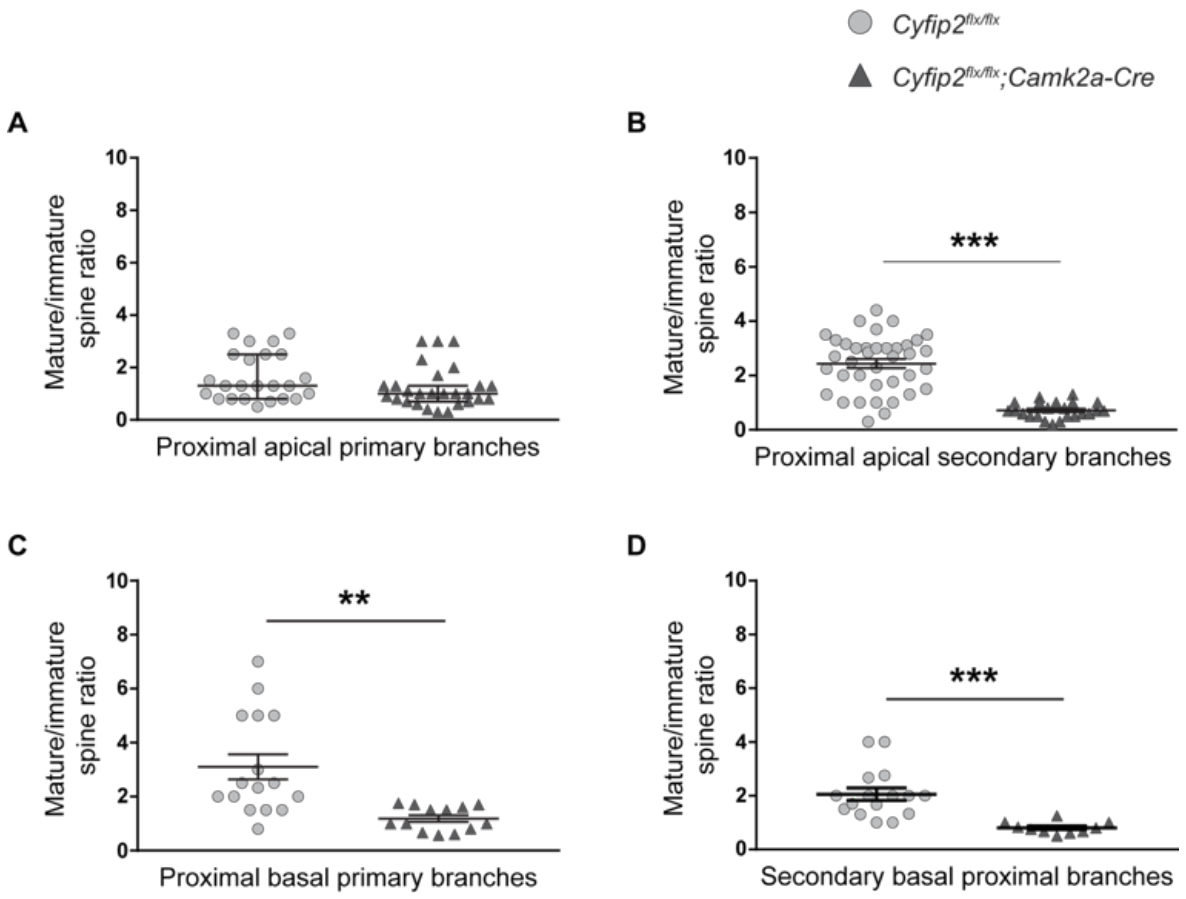

Supplementary Figure 12. *Cyfip2* conditional knockout mice have decreased mature/immature spine ratio in cortical layer 5 pyramidal neurons.
(A) Mature/immature spine ratios of proximal apical primary branches are conserved between the genotypes. On the proximal region of layer 5 pyramidal neurons (B) apical secondary, (C) basal primary and (D) secondary branches show dramatically reduced mature/immature spine ratios. n=2 animals for both genotypes. In all graphs, each data point represents one neuron. Data was checked for normality using the Shapiro-Wilk test. Error bars in (A) represent median with interquartile range; Mann-Whitney test. Error bars in (B-D) represent the mean ± s.e.m.; Two-tailed t-test, **p≤0.01, ***p≤0.001.

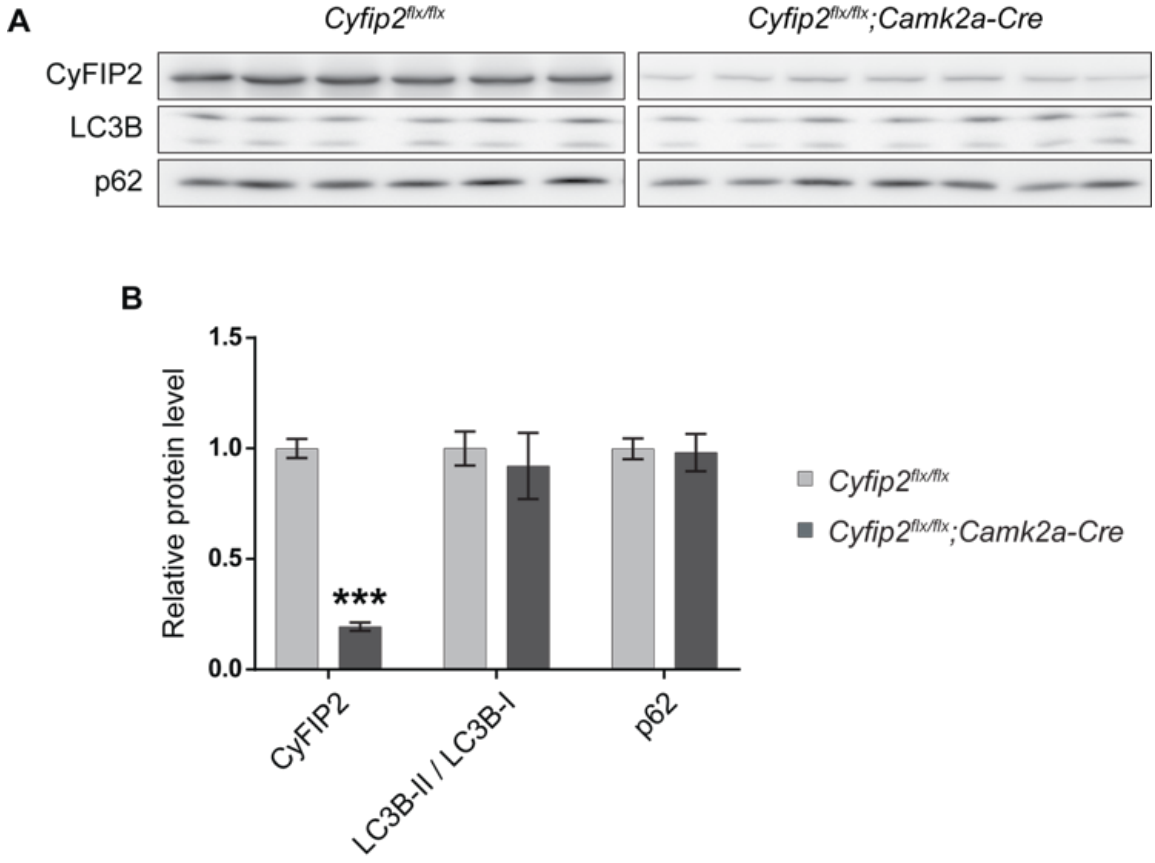

Supplementary Figure 13. Levels of autophagy markers are conserved in the cortex of *Cyfip2* conditional knockout mice.
(A) Western blots of cortical total lysates probed with autophagy marker antibodies. (B) Quantification of blots (shown in A) point to conserved LC3B-II/LC3B-I ratio and p62 levels, indicating no difference in autophagy. Coomassie stainings performed on the membrane were used as a loading control. n=6 animals for controls and n=7 animals for *Cyfip2*$^{flx/flx}$*;Camk2a-Cre* mice. Two-tailed t-test; ***p<0.001. Error bars represent mean ± s.e.m.

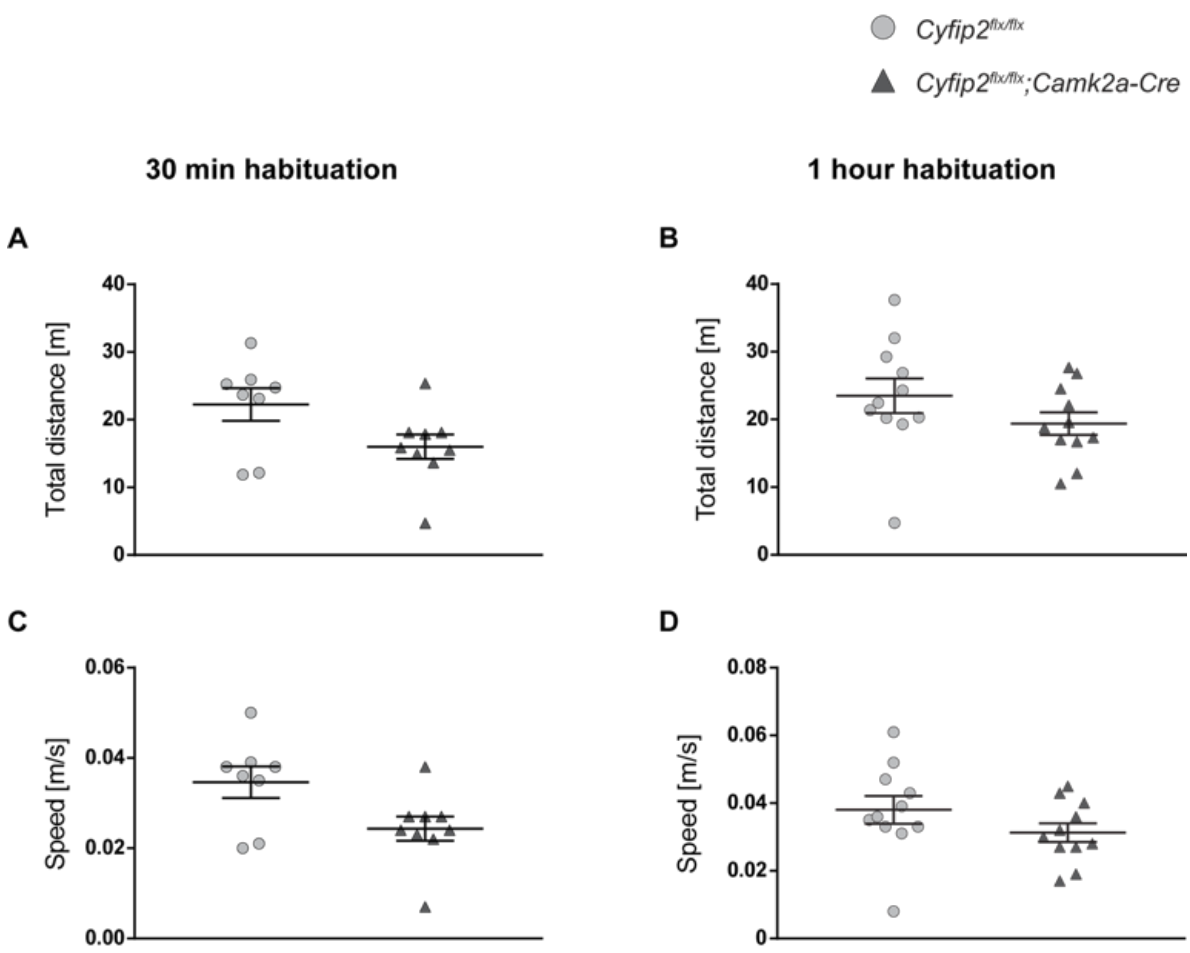

Supplementary Figure 14. *Cyfip2* conditional knockout mice have slightly reduced locomotion.
In an open-field test of 10 minutes, *Cyfip2* conditional knockout mice (A, B) travelled similar distances with (C, D) similar speeds compared to the controls, independent of the habituation time to the room. (A) and (C) n=10 animals for controls and n=9 animals for Cyfip2$^{flx/flx}$;Camk2a-Cre mice. (B) and (D) n=11 animals for both genotypes. Two-tailed t-test. Error bars represent mean ± s.e.m.

Acknowledgements

First of all, I would like to thank my supervisor Prof. Dr. Walter Witke for giving me the opportunity to work on this interesting project and for all his support in the last 5 years both professionally and personally.

Secondly, I would like to thank Prof. Dr. Frank Bradke for the nice conversations, support and for all his input to this work. I would also like to thank Prof. Dr. Susanne Schoch-McGovern and Prof. Dr. Sergio Conti for agreeing to be a part of my doctoral committee.

I would especially like to thank my supervisor Dr. Pietro Pilo Boyl for his guidance throughout my doctoral studies as well as for the fruitful discussions that enriched my knowledge along the way. Next, I would like to thank all my colleagues with whom I had a chance to work with in the last 5 years. I would like to thank Stefanie Hauck for the generation of the CyFIP2 antibody (1C4) that made most of this thesis possible. I particularly want to thank Marina Di Domenico and Carina Beuck for their great friendship and support. Another special thanks to my two great students Annika Böhm and Daniela Stausberg, who helped me with this project while creating a nice environment in the lab.

Of course, I would like to thank my friends whose support has been indispensable throughout my doctoral studies and more. I thank Cansu Tekin and Ezgi Bulca, for being there for me whenever I needed it. I would like to thank Dilege Gülmez, for being the greatest ally during the Germany chapter of our lives and for his reliable support. My special thanks goes to Ripunjay Acharya, who has really been there for me, especially throughout my thesis writing marathon, and for his trusting companionship. I would like to thank Paulina Rocha-Moran and Roberto Cota for making Bonn feel more like home with their sincerity. Emrah Özkan, for his friendship and the stimulating conversations. Jan-Matthis Lückmann, for always offering a sympathetic ear with his kind nature and Thorsten Schimannek, for the delightful memories he creates. Cemre Kızılarmut, for bringing joy to my life in Bonn with her friendship. Erdi Küçük, for being a reliable and supportive friend wherever he may be.

I would like to thank Joanna Komorowska-Müller and Catia Domingos for their support during our PhD adventure as well as for our time together. I thank Nasim Dokani Khesroshahi and Negar Nikbakht for their PhD solidarity. I am grateful to Ana Pavlovic, Michelina Kierzek, Julia Hartweg, Melanie Krause, Simon Rangger and Stefan Dahlhoff for their amazing companionship over the last 6 years.

Yalnız olmadığımı her gün hissettiren, arkadaşlıklarıyla beni mutlu eden Cansu Tekin, Ezgi Bulca, Dilege Gülmez, Ripunjay Acharya'ya en içten dileklerimle teşekkür ederim.

Mesafelerin aramıza girmesine izin vermeden her zaman yanımda olan, hayatımı güzel kılan dostlarım Işılsu Yıldırım, Gülce Coşku Yılmaz, Burak Özer, Dila Kadakal ve Berk Sağlam'a güvenilir arkadaşlıklarından dolayı teşekkür ederim.

Son olarak ve en önemlisi, hayatta her konuda yanımda olan ve bu güne kadar desteklerini asla esirgemeyen aileme teşekkür ederim. Annem Nil Pembe Özer ve babam Mithat Fırat Özer'e benim için yaptıkları bütün fedakarlıklar için, hayatımı renklendiren canım kardeşim Rengin Su Özer'e koşulsuz sevgisi için minnettarım.